Doctoral Dissertation

Fabrication of Electrode−Electrolyte Interface to Enhance Electrochemical Properties of Anode Materials for Alkali-Metal-Ion Rechargeable Batteries

（アルカリ金属イオン二次電池負極材料を活かす電極－電解質界面の構築）

January 2019

Kazuki Yamaguchi

Department of Chemistry and Biotechnology

Graduated School of Engineering

Tottori University

Preface

The studies presented in this thesis were carried out under the guidance of Professor Hiroki Sakaguchi, Associate Professor Hiroyuki Usui, and Assistant Professor Yasuhiro Domi at Applied Chemistry Course, Department of Chemistry and Biotechnology, Graduated School of Engineering, Tottori University during 2016–2019.

The object of this thesis is to fabricate a functional electrode−electrolyte interface which can enhance the electrochemical properties of alloy-based anode active materials for alkali metal-ion rechargeable batteries such as Li-ion and Na-ion batteries. The author wishes sincerely that the findings from his study would be able to contribute to the achievement of rechargeable batteries with high energy density and high safety.

Kazuki Yamaguchi

Department of Chemistry and Biotechnology

Graduate School of Engineering

Tottori University

4-101 Minami, Koyama-cho, Tottori 680-8552, Japan

January 2019

1

Content

General Introduction

Lithium-ion batteries (LIBs) have been widely used in portable electronic devices, such as smartphones and laptop computers because of their high energy density. While they have also used on a larger scale, *e.g.*, as power sources in electric vehicles (EVs) and stationary power supply systems, their energy densities are not yet sufficient for such large-scale applications. More specifically, graphite anode, which is currently used in commercial LIBs, has an insufficient capacity (372 mA h g^{-1}) for EVs application. On the other hand, silicon (Si) is a promising active material for an anode due to its remarkably high theoretical capacity of 3580 mA h g^{-1} ($Li_{15}Si_4$).[1,2] However, Si shows a poor cycle stability because it goes through huge volumetric changes of 380% during lithiation/delithiation reactions,[3,4] which generates high stresses and large strains in the active material. The accumulation of strains during repeated charge–discharge cycling results in disintegration of the active material layer. In addition, Si has disadvantages of a low electrical conductivity (~1 × 10^5 Ω cm) and a low diffusion coefficient of Li^+ within it (D_{Li}^+: 1 × 10^{-14} to 1 × 10^{-12} cm^2 s^{-1}).[5,6] These are the main reasons why a practical application of Si electrodes has been hindered.

Recently, room temperature ionic liquids have widely applied to an organic synthesis, gas separation, vacuum technology, and energy devices including batteries and electrochemical capacitors in the science and industry field.[7–15] Electrolytes are one of the most important factors determining the battery performance and safety. Although carbonate-based organic solvents have been utilized as an electrolyte solvent in current LIBs, they contain a fear of ignition and/or explosion. Therefore, ionic liquids have received much attentions as an alternative to a conventional organic electrolyte because of their excellent physicochemical properties, such as non-flammability, negligible vapor pressure, and wide electrochemical window.[16–22] Since a higher safety is demanded with an increase in the energy density of the batteries, the replacement of a flammable organic solvent with an ionic

5

liquid as an electrolyte solvent can remarkably improve the safety of batteries. Nevertheless, there have been still few reports on application of ionic liquid electrolyte to Si-based anodes.

Meanwhile, there are concerns regarding the maintenance of stable supply of Li for application to large-scale battery systems. Currently, the main Li resources are available in South America, especially Chile and Bolivia, which accounts for 76% of the total.[23,24] The price of Li will significantly increase in the near future, as the demand for Li increases by the popularization of large-scale LIBs for EVs and stationary power supply applications. Therefore, the development of next-generation energy storage devices which use Na^+ as the charge carrier, namely Na-ion batteries (NIBs) have been required. There is no doubt that Na resources are inexhaustible and ubiquitous. However, it would be very difficult to replace Li^+ with Na^+ in the current LIBs system because Na^+ is larger than Li^+. Thus, Li^+-insertion into the interlayer of graphite which is currently used in LIBs occurs to provide a reversible capacity, whereas Na^+-insertion hardly proceeds due to its size.[23–25] Recently, many researchers have studied a hard carbon as an anode material.[23,26–28] It can absorb Na^+ in its nano pores, and exhibits a stable cycle performance. However, the capacity is comparatively small as *ca.* 300 mA h g^{-1}. To further increase the energy density of NIBs, development of metal- or alloy-based anode materials with higher capacities are absolutely imperative.

This thesis consists of following six chapters.

In Chapter 1, the ionic liquids consisted of 1-((2-methoxyethoxy)methyl)-1-methylpiperidinium (PP1MEM) cation and bis(fluorosulfonyl)amide (FSA), bis(trifluoromethanesulfonyl)amide (TFSA), or tetrafluoroborate (BF_4) anion were applied to an electrolyte solvent for LIBs. To definitely investigate the effect of anion species of ionic liquids on cycling performance of a Si-alone electrode, the anion of ionic liquid and that of Li salt were conformed.

In chapter 2, applicability of the FSA- and TFSA-based ionic liquid electrolyte to an annealed Ni–P/(etched Si) composite electrode was investigated to enhance its electrochemical performance.

In chapter 3, the reaction behavior of the Si-alone electrode in the FSA-based ionic liquid electrolyte was investigated by combination of field-emission scanning electron microscopic (FE-SEM) observation and soft X-ray emission spectroscopy (SXES) to elucidate the origin for the better performance of the Si-based electrode in the electrolyte consisted of PP1MEM-FSA in chapter 1 and 2. In addition, two-dimensional delithiation distribution on the Si electrode surfaces after cycling was also confirmed by Raman mapping analysis.

In chapter 4, the effect of a film-forming additive for imidazolium-based ionic liquid electrolyte on the charge–discharge performance of the Si-alone anode was investigated to enhance its rate capability.

In chapter 5, electrochemical performance of a Sn_4P_3 anode for NIBs was evaluated in ionic liquid electrolyte at intermediate temperature, and temperature dependence of cell resistances was discussed by electrochemical impedance spectroscopy.

In chapter 6, influence of cation structure of ionic liquid electrolyte on the rate capability of the Sn_4P_3 anode was studied at room temperature. Furthermore, the factor of improving rate capability was considered from a viewpoint of solvation number and conductivity in the electrolytes.

Finally, concluding remarks are presented.

Chapter 1

Influence of the Structure of the Anion in an Ionic Liquid Electrolyte on the Electrochemical Performance of a Silicon Anode for LIBs

1.1 Introduction

Since Lai firstly reported solid lithium–silicon electrode could operate at 400 ^{o}C,[29] silicon (Si) is a promising active material as an anode material for next-generation LIBs. It has a remarkably high theoretical capacity of 3580 mA h g^{-1} (Li$_{15}$Si$_4$) and a relatively low lithiation–delithiation potential below 0.4 V vs. Li$^+$/Li.[30,31] However, Si undergoes a huge change in volume during alloying/dealloying reactions with Li,[32,33] and this generates high stress and strain in the active material. The accumulation of strain during repeated charge–discharge cycling brings about disintegration of the active material layer, which results in poor cyclability for a Si electrode. To overcome this issue, a nano-sized silicon has been studied as one of the promising approaches. Wu *et al.* demonstrated that nano-sized Si-coated graphite retained a relatively high reversible capacity of 567 mA h g^{-1} over 20 cycles.[34] It was reported that vacuum deposited Si films on rough Ni and Cu substrates exhibited excellent cyclability, and the film consisted of nano-particles with polycrystalline kept structure stable against volumetric change during Li-insertion/extraction.[35]

Our group recently revealed that excellent cycle performances of Si-based electrodes were achieved in the commercially available ionic liquid consisted of piperidinium cation and bis(trifluoromethanesulfonyl)amide (TFSA) anion, and that the electrode performances originate from its high stability against cathodic decomposition.[36–38] The author demonstrated that the effect of cation structure on the electrochemical performance of Si-alone electrode by using ionic liquids having piperidinium cation in which position and number of oxygen atoms

is different. As a result, piperidinium-cation with ether group having two oxygen atoms was the most suitable to enhance the performance of Si electrode.

On the other hand, the anion of an ionic liquid electrolyte is also an important factor because it should affect the solvation structure of Li^+, ionic conductivity, viscosity and so on. [39–41] For example, the solvation structure of Li^+ in a bis(fluorosulfonyl)amide (FSA)-based ionic liquid electrolyte is different from that in a bis(trifluoromethanesulfonyl)amide (TFSA)-based electrolyte, even though FSA^- and $TFSA^-$ are based on the same amide. Li^+ forms $[Li(TFSA)_2]^-$ and $[Li(FSA)_3]^{2-}$ ion clusters in $TFSA^-$- and FSA^--based ionic liquid electrolytes, respectively. [42–44] In a TFSA-based ionic liquid electrolyte, two TFSA anions are bidentate to Li^+ through their oxygen atoms. In contrast, in a FSA-based electrolyte, one FSA anion is bidentate and two are monodentate to Li^+. While the relationship between the structure of the anion in an ionic liquid electrolyte and the electrochemical performance of a anode other than a Si-based electrode (*e.g.*, graphite) has been reported, [45–47] there have been no systematic studies for Si-based electrodes. In this chapter, the author investigated the effect of the structure of the anion in an ionic liquid electrolyte on the electrochemical performance of a Si anode for use in LIBs. In order to directly observe the electrochemical reaction between Si electrode and the electrolyte, the author used Si films prepared by a gas-deposition (GD) method. This method does not require any binder and conductive additive to prepare thick-film electrodes. [48] It enables us to clarify an original electrochemical property of pristine Si electrode. In addition, the author used ionic liquid electrolytes with a single anion species; i.e. the anion of the Li salt was the same as that of the ionic liquid.

1.2 Experimental Details

In preparation of Si electrodes by a GD method (Figure 1-1), commercial Si powder (99.9%, Wako Pure Chemical Industries, Ltd.) was used as the raw material. For the GD, a

9

Cu current collector (20-μm thickness; 99.9%, Nilaco Co., Ltd.) was placed at a distance of 10 mm from the nozzle in a vacuum chamber with a guide tube. The nozzle with a 0.8 mm diameter was connected to the end of the guide tube. An argon carrier gas with a purity of 99.99% was used at a differential pressure of 7.0×10^5 Pa. After the chamber was evacuated to a base pressure of several ten Pa, an aerosol consisting of the argon carrier gas and the Si powder was generated in the guide tube, and instantly gushed from the nozzle onto the Cu substrate. The weight of the deposited active material on the substrate was measured to an accuracy of 1 μg by ultra-microbalance (XP6, METTLER TOLEDO) equipped with an anti-vibration table, and the author used Si thick-film electrode in the range of 28−32 μg. The weight of the deposited active materials and the deposition area on the Cu substrate were *ca.* 30 μg and 0.80 cm^2, respectively. The author assembled a 2032-type coin cell consisting of the Si electrode as a working electrode, Li metal foil (Rare Metallic Co., Ltd., 99.90%) as a counter electrode, and a glass fiber filter (Whatman GF/A) as a separator. The ionic liquid used in this study consisted of 1-((2-methoxyethoxy)methyl)-1-methylpiperidinium (PP1MEM) cation and three types of anion, *i.e.*, FSA, TFSA, or tetrafluoroborate (BF$_4$), as shown in Figure 1-2. The electrolyte solution used was 1 mol dm^{-3} LiX-dissolved in PP1MEM-X (X: FSA, TFSA, or BF$_4$). 1 mol dm^{-3} LiTFSA in propylene carbonate (PC; C$_4$H$_6$O$_3$, Kishida Chemical Co., Ltd.) was also used as a conventional organic electrolyte. The preparation of electrolyte solution and cell assembly were performed in an Ar-filled glove box (Miwa MFG, DBO-2.5LNKP-TS) with a dew point below −100 $^{\circ}$C and oxygen content below 1 ppm. A galvanostatic charge–discharge test was conducted using an electrochemical measurement system (HJ-1001SD8, Hokuto Denko Co., Ltd.) in a potential range between 0.005 and 2.000 V vs. Li$^+$/Li at 303 K under a current density of 0.42 A g^{-1} (0.12 C). The high-rate performance of the electrodes was investigated at a current rate from 0.12 C to 12 C. The ionic conductivity of ionic liquid electrolytes was also investigated by an

electrochemical impedance spectroscopic analysis in the frequency range from 100 kHz to
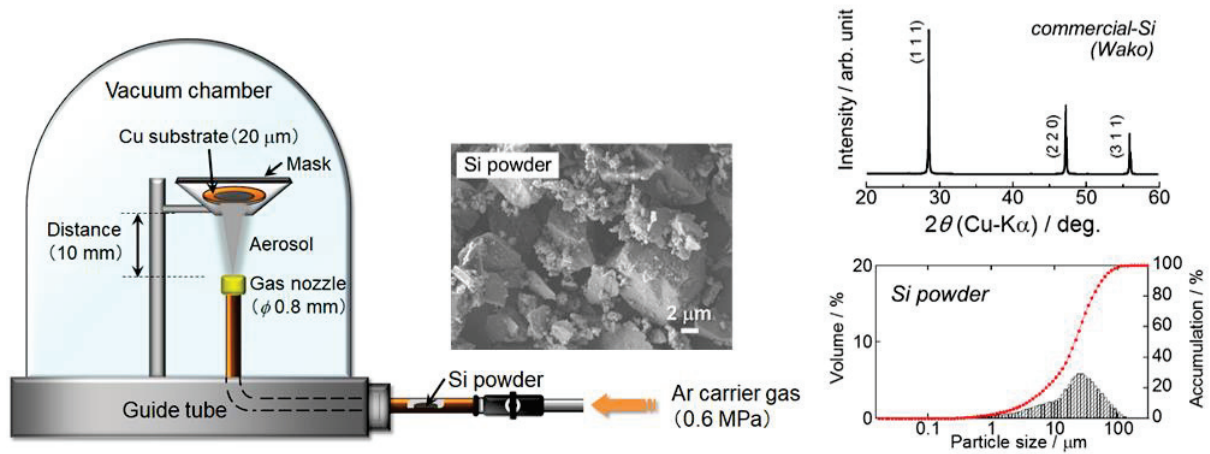
500 Hz with a potential amplitude of 10 mV.

Figure 1-1. (left) Schematic illustration for preparation of Si thick-film electrodes using a gas-deposition method. In this study, Si powder (Wako Pure Chemical Industries, Ltd. 99.9%) with a diameter of 2−10 μm was used as the active material. (right) FE-SEM image, XRD pattern and particle distribution of the Si powder used in this study.
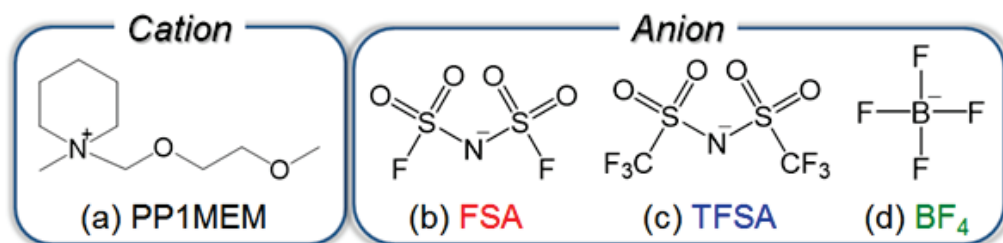
PP1MEM :1-((2-methoxyethoxy)methyl)-1-methylpiperidinium
FSA   :bis(fluorosulfonyl)amide
TFSA   :bis(trifluoromethanesulfonyl)amide
BF$_4$:tetrafluoroborate

Figure 1-2. Cation and anion structures of ionic liquids used in this study. (a) 1-((2-methoxyethoxy)methyl)-1-methylpiperidinium (PP1MEM), (b) bis(fluorosulfonyl)amide (FSA), (c) bis(trifluoromethanesulfonyl)amide (TFSA), and (d) tetrafluoroborate (BF$_4$).

1.3 Results and Discussion

Figure 1-3a shows the dependence of the discharge (Li-extraction) capacity of a Si-alone anode on the cycle number in various ionic liquid electrolyte solutions. For comparison, the result in an organic electrolyte (1 mol dm^{-3} LiTFSA/PC) is also shown. While the discharge capacity of a Si electrode was as high as 3000 mA h g^{-1} in the first cycle in the PC-based electrolyte solution, it rapidly decayed; the Si electrode showed poor cycling stability in the PC-based electrolyte. The rapid capacity-fading resulted from disintegration of the active material layer due to the large change in the volume of Si during Li-insertion and extraction.[33] The volumetric change brought about the cracking and pulverization of Si, and followed by electrolyte decomposition on the exposed surface of the electrode. This phenomenon led to a drop in Coulombic efficiency at around the 30th cycle in the PC-based electrolyte, as shown in Figure 1-3b. The initial discharge capacity of a Si electrode was less than 800 mA h g^{-1} in the BF$_4$-based electrolyte solution. The cycle performance of the electrode in the BF$_4$-based electrolyte was almost the same as that in the PC-based electrolyte; the discharge capacity was less than 200 mA h g^{-1} at the 80th cycle in both electrolytes.
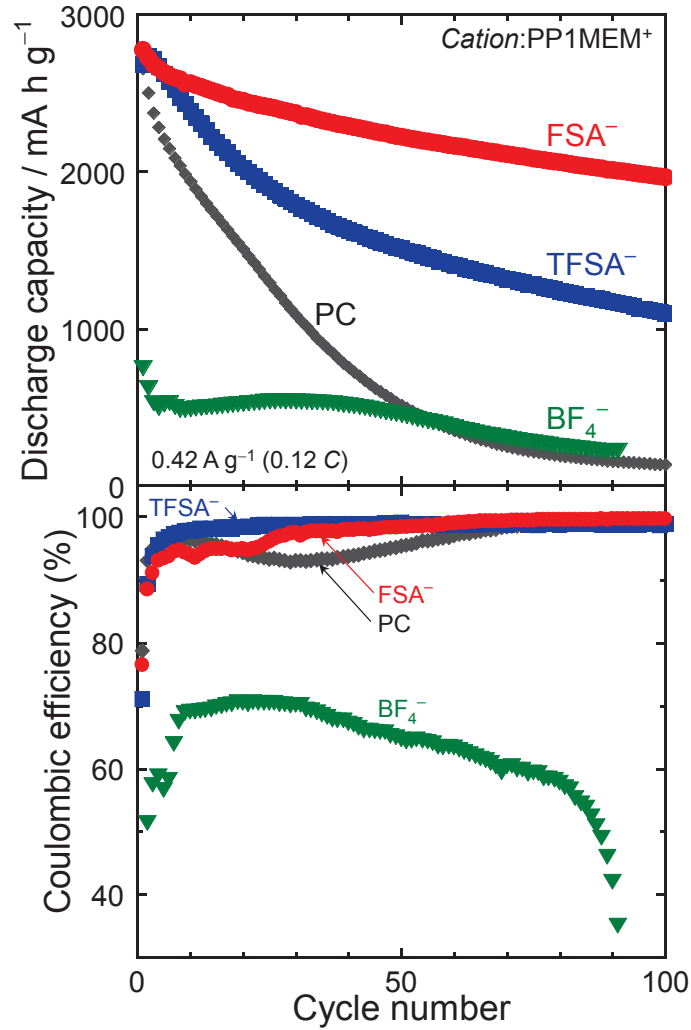
Figure 1-3. Dependence of (a) discharge capacity and (b) coulombic efficiency on cycle number for a Si electrode in 1 mol dm^{-3} LiX/PP1MEM-X. (X: FSA, TFSA, or BF$_4$) For comparison, the performance in 1 mol dm^{-3} LiTFSA/PC is also shown.

Figure 1-4 shows the first charge–discharge profiles of a Si electrode in various electrolytes. A potential plateau was observed at around 0.1 V vs. Li$^+$/Li during the charge (Li-insertion) process in all electrolytes, which corresponds to the Li–Si alloying reaction.[32,33] A huge irreversible capacity was confirmed at around 0.2 V vs. Li$^+$/Li on the charge curve in only the BF$_4$-based electrolyte; an unfavorable reaction appears to occur on the Si electrode. The maximum Coulombic efficiency of the Si electrode in the BF$_4$-based electrolyte was 70%, which was much lower than that in the other electrolytes, as shown in Figure 1-3b.

Generally, an ideal surface film formed on an anode has very low electronic conductivity and high Li^+ conductivity, which suppresses continuous electrolyte decomposition. Therefore, the Coulombic efficiency increases after formation of the surface film. However, the Si electrode maintained low efficiency in the BF_4-based electrolyte. This result suggests that the BF_4-derived surface film did not function suitably as a protective film to prevent continuous electrolyte decomposition.
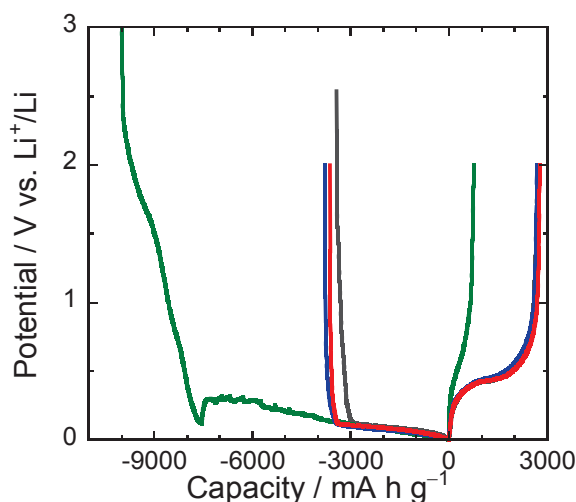

Figure 1-4. The first charge–discharge (Li-insertion/extraction) profiles for Si electrodes in various ionic liquid electrolytes and organic electrolyte.

On the other hand, in the FSA- and TFSA-based electrolytes, the Si anode exhibited a high initial discharge capacity of 2700 mA h g^{-1}, which is almost the same as that in the PC-based electrolyte. This result indicates that desolvation of Li^+ from anions occurred more readily in the FSA- and TFSA-based electrolytes than in the BF_4-based electrolyte. To confirm this assumption, cyclic voltammetry for a simple redox reaction of Li was performed using a Ni electrode as a working electrode, as shown in Figure 1-5. A Ni working electrode was used because it does not change during the Li oxidation/reduction process. In all of the ionic liquid electrolytes, peaks assigned to the deposition and dissolution of Li were observed at around –0.2 V and 0.1 V vs. Li^+/Li, respectively.[19,49,50] These peaks were large in the order

FSA- > TFSA- > BF_4-based electrolytes, which corresponds to the ionic association tendency of the Li salt.[51] This result indicates that the desolvation of Li^+ from the anion most easily occurs in the FSA^--based electrolyte, whereas the desolvation from BF_4 does not occur as easily because of the stronger electrostatic interaction between Li^+ and BF_4. Therefore, the above assumption should be valid. In the first cycle, broad reduction peaks were observed at *ca.* 1.4 V and 1.6 V vs. Li^+/Li in the FSA- and TFSA-/BF_4-based electrolytes, respectively. Although the structure of the cation in all of the ionic liquids was the same, they had different reduction potentials. This suggests that the anion species in the electrolytes decomposed at each potential.[52] and the surface film that consisted of the decomposition products should affect the cycling performance of the Si electrode.

The initial Coulombic efficiency in the FSA- and TFSA-based electrolytes was about 70% at the initial cycle and increased to almost 100% in the subsequent cycle. On the other hand, in the BF_4-based electrolyte, the efficiency was lower in all cycles. This indicates that the surface films formed in the FSA- and TFSA-based electrolytes have much better insulation properties. Therefore, the FSA- and TFSA-derived surface films would act as a protective film to effectively prevent continuous decomposition of the electrolytes.
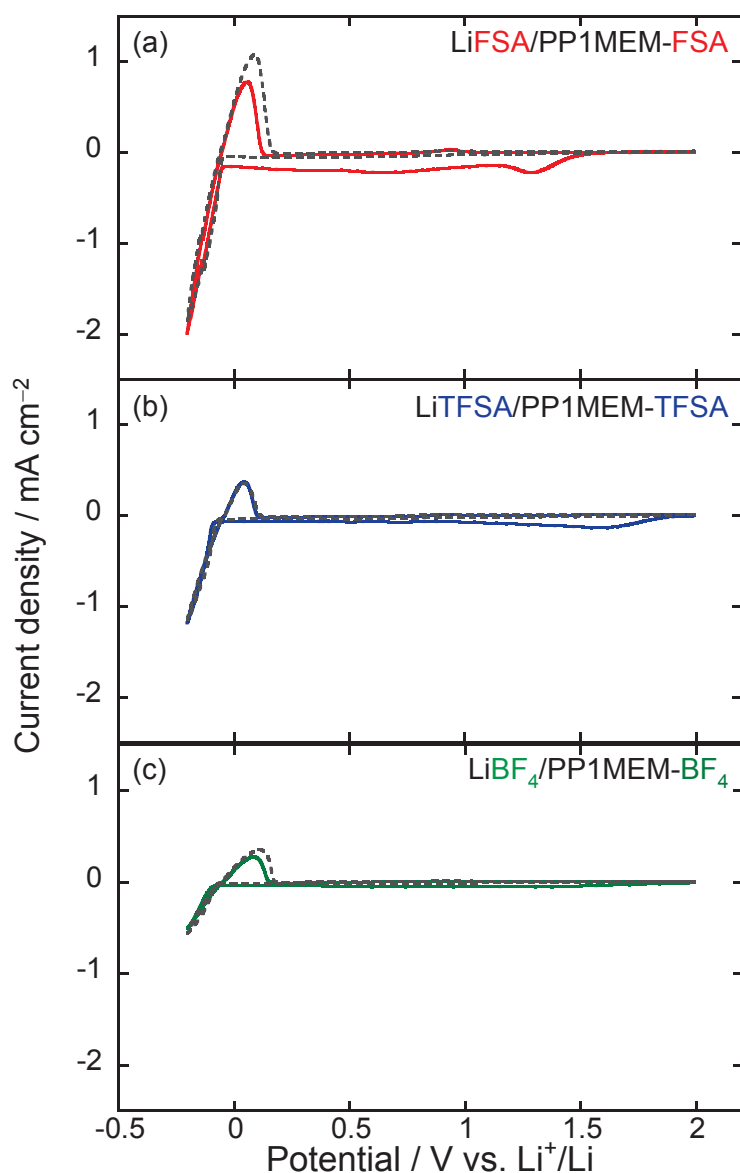
15

Figure 1-5. Cyclic voltammogram for Li deposition/dissolution on/from a Ni electrode in 1 mol dm^{-3} LiX/PP1MEM-X. (X: (a) FSA, (b) TFSA and (c) BF$_4$) Solid and dotted lines show first and second cycles, respectively. Scan rate : 1 mV s^{-1}

As shown in Figure 1-3a, the electrode retained a discharge capacity of 2000 mA h g^{-1} after 100 cycles in the FSA-based electrolyte, which is twice that in the TFSA-based electrolyte. It is considered that cycling stability is attributed to the difference of composition of the surface film. The surface film on Li electrode is composed of LiF, Li$_2$SO$_4$, Li$_2$S$_2$O$_4$, Li$_2$NSO$_2$CF$_3$, Li$_y$C$_2$F$_x$, LiSO$_2$CF$_3$ and others in TFSA-based electrolyte.[53,54] On the other

hand, the FSA-derived surface film is composed of LiF, LiOH, Li_2O, Li_2SO_4, SO_2F etc.[17,55] These insoluble Li salts on the surface of the electrodes are probably responsible for the passivation of the electrodes. However, it is unclear that which component contributes to improve the cycling stability. Piper *et al.* investigated the decomposition mechanism of the FSA and TFSA anions based on molecular dynamics simulations.[17] They reported that the S-F bond in FSA is broken preferentially, and F^- is rapidly released to form LiF, whereas LiF is not formed as readily in TFSA. It is well known that LiF improves the structural stability of the surface film.[56] Hence, the FSA-derived surface film is more stable and should contribute to better cycling performance.

Although the FSA-based ionic liquid electrolyte improved the cycling performance of the Si electrode, gradual capacity-fading still occurred. We have demonstrated that the cycle performance can be remarkably enhanced by controlling Li-insertion/extraction, in moderation.[57] A charge–discharge cycling was performed with a Li-extraction capacity limitation of 1000 mA h g^{-1} in the FSA- and TFSA-based electrolytes, as shown in Figure 1-6. In the $TFSA^-$-based electrolyte, the Si electrode maintained a reversible capacity of 1000 mA h g^{-1} until about the 800th cycle. On the other hand, the Si electrode in the FSA-based electrolyte exhibited better cycle performance with a discharge capacity of 1000 mA h g^{-1} even after *ca.* 1600 cycles. Capacity limitation dramatically improved the cycling stability, since the accumulation of severe stress was suppressed by moderation of the change in the volume of Si. Notably, the cycle life of the electrode in the FSA-based electrolyte was twice as long as that in the TFSA-based electrolyte. Hence, the superiority of the FSA-based electrolyte became clear when the capacity was limited.
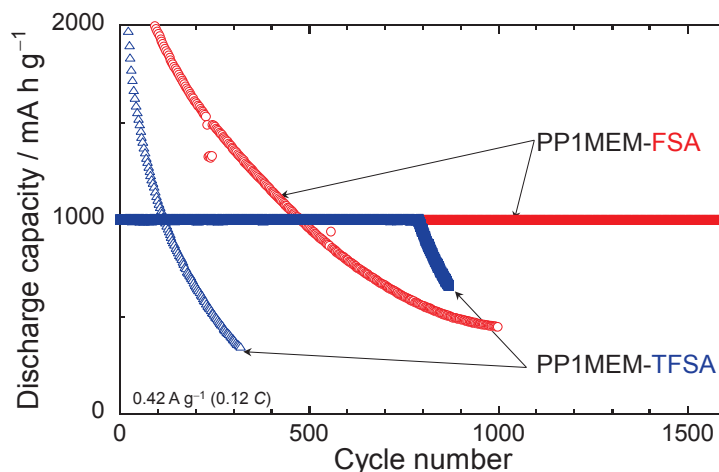
17

Figure 1-6. Variation in discharge capacity of a Si electrode in 1 mol dm^{-3} LiFSA/PP1MEM-FSA or LiTFSA/PP1MEM-TFSA versus number of cycles at a fixed Li-extraction level of 1000 mA h g^{-1}. For comparison, the performance without capacity limitation is also plotted.

Rate performance is one of the most important characteristics of LIBs, especially when used in electric vehicles. Thus, the rate capability of a Si electrode in the ionic liquid electrolytes was investigated, as shown in Figure 1-7. The electrodes showed reversible capacities of 700 mA h g^{-1}, 100 mA h g^{-1}, and 1000 mA h g^{-1} at a high current rate of 6 C (21 A g^{-1}) in the FSA-, TFSA-, and PC-based electrolytes, respectively. As shown in Table 1-1, the PC-based electrolyte exhibited the highest ionic conductivity of 5.51 mS cm^{-1}. In addition, the conductivity of the FSA-based electrolyte (2.06 mS cm^{-1}) was three times that of the TFSA-based electrolyte (0.66 mS cm^{-1}). Since there are no electroneutral molecules in an ionic liquid, electrostatic interaction between the cation and anion immensely influences on the viscosity and ionic conductivity of the ionic liquid. The electrostatic interaction between Li^{+} and FSA is weaker compared with that between Li^{+} and TFSA. In addition, it has been confirmed that FSA-based ionic liquid shows a lower viscosity than TFSA-based one.[58] This is one of the reasons why FSA-based electrolyte has higher ionic conductivity compared to TFSA-based electrolyte. Li-insertion into a Si anode proceeds via several steps: (1) Li^{+} transport in the electrolyte bulk, (2) desolvation of Li^{+} from ionic liquid anions or organic

molecules, (3) Li$^+$ transport in an electric double layer and/or a solid electrolyte interphase, and (4) an alloying reaction of Si with Li.[59] Under a high rate of 6 *C*, Li$^+$ transport, *i.e.* ionic conductivity in the electrolyte bulk, dominantly affects the rate capability. Consequently, a good high-rate performance was achieved only in the FSA$^-$-based electrolyte, even though FSA$^-$ and TFSA$^-$ are based on the same amide. When the current rate was back to the initial value of 0.12 *C*, the Si electrode showed a reversible capacity of 1200 mA h g^{-1} at the 36th cycle in the PC-based electrolyte. In contrast, the discharge capacity of the electrode recovered to 2500 and 2000 mA h g^{-1} at the 36th cycle in the FSA$^-$- and TFSA$^-$-based electrolytes, respectively, which are both higher than the capacity in the PC-based electrolyte. These results indicate that the Si electrode was disintegrated in the PC-based electrolyte at a high current rate of 6 *C*, whereas deterioration of the electrode was almost negligible in the FSA$^-$- and TFSA$^-$-based electrolytes. In addition, it is considered that the discharge capacity-fading in the FSA$^-$- and TFSA$^-$-based electrolytes at 6 *C* is mainly caused by limitation of the rate of Li$^+$ diffusion in the electrolyte bulk.
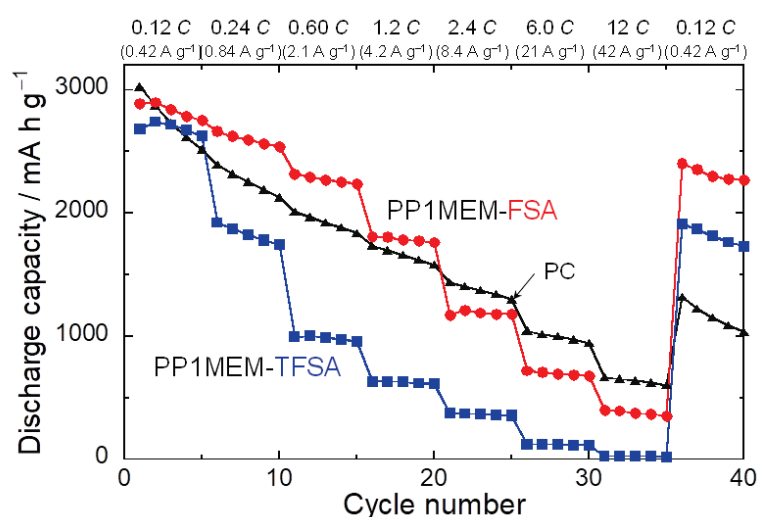

Figure 1-7. Rate capability for a Si electrode in 1 mol dm^{-3} LiFSA/PP1MEM-FSA, LiTFSA/PP1MEM-TFSA, and LiTFSA/PC at various current rates from 0.12 *C* to 12 *C*.

Table 1-1. Ionic conductivity of electrolytes used in this study at 303 K.

Electrolyte		Conductivity / mS cm^{-1}
Li-salt	Solvent	
LiFSA	PP1MEM-FSA	2.06
LiTFSA	PP1MEM-TFSA	0.66
LiTFSA	PC	5.51

1.4 Summary

The effect of the structure of the anion in an ionic liquid electrolyte on the electrochemical performance of a Si-alone anode for use in LIBs was investigated. The electrode showed better cycle performance in FSA$^-$- and TFSA$^-$-based electrolytes than in a BF$_4$$^-$-based electrolyte; the performance of the Si electrode is improved in some, but not all, ionic liquid electrolytes. The electric conductivities of the surface films formed in the FSA$^-$- and TFSA$^-$-based electrolytes would be lower than those in BF$_4$$^-$- and PC-based electrolytes. A Si-alone anode also exhibited excellent cycle performance with a discharge capacity of 1000 mA h g^{-1} beyond 1600 cycles in the FSA$^-$-based electrolyte under Li-extraction capacity limitation, which results from the structural stability of the surface film with LiF. A high rate performance was achieved with a reversible capacity of 700 mA h g^{-1} even at 6 C in the FSA$^-$-based electrolyte due to the high conductivity of the electrolyte. Consequently, the FSA$^-$-based ionic liquid electrolyte is the most promising electrolyte solution for next-generation LIBs with a Si-based anode.

Chapter 2

Anion Effects in Ionic Liquid Electrolytes on Electrochemical Performance of Annealed Ni–P/(etched Si) Composite Anode for LIBs

2.1 Introduction

As mentioned in chapter 1, Silicon (Si) is a promising active material as an anode material due to its remarkably high theoretical capacity of 3580 mA h g^{-1} ($Li_{15}Si_4$).[1,2] However, Si shows a poor cycle stability because it goes through huge volumetric changes during lithiation/delithiation reactions,[3,4] which generates high stresses and large strains in the active material. The accumulation of strains during repeated charge–discharge cycling results in disintegration of the active material layer. To address the issue, we have developed composite electrodes such as $LaSi_2$/Si (or $Si_{1-x}Ge_x$),[60,61] Ni–P/Si,[62,63] and TiO_2/Si,[64] which have both good cycle stability and high capacity. Among them, an electrode consisted of annealed Ni–P/(etched Si) particles exhibited an excellent cycle performance with a reversible capacity of 2000 mA h g^{-1} after 100 cycles in a conventional organic electrolyte.[58] The annealed Ni–P/(etched Si) powder is prepared by following processes; (1) etching Si with hydrofluoric acid to remove its surface oxide, (2) coating etched Si with Ni–P consisted of Ni and Ni_3P by an electroless deposition (ELD) method, and (3) annealing Ni–P/(etched Si) at 800 $^{\circ}$C. A Ni–P coating layer acts as a Li diffusion pathway in the active material layer, and releases the stresses. In addition, etching and annealing can enhance the adhesion between Si surface and Ni–P layer, which results in its improved performance compared to an untreated Ni–P/Si electrode.

In chapter 1, the author also demonstrated that the cycle stability of a Si-alone electrode was remarkably improved by using the ionic liquid of

21

1-((2-methoxyethoxy)methyl)-1-methylpiperidinium bis(fluoromsulfonyl)amide (PP1MEM-FSA). While it was reported that ionic liquid electrolytes can enhance the cycle performance of Si-based electrodes by some researchers,[17,65–67] the optimization of anion structure in an ionic liquid electrolyte has not been sufficiently studied yet. The author have investigated the effect of anion structure in an ionic liquid electrolyte to improve the electrochemical performance of the Si-alone anode, as shown in chapter 1.[19] We have also found that an annealed Ni–P/(etched Si) electrode exhibits better cycle stability in an ionic liquid electrolyte of lithium bis(trifluoromethanesulfonyl)amide/*N*-methyl-*N*-propylpyrrolidinium bis(fluorosulfonyl) amide (LiTFSA/Py13-FSA) under a charge capacity limit. However, the ionic liquid electrolyte is not necessarily the best for the electrode. In this study, to improve the electrochemical performance of annealed Ni–P/(etched Si) anode for LIBs, the author determined the effect of anion structure in an ionic liquid electrolyte on its performance. The author adopted ionic liquid electrolytes consisted of piperidinium-based cation and amide-based anion, where the anion of the Li salt was the same as that of the ionic liquid unless otherwise stated.

2.2 Experimental Details

We designed annealed Ni–P/(etched Si) powder, and commissioned Hitachi Metals Neomaterial, Ltd. to prepare it. Chemical etching with hydrofluoric acid was performed to remove a natural dioxide film on the Si surface accompanied by roughening of the surface. Etched Si was coated with Ni–P particles by the ELD method,[6] and the powders were subsequently annealed at 800 $^{\circ}$C in an inert gas atmosphere. An annealed Ni–P/(etched Si) electrode was prepared by the gas–deposition (GD) method which requires no binders and conductive additives. The detailed conditions of GD were described in chapter 1. The author

fabricated 2032-type coin cells consisted of annealed Ni–P/(etched Si) electrode as working electrode, Li foil (Rare Metallic, 99.90%, thickness: 1.0 mm) as counter electrode, ionic liquid electrolyte, and glass fiber filter as separator. The areas of the active material layer and Li foil in the cell are 0.5 cm^2 and 2.0 cm^2, respectively. The electrolyte solution used in this study was 1 mol dm^{-3} (M) lithium bis(fluorosulfonyl)amide (LiFSA) dissolved in 1-((2-methoxyethoxy)methyl)-1-methylpiperidinium bis(fluorosulfonyl)amide (PP1MEM-FSA). In addition, 1 M LiTFSA dissolved in 1-((2-methoxyethoxy)methyl)-1-methylpiperidinium bis(trifluoromethanesulfonyl)amide (PP1MEM-TFSA) was adopted. The electrolyte preparation and cell assembly were conducted in an Ar–filled glove box (Miwa MFG, DBO–2.5LNKP–TS) with an oxygen concentration below 1 ppm and a dew point below –100 $^{\circ}$C. A galvanostatic charge–discharge test was carried out using an electrochemical measurement system (HJ1001SM8, Hokuto Denko Co., Ltd.) in a potential range between 0.005 and 2.000 V vs. Li$^+$/Li at 303 K. The current density was set at 0.36 A g^{-1} (0.1 *C*) in the 1st cycle and 1.44 A g^{-1} (0.4 *C*) after the 2nd cycle. Electrochemical impedance spectroscopic (EIS) analysis was performed at 0.005 V vs. Li$^+$/Li in the frequency range from 100 kHz to 10 mHz with amplitude of 5 mV. The author used three-electrode cell for EIS measurement to reduce the effect from counter electrode. The surface morphologies of the annealed Ni–P/(etched Si) electrodes after charge–discharge cycle were observed by a field-emission scanning electron microscope (FE-SEM: JSM-6701F, JEOL Co., Ltd.).

2.3 Results and Discussion

Figure 2-1a shows the initial three charge–discharge curves of annealed Ni–P/(etched Si) electrodes in 1 M LiFSA/PP1MEM-FSA. In addition, the results in 1 M LiTFSA/PP1MEM-TFSA were also plotted. The electrode exhibited a discharge capacity of

2200 and 2400 mA h g^{-1} at the first cycle in the FSA- and TFSA-based electrolytes, respectively. In addition, a potential gradient between 0.8 and 2.0 V vs. Li^+/Li appeared on charge curves in each electrolyte, which results in a formation of surface film through reductive decomposition of the electrolyte.[52,68–70] Since the surface film has an insulation property and Li^+ conductivity, it can prevent the electrolyte from continuing to be reductively decomposed. Therefore, the potential gradient disappeared after the second cycle. Although the electrode showed a relatively low discharge capacity of 1560 mA h g^{-1} at the second cycle in the TFSA-based electrolyte, a discharge capacity of 2170 mA h g^{-1} was maintained in the FSA-based electrolyte. At the third cycle, discharge capacities were almost the same as those at the second cycle regardless of the electrolyte. Thus, the author concluded that serious degradation of the electrode did not occur at the initial cycles.

In Figure 2-1b, the annealed Ni–P/(etched Si) electrode exhibited an excellent cycle stability with a discharge capacity of 1890 mA h g^{-1} in the FSA-based electrolyte even after 250 cycles. In addition, the capacity decay hardly occurred in the electrolyte. In contrast, the electrode exhibited only 540 mA h g^{-1} in the TFSA-based electrolyte after 250 cycles, which suggests that the electrode disintegrated. The author proposed that the cycle stability is related to the structural stability of a surface film on the electrode. The FSA-derived film is mainly comprised of LiF which enhances structural stability of the film,[17] whereas LiF content in the TFSA-derived film is relatively low. Therefore, it is considered that the cycle stability of the electrode in the FSA-based electrolyte was superior to that in the TFSA-based electrolyte. In addition, the cycle stability of the annealed Ni–P/(etched Si) electrode was higher than that of a Si-alone electrode.[71] This is because a Ni–P coating layer accommodated stresses caused by a huge volumetric change of Si active material during charge–discharge cycle and suppressed a degradation of the active material layer. No drop of the Coulombic

efficiency was observed regardless of the kind of electrolytes. This result indicates that drastic electrode disintegration did not occur.

We have demonstrated that a cycle life of a Si-alone electrode can prolong by controlling the amount of Li insertion–extraction.[72] Thus, the author expected the cycle stability of the Ni–P/Si electrode is also improved by a charge (Li-insertion) capacity limit. Figure 2-1c shows the long cycle performance of the annealed Ni–P/(etched Si) electrode in ionic liquid electrolytes with a charge capacity limit of 1000 mA h g^{-1}. In the TFSA-based electrolyte, a discharge capacity decayed at about 160 cycles. On the other hand, in the FSA-based electrolyte, the electrode exhibited an excellent cycle life with a reversible capacity of 1000 mA h g^{-1} over *ca*. 1000th cycle. Consequently, it is obvious that the anion of an ionic liquid is very important to enhance cycle stability of Si-based electrodes.

As both energy and power densities are critical factors in LIBs, the author measured a rate capability of the annealed Ni–P/(etched Si) electrode, as shown in Figure 2-1d. In the TFSA-based electrolyte, the electrode only retained 50% of the first discharge capacity at 0.5 *C* and exhibited almost no capacity at 5.0 and 10 *C*. Potential plateaus were hardly observed in charge–discharge curves as shown in Figure 2-2a. In contrast, in the FSA-based electrolyte, the electrode maintained 60% of the initial capacity at 2.0 *C*, and showed a discharge capacity of 500 mA h g^{-1} even at 10 *C*, which is higher than the theoretical capacity of graphite (372 mA h g^{-1}). The plateaus also appeared in the FSA-based electrolyte, as shown in Figure 2-2b. When the current rate was back to 0.1 *C* at the 36th cycle, the capacities were almost the same as the first capacity in each electrolyte. Thus, the capacity fading at the high current rate would not be attributed to the electrode deterioration. The capacity gradually decreased in the TFSA-based electrolyte in subsequent charge–discharge test at 0.1 *C,* whereas that hardly decreased in the FSA-based electrolyte, as shown in Figure 2-3. The

difference should be attributed to the structural stability of a surface film on the electrode as mentioned above.
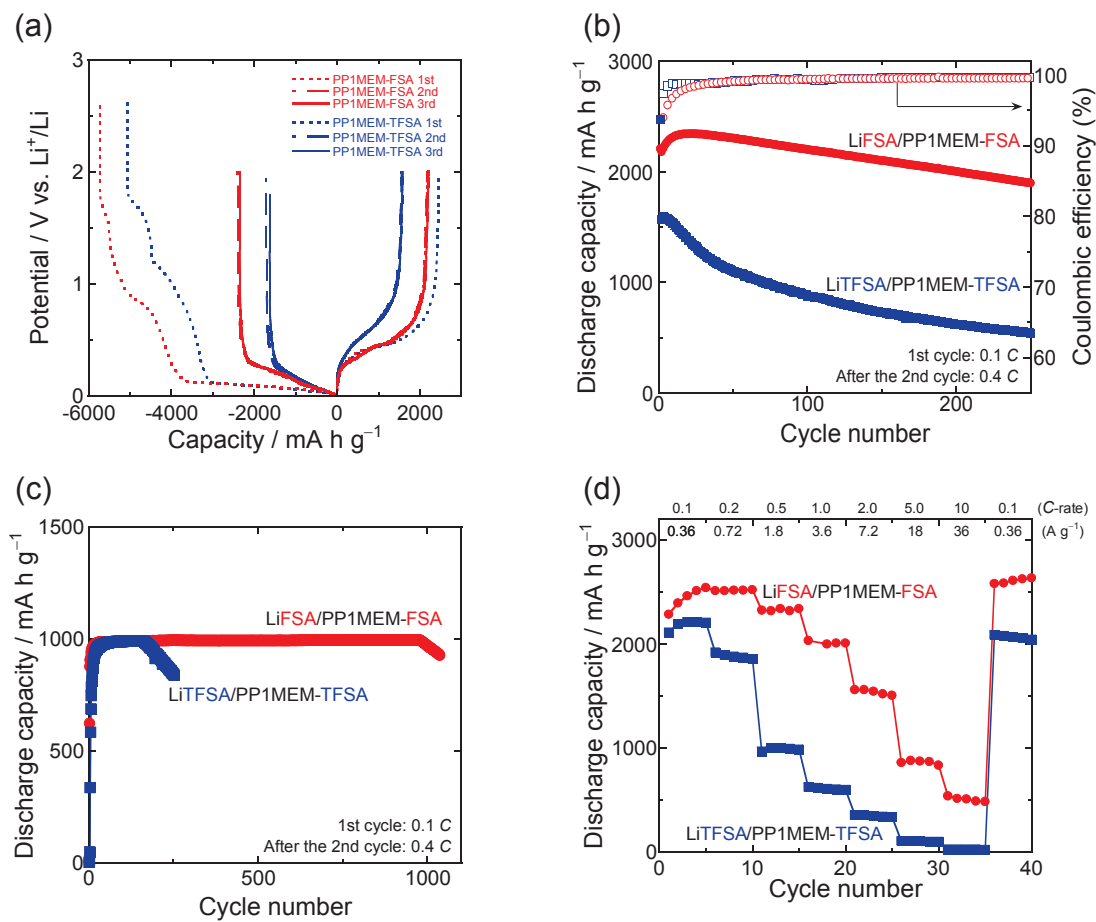

Figure 2-1. (a) The initial charge–discharge curves, cycling performances (b) without and (c) with charge (lithiation) capacity limit at 1000 mA h g^{-1}, and (d) rate capability of annealed Ni–P/(etched Si) electrodes in 1 M LiFSA/PP1MEM-FSA or LiTFSA/PP1MEM-TFSA.
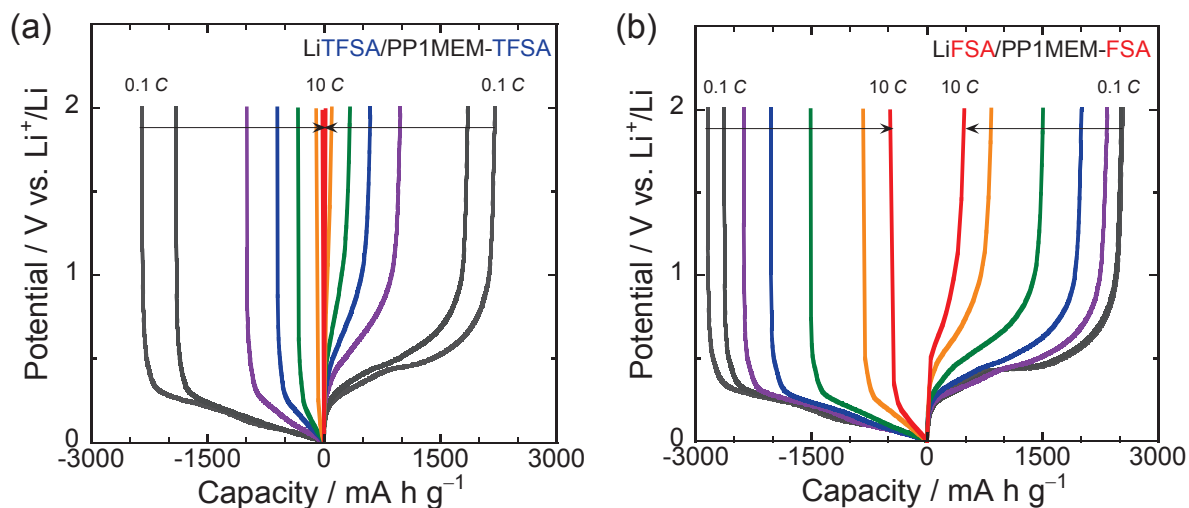
Figure 2-2. Charge–discharge curves of annealed Ni–P/(etched Si) electrodes in 1 M (a) LiFSA/PP1MEM-FSA or (b) LiTFSA/PP1MEM-TFSA at various current rate from 0.12 to 12 *C*. Black, grey, purple, blue, green,　orange, and red curves correspond to results at 0.1, 0.2, 0.5, 1, 2, 5, and 10 *C*, respectively.
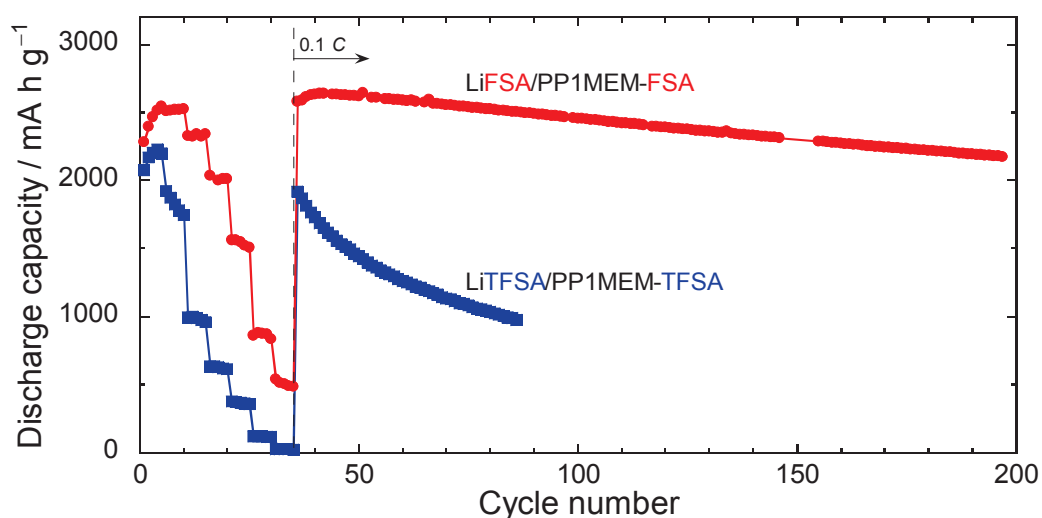

Figure 2-3. Cycle performance of annealed Ni–P/(etched Si) electrodes in 1 M LiFSA/PP1MEM-FSA or LiTFSA/PP1MEM-TFSA at 0.1 *C* after rate performance measurement.

In the conventional evaluation method of rate capability, it is difficult to discriminate the reason for capacity decay under high current density. To exclude the capacity decay caused by the electrode degradation, the author investigated the rate capability of the annealed Ni–P/(etched Si) electrode with charge capacity limit in the FSA-based electrolyte

(Figure 2-4). A discharge capacity of 1000 mA h g^{-1} was maintained until a current rate of

2.0 *C*. Although capacity decay was observed at 5.0 *C*, the capacity was recovered when the

current rate was back to 0.1 *C*. This result suggests that the capacity decay is caused by

limitation of mass transfer. The capacity of 1000 mA h g^{-1} was retained without hardly effect

of mass transfer until 2.0 *C*. Therefore, the electrode in the FSA-based electrolyte would

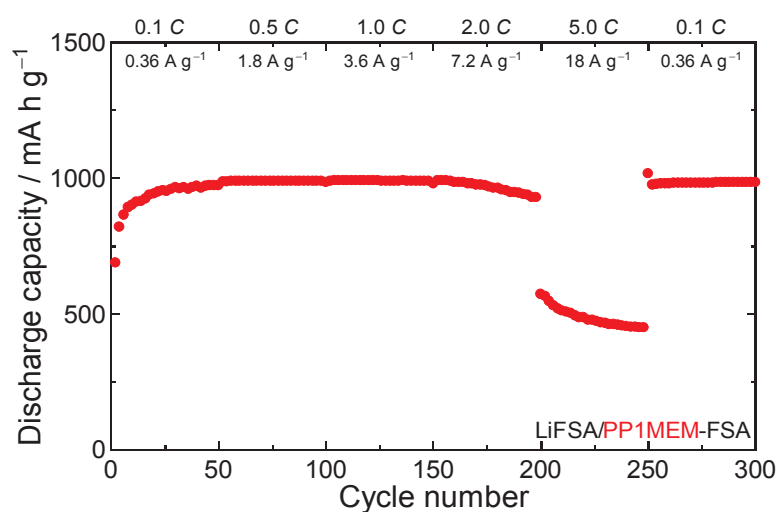stably cycle until a relatively high rate of 2.0 *C*.

Figure 2-4. Rate capability of annealed Ni–P/(etched Si) electrodes in 1 M LiFSA/PP1MEM-FSA at various current rate from 0.1 to 5 *C* at a fixed Li-insertion level of 1000 mA h g^{-1}.

To reveal the reason for the difference in the cycle stability of the annealed Ni–

P/(etched Si) electrode (Figures 2-1b), the author observed the surface morphology by

FE-SEM. Figures 2-5a-d show FE-SEM image of the electrode surface after 1 and 50 cycles.

No cracks were observed on the electrode surface after the 1st cycle regardless of electrolyte

(Figures 2-5a and c), which suggests that the Ni–P coating layer alleviates the stresses arising

from the change in the volume of Si layer during the charge–discharge reaction.[73] On the

other hand, the crack generated on the electrode surface after the 50th cycle, as shown in

Figures 2-5b and d. Since there is no great distinction between the TFSA- and FSA-based

electrolytes, the reason of capacity decay in the TFSA-based electrolyte in Figure 2-1b cannot

be explained by only surface morphology. Thus, EIS measurement was conducted to investigate electrochemical behavior of Li^+ at the interface between the electrode and the electrolyte.
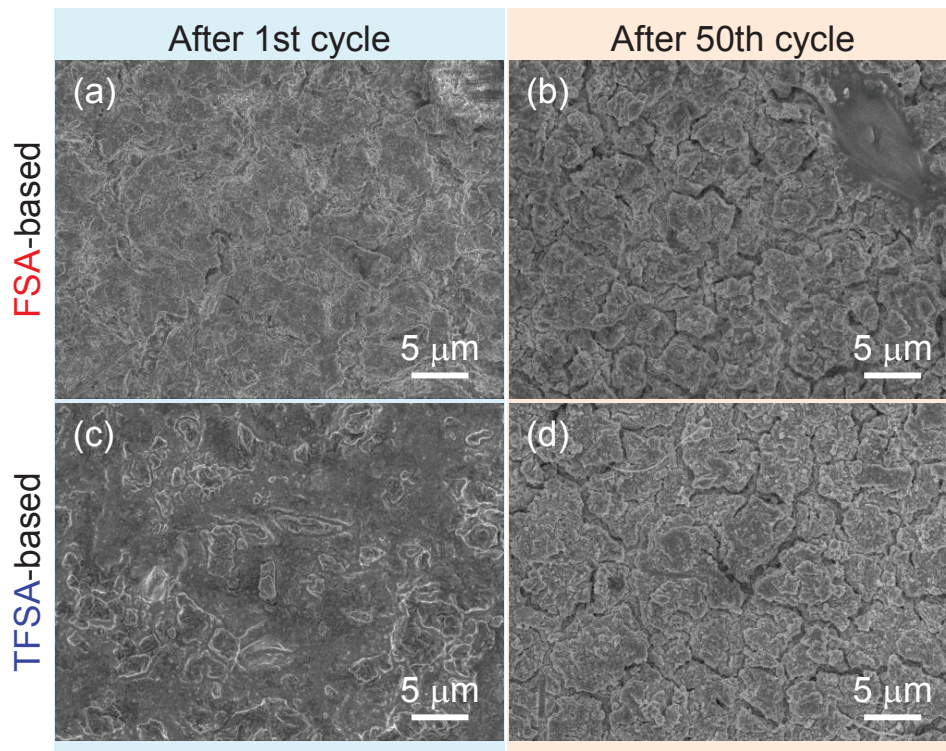

Figure 2-5. FE-SEM images of annealed Ni–P/(etched Si) electrodes after (a, c) 1st or (b, d) 50th cycle. The electrodes were cycled in (a, b) 1 M LiFSA/PP1MEM-FSA or (c, d) 1 M LiTFSA/PP1MEM-TFSA.

Figures 2-6a and b display Nyquist plots of the annealed Ni–P/(etched Si) electrodes charged at 0.005 V vs. Li^+/Li after 10 cycles in each electrolyte. Solution resistance (R_{sol}) corresponds to ionic conductivity of the electrolyte, which reflects Li^+ transport in the bulk of electrolyte. The first semicircle in high frequency region denotes interfacial resistance (R_{if}) which is associated with interfacial Li^+ transfer processes. They include desolvation of anions from Li^+ as well as Li^+ transport in electrical double layer and/or a surface layer induced by the decomposition of electrolyte.[74] The second semicircle corresponds to charge transfer

29

resistance (R_{ct}), and is related to the process of Li−Si alloying reaction.[59] The straight line with a slope of approximately 45° in the low frequency named as Warburg impedance (Z_w) is derived from solid state diffusion of Li in Si layer. Resistances of these components were analyzed by using an equivalent circuit as shown in Figure 2-6c, and calculated resistances were summarized in Table 2-1. R_{sol} in the FSA-based electrolyte was nearly one third of that in the TFSA-based electrolyte, which is attributed to difference in conductivity of each electrolyte.[71] R_{if} in the FSA-based electrolyte was much less than that in the TFSA-based electrolyte, which indicates that Li$^+$ transferred smoothly at the electrode−electrolyte interface. In addition, R_{ct} was lower in the FSA-based electrolyte. This suggests that Li–Si alloying reaction easily occurs due to smooth Li$^+$ supply to the interface. However, it must be careful that an EIS spectrum for a two-electrode cell includes information from both electrode/electrolyte interfaces. To discuss more correctly, the author performed EIS measurement for Li/Li symmetric cell in each electrolyte and Figure 2-7 shows the results. These lower $R_{sol,}$ R_{if} and R_{ct} should lead to high cycle performance and good rate capability. The author considered that this difference in resistance is attributed to the coordination environment around Li$^+$ and the property of surface film formed on the annealed Ni–P/(etched Si) electrode. The author have demonstrated that the ionic association tendency of the Li salt corresponds to the desolvation of the anion from Li$^+$ more easily occurs in the FSA-based electrolyte. This should be the reason why R_{if} and R_{ct} in the FSA-based electrolyte is lower.
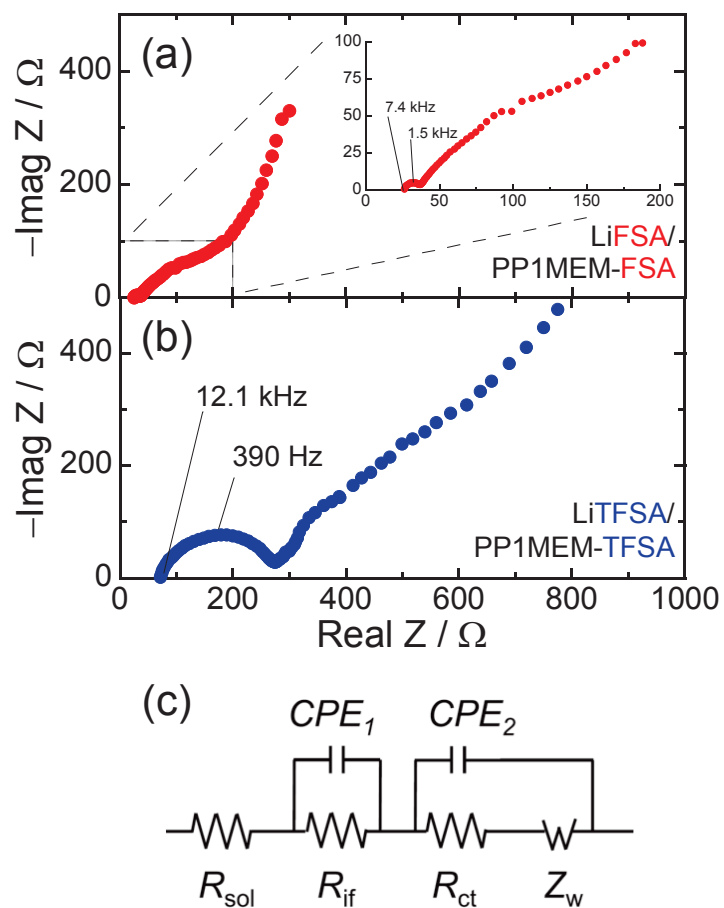
Figure 2-6. Nyquist plots of the annealed Ni–P/(etched Si) electrode at the 10th charged state (0.005 V vs. Li$^+$/Li) in 1 M (a) LiFSA/PP1MEM-FSA and (b) LiTFSA/PP1MEM-TFSA. (c) Equivalent circuit for impedance analysis in this study.

Table 2-1. Summary of EIS analyses for annealed Ni–P/(etched Si) electrodes at 10th cycle in figure 2-6 and conductivity of electrolytes.

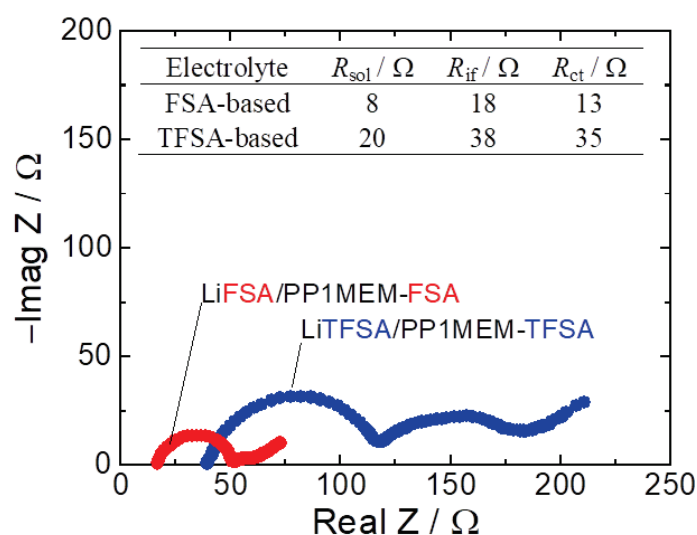|	R_{sol} / Ω	R_{if} / Ω	R_{ct} / Ω	Conductivity / mS cm^{-1}
FSA-based	26.1	8.8	78.5	2.06
TFSA-based	72.0	210	260	0.66

Figure 2-7. Nyquist plots of the Li/Li symmetric cells in 1 M LiFSA/PP1MEM-FSA and LiTFSA/PP1MEM-TFSA. Inset table shows the fitting results.

2.4 Summary

The author investigated the effect of the anion structure in an ionic liquid electrolyte on the electrochemical performance of an annealed Ni–P/(etched Si) anode for LIBs. The electrode showed better cycle performance and rate capability in the FSA-based electrolyte than those in the TFSA-based electrolyte. The surface morphology of the electrode after the cycles was almost the same regardless of electrolyte. On the other hand, R_{sol} of the FSA-based electrolyte was lower, contributing to high rate performance. In addition, lower R_{if} and R_{ct} enhances cycle performance, which is attributed to relatively facile desolvation of FSA^- from Li^+. As a consequence, the FSA-based ionic liquid electrolyte is able to improve the electrochemical performance of the annealed Ni–P/(etched Si) electrode, and contributes to realization of next-generation LIBs with a Si-based anode.

Chapter 3

Elucidation of the Reaction Behavior of Silicon Anodes in a Bis(fluorosulfonyl)amide-Based Ionic Liquid Electrolyte

3.1 Introduction

In chapter 1 and 2, the author revealed that FSA-based ionic liquid electrolyte can enhance the electrochemical performance of Si-based anodes for LIBs. Meanwhile, some researchers also reported that an effectiveness of the FSA-based electrolyte for the Si-based electrode. Lee *et al.* demonstrated the decomposition mechanism of FSA anion on a Si-based electrode using ab initio molecular dynamics simulation.[17] The S-F bond of the FSA anion rapidly breaks and releases F^-, most likely forming LiF in the surface film, in combination with the release of SO_2. They speculated that the fast release of F^- and SO_2 is associated with the superior cycling performance in the FSA-based electrolyte. They also examined changes in the mass of the electrode during the first charge–discharge cycle using an in situ electrochemical quartz crystal microbalance. The results revealed that the surface film derived from FSA is stable compared with that derived from an organic electrolyte. Ishikawa *et al.* investigated the cycling performance of a silicon–nickel–carbon composite electrode in an FSA-based electrolyte.[75] Based on the results of electrochemical impedance spectroscopy, they demonstrated that the excellent performance in an FSA-based electrolyte is associated with very low interfacial and charge–transfer resistances at the Si-based composite electrode. The authors confirmed the much lower resistances of a Si-alone electrode in an FSA-based electrolyte compared to that in a bis(trifluoromethanesulfonyl)amide-based electrolyte.[17] Although the composition of the surface film and the interfacial resistance between the electrode and electrolyte have been studied previously as described above, the distribution of the lithiation–delithiation reaction on a Si electrode in an FSA-based electrolyte is not yet

33

fully understood. The lithiation distribution is important for understanding the utilization ratio of active material, which should contribute to the development of electrodes with higher capacity and longer life.

Soft X-ray emission spectroscopy (SXES) is a method for elemental analysis that can detect Li, whereas it is difficult to observe Li with other methods such as energy dispersive X-ray spectroscopy. Thus, with SXES, we can directly observe the lithiation distribution in the electrode. On the other hand, Raman spectroscopy enables us to identify the crystallinity of Si, since Raman bands of crystalline Si (*c*-Si) and amorphous Si (*a*-Si) appear at 520 and 490 cm^{-1}, respectively.[76–78] After *c*-Si electrochemically reacts with Li at room temperature to form $Li_{15}Si_4$ and then Li is extracted, it turns into *a*-Si.[2,31] Taking advantage of this phenomenon, we previously visualized for the first time the distributions of *c*-Si and *a*-Si on an electrode surface after cycling by Raman mapping analysis.[57] The results revealed that the lithiation–delithiation reaction proceeds uniformly on the electrode surface in a certain ionic liquid electrolyte, which may contribute to the excellent cycling performance. However, we did not determine whether the lithiation–delithiation reaction inside the electrode also proceeds uniformly. Hence, the interior of the electrode need to be investigated by cross-sectional observation. In chapter 3, the author tried to elucidate the reaction behavior of Si-alone electrodes in an FSA-based ionic liquid electrolyte based on cross-sectional scanning electron microscopic observation, SXES, and Raman spectroscopy. In addition, the author attempted to further improve the cycling performance by controlling the extent of Li-extraction.

3.2 Experimental Details

Electrode preparation and charge–discharge test

A Si-alone electrode was prepared by the gas-deposition (GD) method. While conventional electrode preparation using a slurry requires not only active materials but also a binder and conductive agent, the GD method does not require these additives. Thus, this method is suitable for elucidating the reaction behavior of a Si electrode. The detailed conditions have been described in chapter 1. The weight of the deposited active materials, the deposition area on the Cu substrate, and the thickness of the active material layer were 30 ± 2 µg, $0.5\times0.5\times\pi$ cm^2, and *ca.* 1.6 ± 0.3 µm, respectively. The author assembled a 2032-type coin cell, which consisted of the Si-alone electrode as a working electrode, a glass fiber filter (Whatman GF/A) as a separator, and Li metal foil (Rare Metallic Co., Ltd., 99.90%) as a counter electrode. The ionic liquid electrolyte solution was 1 mol dm^{-3} (M) lithium bis(fluorosulfonyl)amide (LiFSA) dissolved in 1-((2-methoxyethoxy)methyl)-1-methylpiperidinium bis(fluorosulfonyl)amide (PP1MEM-FSA). PP1MEM cation was used because it can increase the initial capacity of the Si electrode.[71,72] For comparison, 1 M lithium bis(trifluoromethanesulfonyl)amide (LiTFSA) in propylene carbonate (PC, Kishida Chemical Co., Ltd.) was also used as a conventional organic electrolyte. The electrolyte preparation and cell assembly were performed in an argon-filled glove box (DBO-2.5LNKP-TS, Miwa MFG) which was maintained at a dew point below -100 ^{o}C and an oxygen content below 1 ppm. A galvanostatic charge–discharge test was conducted using an electrochemical measurement system (HJ-1001SD8, Hokuto Denko Co., Ltd.) in a potential range between 0.005 and 2.000 V vs. Li$^+$/Li at 30 ^{o}C under a current density of 0.42 A g^{-1} (0.12 *C*) unless otherwise stated. The rate capability was also investigated at a current rate from 0.12 to 12 *C*.

Morphological observation and elemental analysis

After the charge−discharge test, the coin-type cell was disassembled in an argon-filled glove box to prevent exposure to the atmosphere, and the electrode was washed with PC and diethyl carbonate (DEC, Kishida Chemical Co., Ltd.) to remove residual electrolytes. A focused ion beam (FIB, JIB-4501, JEOL Co., Ltd.) was used to fabricate the cross-sectional surface of the electrode. The surface of the electrode was coated with carbon to protect it against damage by the Ga^+ beam of FIB. The cross-sectional surface of the electrode was observed by a field-emission scanning electron microscope (FE-SEM, JSM-7800F, JEOL Co., Ltd.) equipped with energy dispersive X-ray spectroscopy (EDS) and soft X-ray emission spectroscopy (SXES). The electrodes were not exposed to the atmosphere until they were introduced into the chamber of the FE-SEM from cell disassembly using a transfer vessel.

Raman spectroscopic analysis

The distribution of *c*-Si and *a*-Si on the electrode surface after the charge–discharge test was investigated by Raman microscopy (NanofinderFLEX, Tokyo Instruments, Inc.). Raman spectra were excited with the 532 nm line (16.5 mW) of a Nd:YAG laser through a 50-power objective lens. After the 10th cycle, the coin-type cell was disassembled in a glove box and the Si electrode was washed with PC and DEC to remove residual electrolyte. The electrode was then put into a sealed cell. The mapping area was 7×7 μm^2, and Raman spectra of 400 points (20- by-20 points) were recorded. Raman images of the electrode surfaces were then made by plotting the band position with the maximum intensity in a wavenumber range from 490 to 520 cm^{-1}.

3.3 Results and Discussion

Figure 3-1a and b show the charge–discharge curves of the Si electrodes at 1st to 100th cycles in PC-based organic and FSA-based ionic liquid electrolytes. At the 1st cycle, potential plateaus were observed at around 0.1 and 0.4 V vs. Li$^+$/Li on charge and discharge curves in each electrolyte. These potential plateaus are attributed to the alloying and dealloying reactions of Si with Li. In addition, potential slopes were also observed more than 0.2 V vs. Li$^+$/Li on charge curves in each electrolyte, indicating that the electrolyte was decomposed to form a film on the electrode surface.[79,80] The Coulombic efficiencies at the 1st cycle were 81% and 76% in PC and PP1MEM-FSA, respectively. These low efficiencies should be attributed to the electrolyte decomposition. However, the ideal film prevents continuous decomposition of electrolyte during subsequent cycles. Therefore, potential slopes were not clearly appeared on charge curves following 2nd cycle.

Figure 3-1c shows the cycling performance of a Si electrode in PP1MEM-FSA or PC. The Si electrode exhibited a high discharge capacity of 2700 mA h g^{-1} at the first cycle in the PC. However, almost all of the capacity faded by the 100th cycle. In contrast, in the PP1MEM-FSA, the electrode showed not only a high initial discharge capacity of 2700 mA h g^{-1} but also excellent cycling stability: the discharge capacity was approximately 950 mA h g^{-1} even at the 500th cycle. We previously reported that a Si electrode exhibited a discharge capacity of 1000 mA h g^{-1} at the 100th cycle in 1 M LiTFSA/PP1MEM-TFSA.[38,71] Although these ionic liquids consisted of the same PP1MEM cation, the PP1MEM-FSA achieved superior cycling performance. Therefore, the author focused on the FSA-based electrolyte in this study. The areal capacity is important factor in this field. The capacity was calculated and shown in Figure 3-2. An areal capacity of 0.15 mA h cm^{-2} in PP1MEM-FSA was never high. However, a GD method is a suitable technique for forming thick films and does not require

any conductive additive and binder for the preparation of thick-film electrodes. It is thus possible to directly observe an electrochemical reaction between pure Si and electrolytes.

Figure 3-1d shows an enlarged view of the initial Coulombic efficiency in Figure 1c. A drop in efficiency was observed at around the 30th cycle in the PC. Because a large change in the volume of Si during the charge–discharge process led to cracking and pulverization of the active material layer, the PC was decomposed on the newly exposed electrode surface. This is the reason for the drop in efficiency. In contrast, in the PP1MEM-FSA, the efficiency gradually increased with cycle number and remained above 95% after the 30th cycle, indicating that the extent of disintegration of the electrode in the PP1MEM-FSA was small compared to that in the PC.
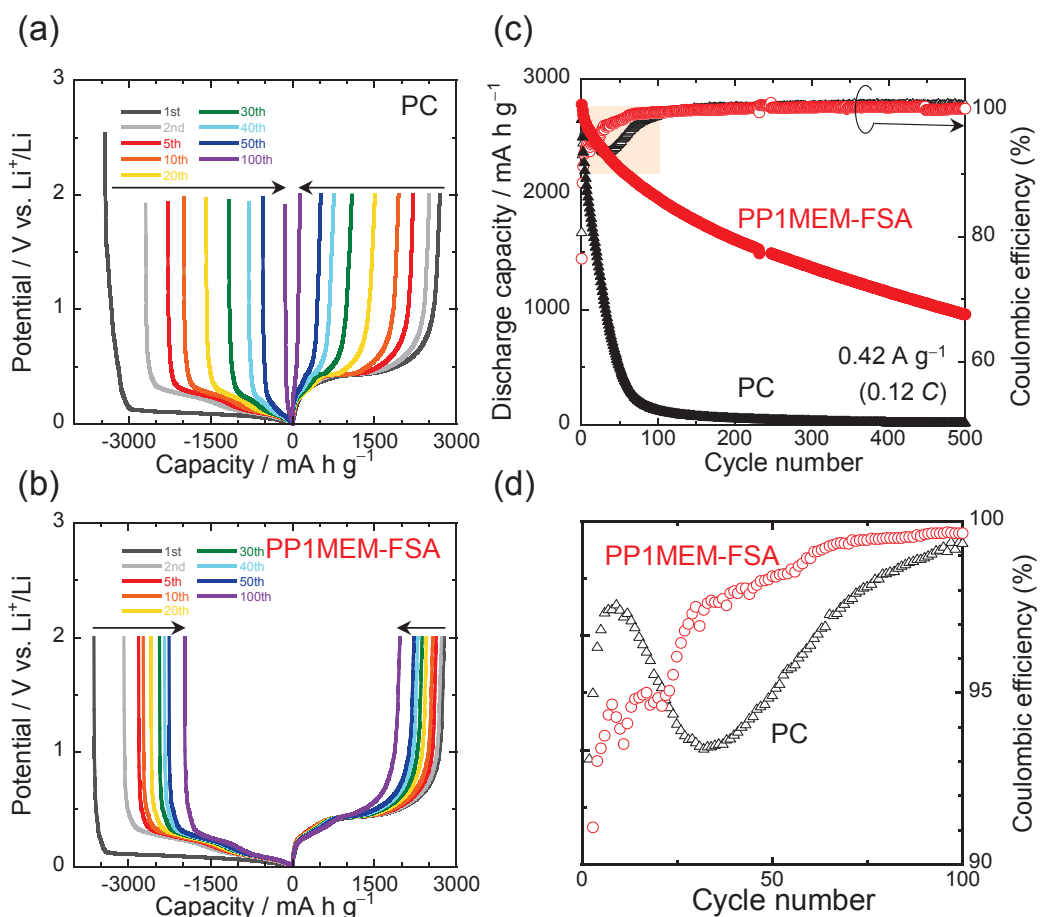

Figure 3-1. Charge–discharge curves of Si electrodes in (a) 1 M LiTFSA/PC and (b) LiFSA/PP1MEM-FSA. (c) Cycling performance of Si electrode in 1 M LiFSA/PP1MEM-FSA or LiTFSA/PC. (d) Enlarged view of the corresponding Coulombic efficiency during the initial 100 cycles.
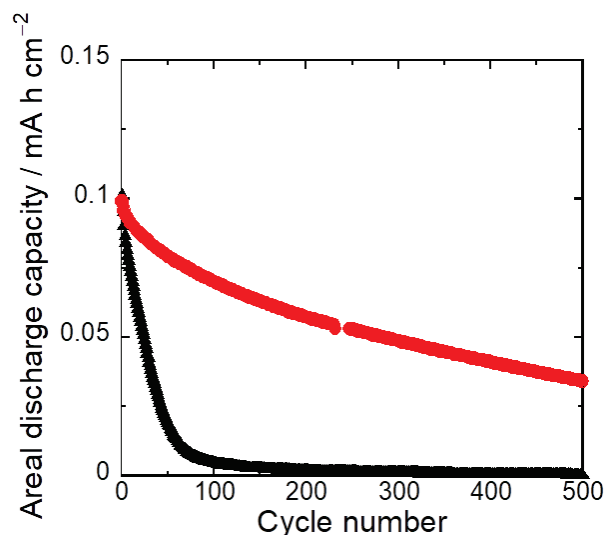
Figure 3-2. Dependence of areal discharge capacities of Si electrodes on cycle number in 1 M LiTFSA/PC and LiFSA/PP1MEM-FSA.

To elucidate the reaction behaviors of Si electrodes in each electrolyte, the author observed changes in the morphology of the Si active material layer after the charge–discharge test by cross-sectional SEM, as shown in Figure 3-3. While the thickness of the Si active material layer was 1.6 μm before cycling, it increased to 2.4 and 3.6 μm after the first cycle in the PP1MEM-FSA and PC, respectively. In addition, the thickness was estimated to be 10.4 and 14.9 μm after the 20th cycle in the PP1MEM-FSA and PC, respectively. Table 3-1 shows the variation in the thickness of the Si layer versus the number of cycles. The thickness of the Si layer increased with the cycle number in both electrolytes. In addition, the Si layer in the PP1MEM-FSA was thinner than that in the PC. The Si layer in the PC became porous after the 20th cycle, whereas that in the PP1MEM-FSA was not very porous. A similar phenomenon has been reported for other Si-based electrodes in PC.[81] Therefore, this phenomenon can be attributed to the electrolyte rather than the electrode. PC-based organic electrolytes are generally decomposed to inhomogeneously form surface film on anodes.[82] It is considered that Li^+ is preferentially inserted into the electrode through not the thicker parts but the thinner parts of the surface film, because the thicker parts inhibit the Li-insertion reactions. For non-uniform Li-insertion, extreme volume expansion and contraction occur in

39

the localized regions of the Si electrode, which intensively generates accumulated stress in these regions. This leads to severe disintegration of the Si electrode, which then results in poor cycling stability. In addition, the extreme volume changes bring about the formation of cracks. After Li-extraction from the Si electrode, the crack becomes larger, and a partial breakup of the electrode occurs. The author considers this is the reason that the Si layer was porous in PC. On the other hand, a film derived from ionic liquid electrolyte is thin and stable.[74] In addition, the author revealed that Li-insertion uniformly occurs in PP1MEM-TFSA.[57] The uniform Li-insertion into the Si electrode makes the Si layer expand uniformly. As a result, the stress uniformly generates over the entire surface. In other words, the Si electrode can reasonably avoid stress accumulation in localized regions, which suppresses the severe disintegration of the Si electrode. For this reason, the Si layer in PP1MEM-FSA was not as porous as that in PC.
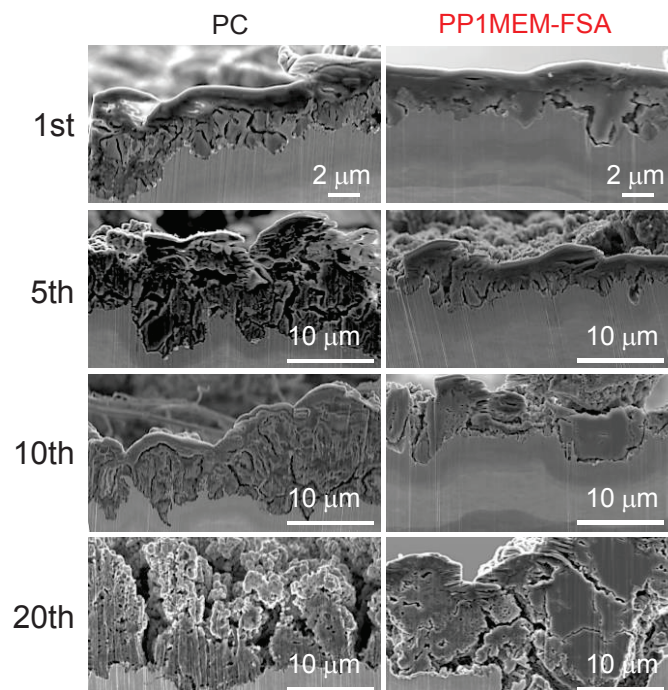

Figure 3-3. Cross-sectional SEM images of lithiated Si electrodes after the 1st, 5th, 10th and 20th cycle in 1 M (left) LiTFSA/PC or (right) LiFSA/PP1MEM-FSA.

Table 3-1. Thickness of a lithiated Si layer after the 1st, 5th, 10th, and 20th cycles estimated from Figure 3-3.

	PC	PP1MEM-FSA
Before cycle	1.6 $\pm$ 0.3 μm	
1st cycle	3.6 $\pm$ 0.9 μm	2.4 $\pm$ 0.7 μm
5th cycle	8.6 $\pm$ 2.7 μm	3.0 $\pm$ 0.9 μm
10th cycle	8.8 $\pm$ 2.8 μm	5.6 $\pm$ 1.2 μm
20th cycle	14.9 $\pm$ 2.7 μm	10.4 $\pm$ 4.5 μm

It is well known that the properties of films strongly affect battery performance.[70] To investigate the composition of the film, an elemental analysis was performed for a cross-section of the electrode. Figure 3-4 shows the results of EDS elemental mapping after the 10th cycle in combination with SEM images. C and O were detected in the Si layer in the PC. This suggests that the electrolyte penetrated into the Si layer which became porous, and was reductively decomposed. It has been reported that the decomposition products of carbonate-based solvents are mainly lithium carbonate, lithium alkyl carbonate, and organic salts.[55,70,83,84] Among these, organic salts are soluble in electrolytes, which mean that a surface film composed of organic salts should be unstable during charge–discharge cycling. Although LiTFSA (LiN(SO$_2$CF$_3$)$_2$) contains fluorine, almost no F was detected, indicating that the organic solvent, i.e. PC, was mainly decomposed during a charge–discharge process. On the other hand, in the PP1MEM-FSA, the author observed not only C and O, but also F. Indeed, F was confirmed after each cycle, as shown in Figures 3-5a-c. Table 3-2 shows the ratios of all elements calculated from EDS spectra. In contrast to the PC, the FSA anion appeared to have decomposed, since S and N were detected in the PP1MEM-FSA. Some researchers have reported that the decomposition products of FSA are LiF, Li$_2$O, and so on.[55,69] LiF and Li$_2$O have been shown to enhance the structural stability of a film on an electrode surface and the anode property of a Si electrode was remarkably improved by a

41

surface film including LiF and Li_2O.[55,66] Therefore, the formation of a favorable film on the surface and the interior of the Si electrode should contribute to the excellent cycling stability.
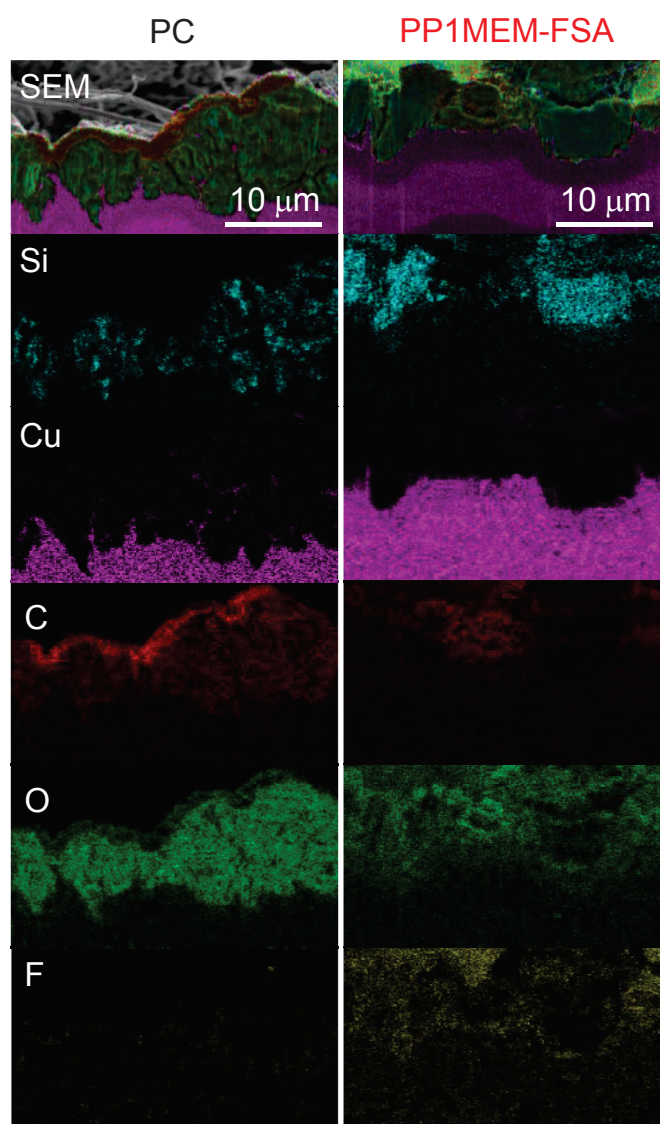

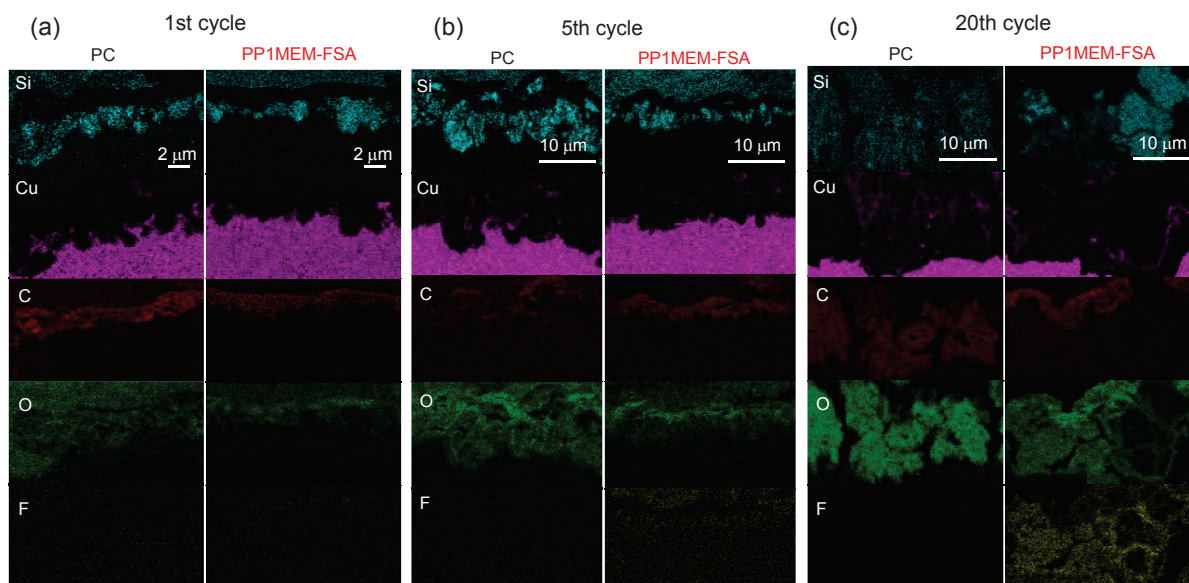Figure 3-4. Cross-sectional EDS mapping images of Si electrodes after the 10th charge.

Figure 3-5. Cross-sectional EDS mapping images of Si electrodes after the (a) 1st, (b) 5th, and (c) 20th charge.

Table 3-2. Elemental ratio (atomic %) on the cross-section of a Si active material layer calculated from an EDS spectrum after the 1st, 5th, 10th, and 20th cycles.

	PC					PP1MEM-FSA				
	C	N	O	F	S	C	N	O	F	S
1st cycle	49.2	0.6	45.9	3.5	0.8	47.0	2.4	35.8	10.5	4.3
5th cycle	40.0	0	56.2	3.1	0.7	50.0	2.3	33.1	11.0	3.6
10th cycle	41.7	0.4	53.1	4.0	0.8	31.6	4.2	34.0	22.8	7.4
20th cycle	35.6	0.2	59.1	3.7	1.4	31.7	2.0	52.2	9.2	4.9

It is very important to understand the distribution of the lithiation–delithiation reaction of Si electrodes, because this distribution leads to the utilization ratio of active material and largely affects the cycling performance of Si electrodes.[56] To investigate the distribution of c-Si and a-Si on the surface of the Si electrode, Raman mapping measurement was conducted. Mapping was performed at peak positions with maximal intensities within a wavenumber range from 490 to 520 cm^{-1} based on the phenomenon that the crystallinity of Si decreases upon reaction with Li. Figures 3-6a and b show Raman mappings of delithiated Si electrodes

after the 10th cycle in the PC and PP1MEM-FSA, respectively. The red region in the images corresponds to *c*-Si, which did not react with Li, whereas the blue region indicates *a*-Si, which completely reacted. In regions with a cooler color (*e.g.* green), Si showed a greater loss of crystallinity. In Figure 3-6a, *c*-Si locally remained on the electrode, which means that the lithiation–delithiation reaction inhomogeneously occurred in the PC. In contrast, the domains of *a*-Si were homogeneously distributed on the electrode surface in the PP1MEM-FSA (Figure 3-6b), which shows that the lithiation–delithiation reaction occurred uniformly. As mentioned above, this is probably because FSA-derived films are thin and have uniform conductivity of Li; thus, Li was inserted into the Si electrode over the entire surface, which suppresses severe disintegration of the Si electrode. The uniform distribution of lithiation–delithiation enhances the utilization ratio of active material and contributes to the significant improvement in the cycling performance of the Si electrode with the use of a PP1MEM-FSA.
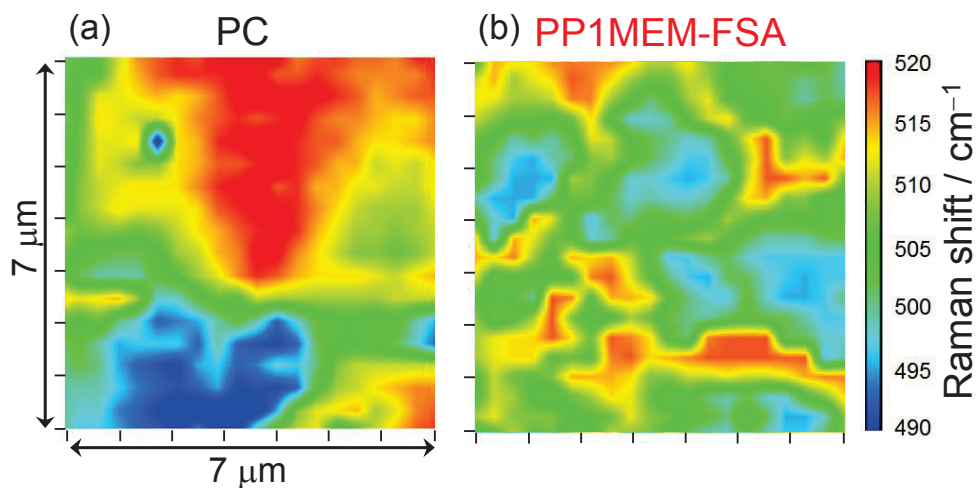

Figure 3-6. Raman mapping images of the delithiated Si electrode surface after the 10th cycle. The electrodes were cycled in (a) LiTFSA/PC or (b) LiFSA/PP1MEM-FSA.

To show that the results of Raman mapping are applicable over a wider regions, the author conducted Raman spectroscopic measurements quantitatively at arbitrary points in a 100 μm square on the electrode surface. Figure 3-7 shows the dependence of the mean value

of the Raman shift and its standard deviation (SD) for the Si electrode on the cycle number in each electrolyte. In the PC, the SD was large during 10 cycles, indicating that the region where Si reacted with Li and the region where it did not react were mixed over a wide area on the electrode. On the other hand, in the PP1MEM-FSA, lithiation–delithiation reactions should uniformly occur within a region of $100 \times 100\ \mu m^2$, because the SD was smaller during 10 cycles. Consequently, these results reflect the findings of Raman mapping analyses. The mean value in the PP1MEM-FSA was lower than that in the PC at each cycle. In addition, almost no change in the mean value was observed in the PP1MEM-FSA, whereas the value decreased gradually with cycle number in the PC. These results indicate that the crystallinity of Si on the electrode decreased continuously in the organic electrolyte. In contrast, almost no change in crystallinity was confirmed during the 10th cycle in the PP1MEM-FSA. In the PP1MEM-FSA, a favorable film was formed on the entire surface of the electrode at the initial cycle, and the charge–discharge reaction was repeated. In contrast, a favorable film was not formed in the PC, and the lithiation–delithiation reaction occurred locally and gradually decreased the crystallinity of Si.
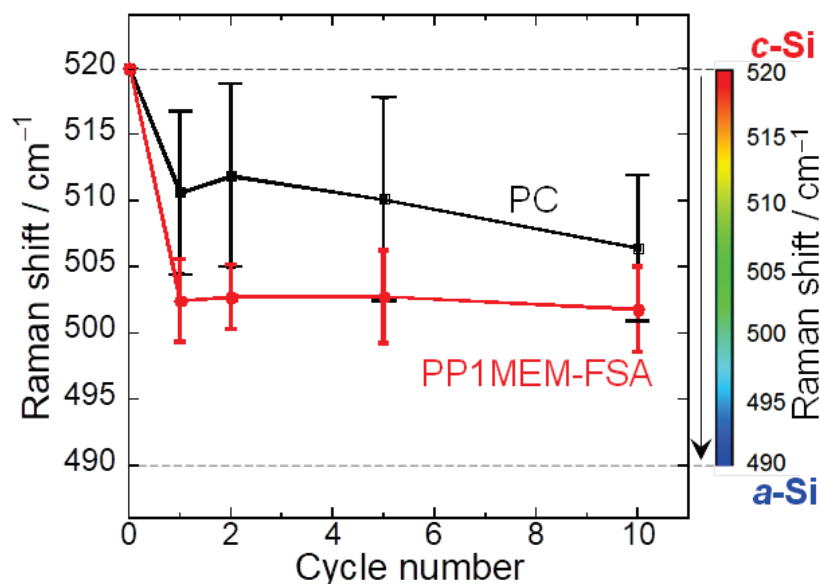

Figure 3-7. Dependence of mean value and standard deviation of Raman shift on cycle number for Si electrodes cycled in 1 M LiTFSA/PC or LiFSA/PP1MEM-FSA.

45

To determine distribution of the lithiation–delithiation reaction inside Si electrode, SXES measurements of the electrodes were performed after the 10th cycle, as shown in Figure 3-8. The intersection of crosses in the SEM images indicates measured points, and the number corresponds to each SXE spectrum. Figure 3-9 shows the enlarged view of SXE spectra in Figure 3-8. It is reported that peaks of Li_2O and LiF newly appear at both side of the peak of 0.054 keV corresponding to Li.[84] Thus, the author considered that Li-K emission detected at 0.054 keV shows not Li_2O or LiF but Li in Si. In the PC, no Li-K emission was confirmed at the measured points in 3 and 4, whereas it was detected in 1 and 2. This result revealed that a lithiation reaction inhomogeneously occurred in the PC. In addition, oxygen and carbon were clearly observed at all of the measured points, consistent with the results of EDS mapping, which supports the notion that a film derived from the PC was also formed inside the Si active material layer. On the other hand, Li was detected at all the measured points in the PP1MEM-FSA. This result appears to indicate that the Si electrode uniformly reacted with Li in the PP1MEM-FSA. Since the Si active material layer uniformly expanded and contracted, stresses arising from a change in the volume of Si did not accumulate locally in the layer. Thus, disintegration of the layer was suppressed, which should contribute to the excellent cycling stability. In addition, the FSA-derived film should be thin and uniform, because Si-L emission was observed and the peak intensity of oxygen and carbon were low at all points. On the other hand, Si-L emission was not detected on the electrode cycled in the PC, indicating that the film derived from a PC was thicker than that derived from FSA.
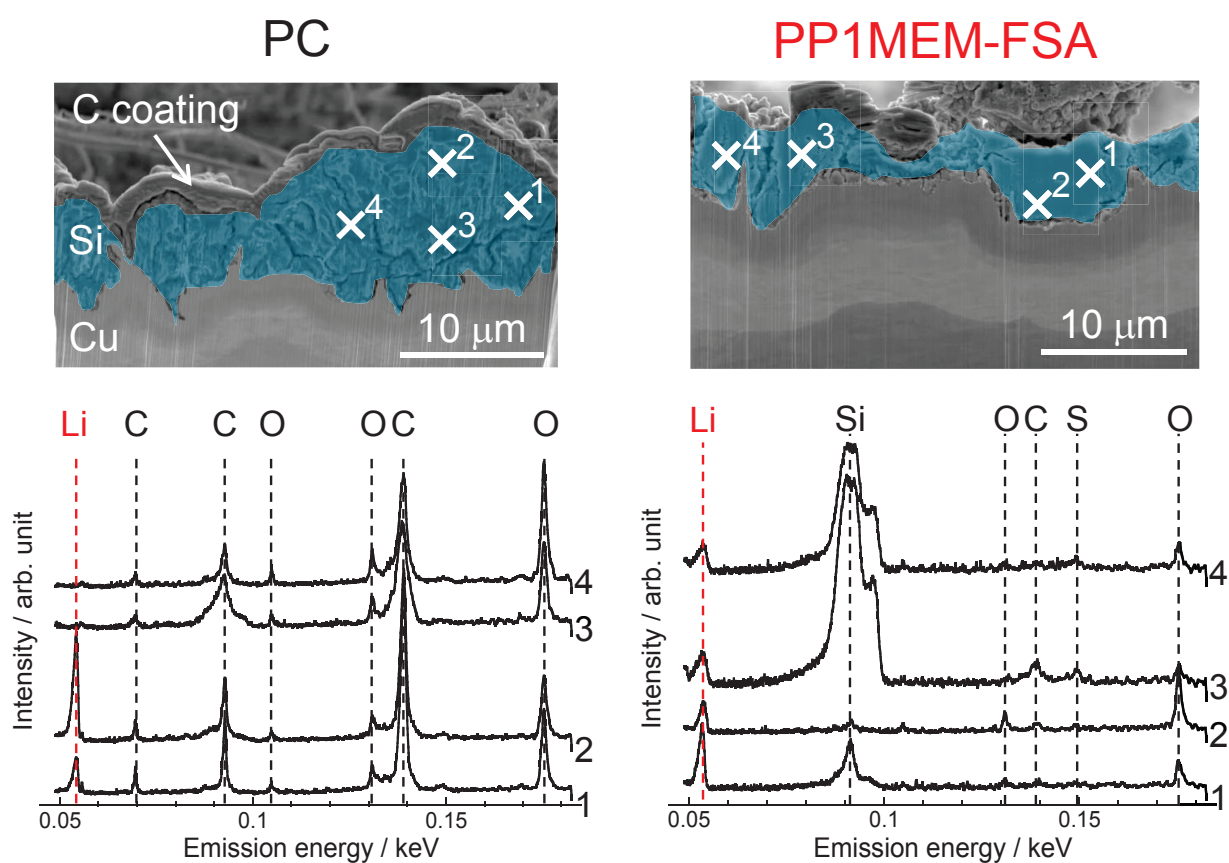
Figure 3-8. (top) Cross-sectional SEM images and (bottom) SXE spectra of Si electrodes at a charged state after the 10th cycle. The electrodes were cycled in 1 M LiTFSA/PC or LiFSA/PP1MEM-FSA.
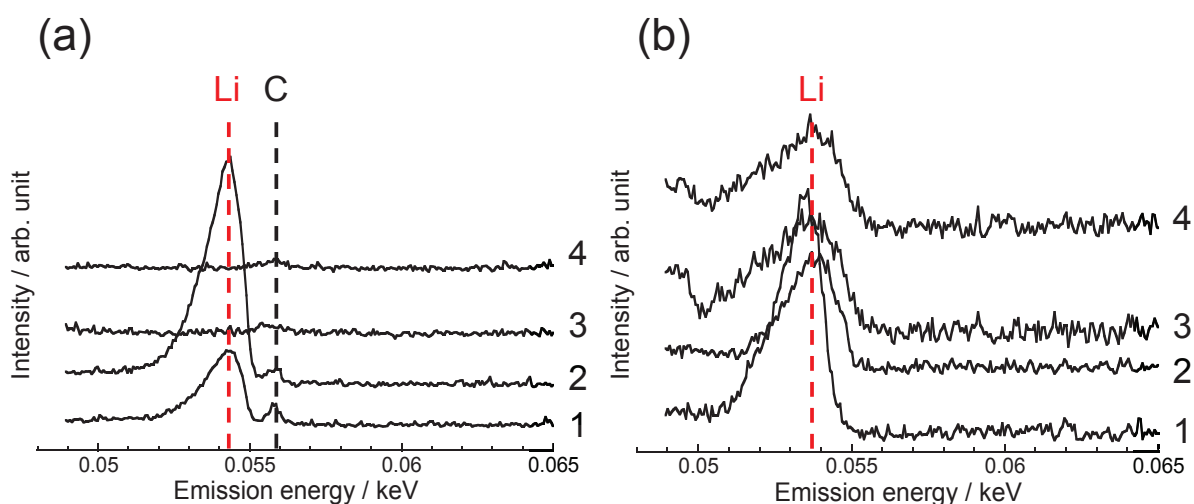

Figure 3-9. Enlarged view of SXE spectra in Figure 3-8. The electrodes were cycled in (a) 1 M LiTFSA/PC or (b) LiFSA/PP1MEM-FSA.

Si exhibits an extremely high capacity by alloying with Li to form $Li_{15}Si_4$. In this process, its volume expands up to approximately 4 times, which leads to disintegration of the electrodes. Even if a favorable electrode–electrolyte interface, which enables uniform Li-insertion into the Si electrode, is formed, the excessive volume expansion leads to breakup of the interface. The author has demonstrated that a favorable electrode–electrolyte interface can be maintained by controlling the amount of Li insertion–extraction, as shown in chapters 1 and 2. Figure 3-10 shows the long cycling performance of a Si electrode in the PP1MEM-FSA with a discharge-capacity limitation of 1000 mA h g^{-1}. In the PC, the Si electrode maintained a discharge capacity of 1000 mA h g^{-1} until 200 cycles. On the other hand, the cycling performance dramatically improved in the PP1MEM-FSA. The Si electrode exhibited extremely excellent cycling stability and maintained a high capacity of 1000 mA h g^{-1} beyond 3000 cycles. The electrode without capacity limitation was not able to maintain a discharge capacity of 1000 mA h g^{-1} beyond the 500th cycle, as shown in Figure 3-1c. Therefore, this excellent performance should be attributed to the notion that a favorable electrode–electrolyte interface was achieved by suppressing extreme volumetric changes in the Si layer.
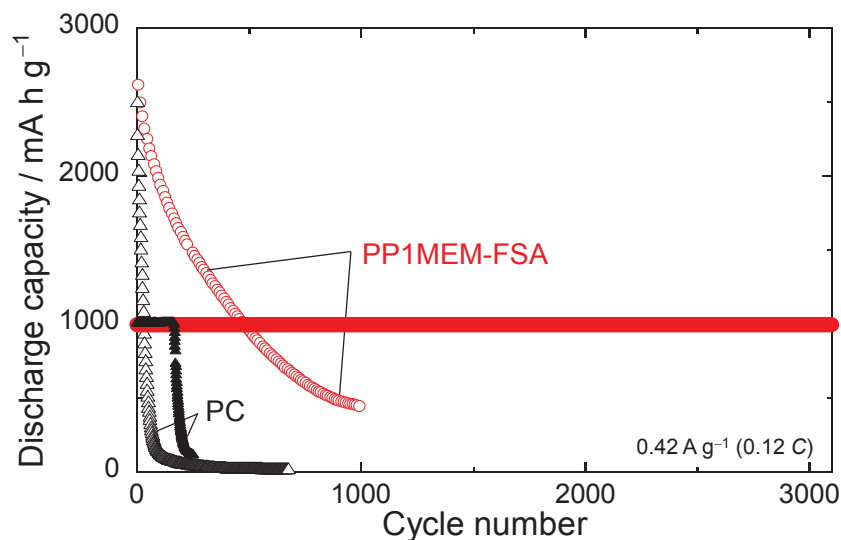

Figure 3-10. Changes in discharge capacities of Si electrodes versus cycles number in 1 M LiFSA/PP1MEM-FSA, or LiTFSA/PC. The discharge capacities were limited to 1000 mA h g^{-1}. For comparison, the performances of electrodes without capacity limitation are also plotted.

Figure 3-11a shows the rate capabilities of the Si electrodes in the PP1MEM-FSA and PC with a discharge capacity limitation of 1000 mA h g^{-1}. The electrode in the PP1MEM-FSA maintained a discharge capacity of 1000 mA h g^{-1} even at a relatively high current density of 8.4 A g^{-1} (2.4 C), but the capacity decreased at a current rate of 6 or 12 C. On the other hand, in the PC, the electrode maintained this discharge capacity even at a higher current rate of 12 C. The author previously confirmed that the ionic conductivities of the PP1MEM-FSA and PC are 2.06 and 5.51 mS cm^{-1} at 303 K, respectively (see chapter 1). Under a high current rate, Li$^+$ transport, i.e., ionic conductivity in the electrolyte bulk, dominantly affects the rate capability. Therefore, the capacity-fading in the PP1MEM-FSA at 6 and 12 C may be mainly caused by limitation of the rate of Li$^+$ diffusion in the electrolyte bulk. As shown in Figure 3-11b, when the charge capacity was limited, the discharge capacity of the electrode in the PC decreased at 12 C. This result suggests that the electrode was more disintegrated compared to when the discharge capacity was limited.
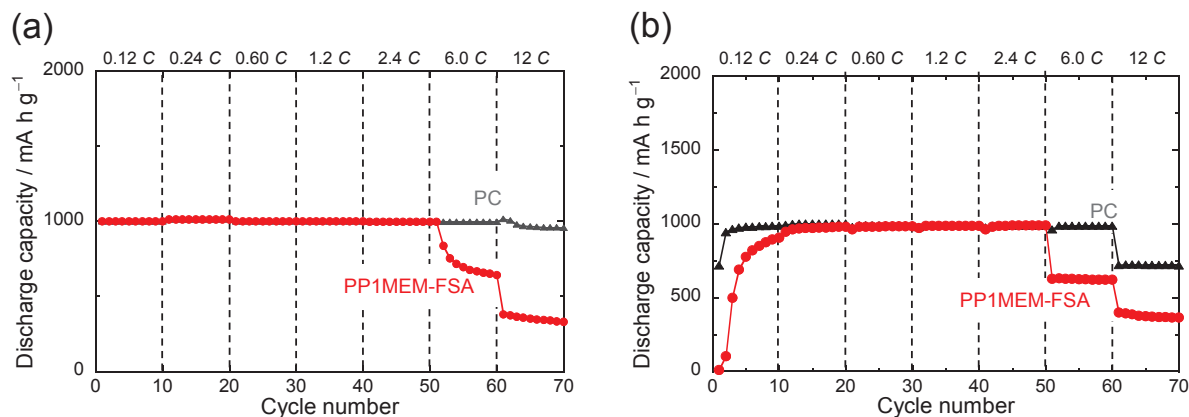

Figure 3-11. Rate capabilities of Si electrodes in 1 M LiFSA/PP1MEM-FSA, or LiTFSA/PC at various current densities from 0.42 to 42 A g^{-1}. (a) The discharge and (b) charge capacities were limited to 1000 mA h g^{-1}.

3.4 Summary

A Si-alone electrode exhibited superior electrochemical performance in an FSA-based ionic liquid electrolyte compared to a PC-based organic electrolyte. The electrode in the PP1MEM-FSA maintained a discharge capacity of 1000 mA h g^{-1} beyond 3000 cycles, whereas that in the PC retained this capacity until only 200 cycles. To understand the reason for the excellent cycling performance, the author tried to elucidate the reaction behavior of the Si electrode in the PP1MEM-FSA. The author confirmed that the thickness of the electrode increased with cycle number in both electrolytes by cross-sectional SEM observations. This means also that the PP1MEM-FSA is not able to stop the continuous growth of the Si layer but that the FSA-derived film has enough structural stability for long term cycling and this is probably due to the presence of LiF in its composition. The EDS mapping results demonstrated that a film derived from electrolytes was formed not only on the surface, but also inside of the electrode. In addition, the FSA-derived film contained F and O, which suggests that LiF and Li_2O were formed. Thus, the film should be more stable and contribute to better cycling performance. The SXES results suggested that the lithiation distribution on the cross-section of the Si layer in the PP1MEM-FSA was more uniform than that in the PC. In addition, the film derived from FSA was thin and uniform. Raman spectroscopic analysis revealed that a lithiation reaction proceeded uniformly, which helped to suppress the disintegration of the Si active material layer. Consequently, the Si-alone electrode in the PP1MEM-FSA attained excellent cycling stability.

Chapter 4

Effect of Film-Forming Additive in Ionic Liquid Electrolyte on the Charge–Discharge Performance of Si Anode for LIBs

4.1 Introduction

In chapter 1 to 3, the author demonstrated that fabrication of electrode–electrolyte interface by using the FSA-based ionic liquid electrolyte was effective to enhance the electrochemical performance of Si-based anode for LIBs. Meanwhile, the high viscosity of quaternary ammonium-based ionic liquid electrolytes, such as piperidinium and pyrrolidinium-based, hinders charge transfer reaction at electrode–electrolyte interface, leading to deteriorating cycle life and rate performance of Si electrode. In contrast, imidazolium-based ionic liquids have lower viscosity and higher conductivity than quaternary ammonium-based ionic liquids.[19,37,58,85] For example, viscosity and conductivity of 1-ethyl-3-methylimidazolium bis(trifluoromethanesulfonyl)amide (EMI-TFSA) is 33 mPa s and 8.3 mS cm^{-1} at 298 K, whereas those of 1-methyl-1-propylpyrrolidinium bis(trifluoromethanesulfonyl)amide (Py13-TFSA) is 61 mPa s and 3.9 mS cm^{-1} at 298 K, respectively.[19] Hence, the EMI-based ionic liquids may enhance the battery performance. Nevertheless, EMI cation is easily decomposed reductively and the decomposition product inhibits Li$^+$ insertion into the electrode.[37,46,75] This is one of the reasons for hindrance of application of EMI-based ionic liquids to electrolytes for LIBs.

It is well known that film-forming additives, such as vinylene carbonate (VC) and fluoroethylene carbonate (FEC), can suppress continual electrolyte decomposition because they preferentially decompose to form stable surface film on the electrode.[56,70,86–89] Sun *et al*. reported that reversible charge–discharge reaction of graphite electrode proceeded in pyrrolidinium and piperidinium-based ionic liquid electrolytes by addition of VC.[90] Ishikawa

51

et al. applied 0.8 mol dm^{-3} (M) LiTFSA/1-ethyl-3-methylimidazolium bis(fluorosulfonyl)amide (EMI-FSA) with 10 wt.% propylene carbonate (PC) and VC to graphite electrode, and confirmed that Li^{+} insertion/extraction reaction occurred in the presence of VC.[91] If a favorable film derived from additives is also formed on the Si electrode surface in the EMI-based ionic liquid electrolytes, reductive decomposition of EMI cation will be suppressed to achieve a high rate capability. On the other hand, FSA anion enables a reversible charge–discharge reaction of graphite or Si electrode in EMI-based ionic liquid electrolyte without organic additives. Ishikawa *et al*. reported that a discharge capacity of Si–Ni–carbon composite electrode was 932.5 mA h g^{-1} even at the 20th cycle in 0.3 mol kg^{-1} LiTFSA/EMI-FSA, whereas no capacity was obtained in LiTFSA/EMI-TFSA.[75] They considered that such excellent performance with FSA-based electrolyte correlates with very low interfacial and charge-transfer resistances at the Si-based composite anode. Piper *et al.* applied 1.2 M LiFSA/EMI-FSA to cyclized-polyacrylonitrile-based Si nanocomposite architecture (nSi-cPAN), and demonstrated that the nSi-cPAN electrode maintained a discharge capacity of more than 2000 mA h g^{-1} after 100 cycles.[17] However, influence of EMI-FSA on the cycling performance of Si-alone electrode is not sufficiently understood because these electrodes were fabricated by mixing active materials with binders and conductive additives. They causes side reaction, which makes difficult to observe reaction of Si itself.

We have applied a gas-deposition method to prepare electrode, which requires no binders and conductive additives.[48] Thus, this method is suitable for analyzing the reaction behavior at interface between active materials and electrolytes. In this study, the author investigated an effect of VC-addition to EMI-based ionic liquid electrolytes on a cycling performance of Si-alone anode for LIBs. The author also studied relationship between cation/anion structure in ionic liquid electrolyte and electrochemical performance of Si

electrode. Coordination environment of Li$^+$ in each electrolyte was explored by Raman spectroscopic measurements. To confirm non-flammability of VC-added ionic liquid electrolyte, fire-resistance test was also conducted.

4.2 Experimental Details

The author used two types of commercially available ionic liquids: the one is EMI-TFSA (Kanto Chemical Co., Ltd.) and the other is EMI-FSA (Kanto Chemical Co., Ltd.). Chemical structures of these ionic liquids were shown in Figure 4-1. The electrolytes were 1 M LiTFSA (99.9%, Kishida Chemical Co., Ltd.) dissolved in EMI-TFSA and 1 M lithium bis(fluorosulfonyl)amide (LiFSA; 99%, Kishida Chemical Co., Ltd.) dissolved in EMI-FSA. The anion of the Li salt was the same as that of the ionic liquid: only single anion species was in the electrolytes. Then, 5 or 20 vol.% of VC (Kishida Chemical Co., Ltd.) was added to each electrolyte. The ionic conductivity was investigated by an electrochemical impedance spectroscopy (EIS) with CompactStat of Ivium Technologies using the cell with two Pt electrodes under argon atmosphere at various temperatures from 298 to 333 K. To confirm the superiority of EMI-based electrolyte, the author also adopted an electrolyte consisted of Py13-TFSA; Kanto Chemical Co., Ltd.) which has high stability against oxidation/reduction.
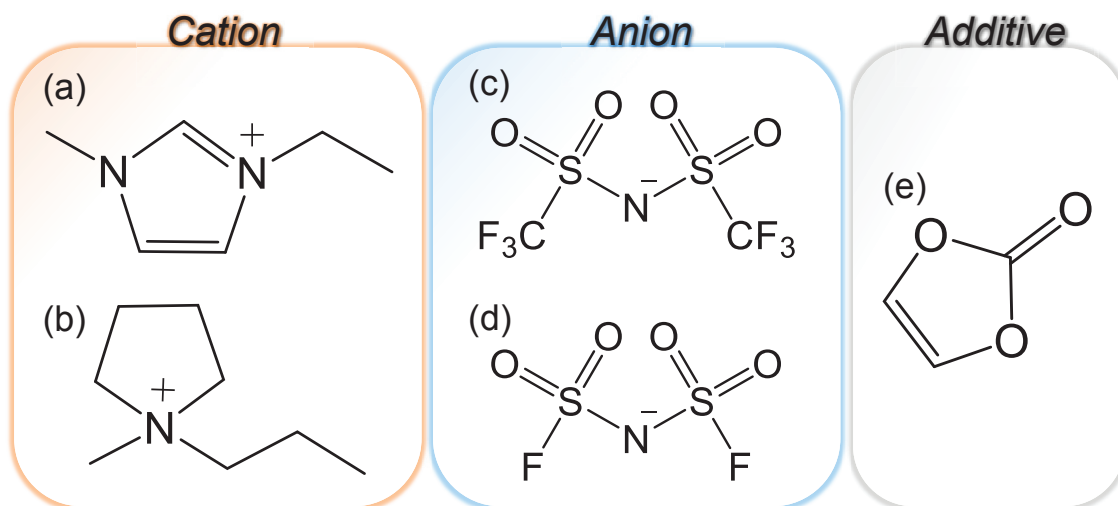
Figure 4-1. Chemical structure of (a) 1-ethyl-3-methylimidazolium (EMI$^+$), (b) 1-methyl-1-propylpyrrolidinium (Py13$^+$), (c) bis(trifluoromethanesulfonyl)amide (TFSA$^-$), (d) bis(fluorosulfonyl)amide (FSA$^-$), and (e) vinylene carbonate (VC).

The interactions between Li$^+$ and VC or FSA anion of ionic liquid electrolytes were analyzed by using a Raman microscopy system (NanofinderFLEX, Tokyo Instruments, Inc.) with 532 nm line of Nd:YAG laser through a 50-power objective lens at room temperature. Although the electrolytes used in this study were consisted of mainly ionic liquids, VC, that is organic film-forming additive was also contained; hence, advantage of non-flammability might be lost. Thus, the author conducted fire-resistance tests by using a flash point tester (Setaflash Series: 33000-0, STANHOPE SETA LTD.). These tests were performed in line with rapid equilibrium closed cup method according to International Organization for Standardization (ISO) 3679:2004 and Japanese Industrial Standards (JIS) K2265-2. We have introduced this technique as the evaluation method for the flame retardancy of ionic liquid electrolytes for the first time.[92,93] Detail condition and procedure have been described in previous our report.[92]

Cell assembly and electrochemical measurements

Si electrodes were prepared by a gas-deposition method using commercially available Si powder (FUJIFILM Wako Pure Chemical Corporation, 99.9%, average particle size: 20 μm). The detail condition is listed in the previous papers.[38,57] The deposited weight of active material on the Cu substrate was measured to an accuracy of 1 μg with an XP6 ultramicrobalance (Mettler-Toledo) equipped with an anti-vibration table. Si electrodes in the range of 28−32 μg were adopted. We confirmed that the GD-electrode was composed only of Si by XRD pattern (Figure 4-2a) and that Si was crystalline by Raman spectrum (Figure 4-2b). Figure 4-2c and d shows surface and cross-sectional field-emission scanning electron microscopic (FE-SEM) image of the electrode. The thickness and area of active material layer were approximately 1.6 μm and 0.8 cm^2, respectively. The author fabricated 2032-type coin cells, which contain Si electrode as working electrode, Li metal foil (Rare Metallic, 99.90%, thickness: 1.0 mm) as counter electrode, ionic liquid electrolyte, and glass-fiber filter as a separator. The author performed the charge–discharge test of the cells by using an electrochemical measurement system (HJ-1001 SM8 and HJ-1001 SD8, Hokuto Denko Co., Ltd) in the potential range between 0.005 and 2.000 V vs. Li^+/Li at 303 K under a current density of 420 mA g^{-1} (0.12 *C*). Rate capability was also evaluated under current density range from 1050 to 4200 mA g^{-1} (0.29–1.2 *C*). EIS analysis using a three-electrode type cell was performed at 0.005 V vs. Li^+/Li in the frequency range of 100 kHz to 10 mHz with an amplitude of 5 mV at 303 K. The surface morphology of the electrodes before and after cycling was observed by a field-emission scanning electron microscope (FE-SEM, JSM-6701F; JEOL Ltd.).
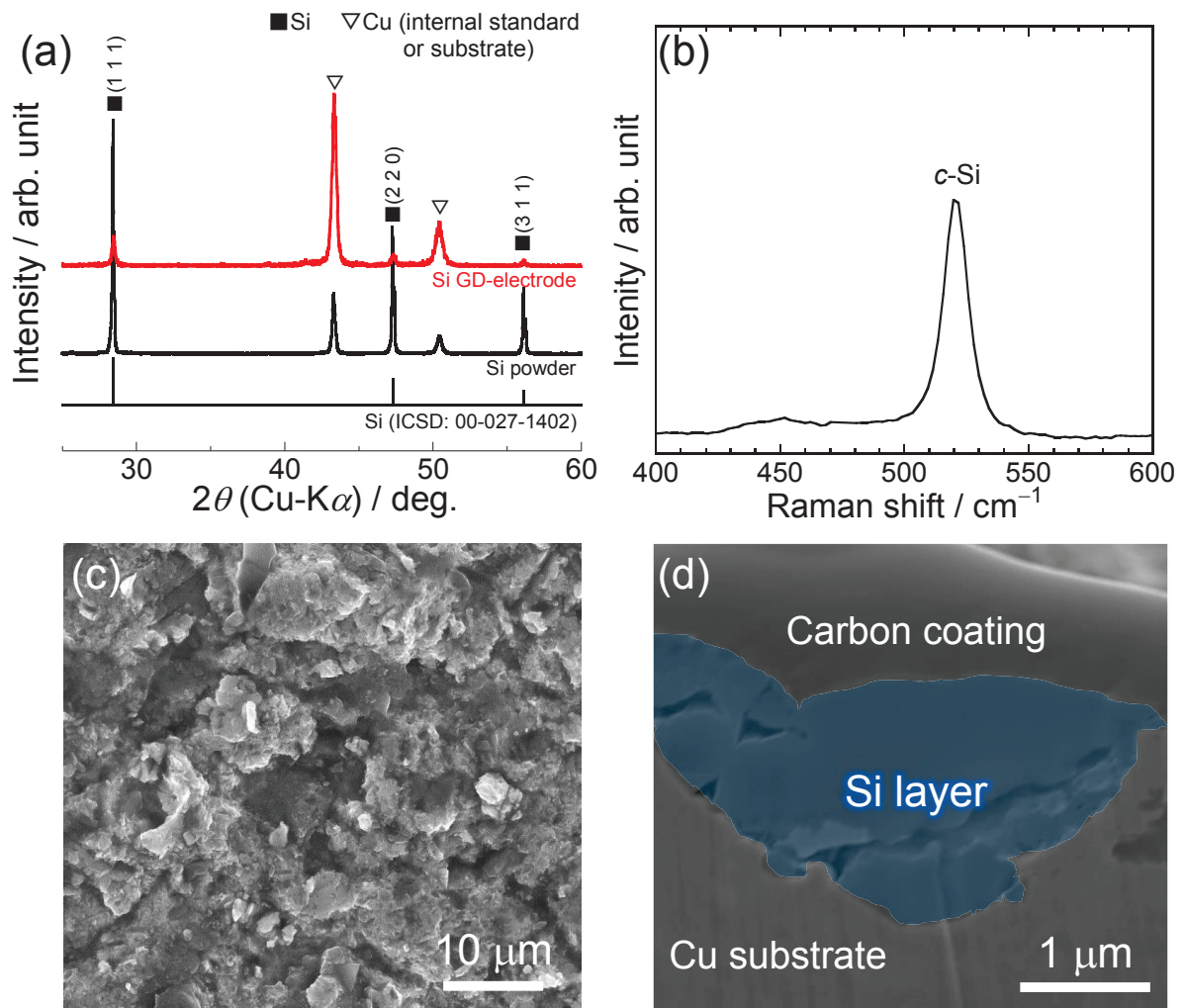
Figure 4-2. (a) XRD patterns and Si powder and Si GD-electrode as prepared. (b) Raman spectrum of Si GD-electrode. (c) Surface and (d) cross-sectional FE-SEM image of Si GD-electrode as prepared. The electrode surface was coated with carbon to protect it against damage by the Ga^+ beam of focused ion beam.

4.3 Results and Discussion

Electrochemical performance in an electrolyte consisted of EMI-TFSA

Figure 4-3a shows charge–discharge profiles of Si electrodes at the first cycle in an electrolyte of 1 M LiTFSA/EMI-TFSA without and with 5 or 20 vol.% VC. Figure 4-3b also shows corresponding differential charge capacity versus potential (dQ/dV) profiles. In all electrolytes, potential plateaus appeared at 0.1 and 0.4 V vs. Li^+/Li on charge and discharge

56

curves, respectively. These plateaus indicate that lithiation/delithiation reactions of Si proceeded with or without VC. However, a potential gradient (Figure 4-3a) and a broad peak (Figure 4-3b) was observed from 0.6 to 0.2 V vs. Li^+/Li in additive free electrolyte, which is attributed to reductive decomposition of EMI cation. Although a charge capacity was 5730 mA h g^{-1} in additive free electrolyte, a discharge capacity was only 2700 mA h g^{-1}, resulting in low Coulombic efficiency of 47%.   In contrast, no potential gradient and broad peak at 0.6 V vs. Li^+/Li was confirmed in the electrolyte with VC. In VC-added electrolytes, irreversible capacity reduced and therefore the Coulombic efficiency improved (VC 5 vol.%: 81% and 20 vol.%: 66%). From these results, it is found that reductive decomposition of EMI cation is suppressed in the presence of VC. Figure 4-3c shows cycling performances of Si electrode in 1 M LiTFSA/EMI-TFSA without and with VC. the electrolytes. The Si electrode exhibited a relatively high discharge capacity at initial cycles in additive free electrolyte, though most of its capacity was lost at only 10 cycles. This is because surface film derived from EMI cation was formed on Si electrode surface, which prohibits Li^+ insertion into Si active material layer.[37,75] On the other hand, a rapid capacity decay until initial 10 cycles was suppressed by adding VC 5 vol.%. Nevertheless, the capacity started to decrease after 50 cycles and almost no capacity was obtained after 100 cycles. To confirm the reason for capacity degradation after 50 cycles, the author observed the surface morphology of Si electrode after the 40th and 70th cycles by FE-SEM (Figure 4-4). Although the capacity quite decreased at the 70th cycle, the degree of electrode disintegration was comparable with the electrode at the 40th cycle before starting capacity decay. Thus, the main reason for capacity degradation after 50 cycles was not electrode disintegration. We considered mechanism of capacity decay as follows. A volume of Si expands up to 380% when Si reacts with Li to form $Li_{15}Si_4$, and repeating volumetric change during charge–discharge cycling damages a surface film on the Si electrode. While VC is decomposed at newly exposed electrode surface,

5 vol.% might be almost consumed during repeating several tens cycle. As a result, EMI cation eventually is reductively decomposed and passivation of anode proceeds. Hence, 5 vol.% VC was insufficient to form stable surface film for long term cycling and the discharge capacity started to decay at around 50th cycle (Figure 4-3c). To address this issue, the author furthermore added VC (total 20 vol.%) to EMI-based electrolyte. A discharge capacity gradually increased in this electrolyte. This is possibly due to activation process of Si electrode. In contrast to 5 vol.% VC, the electrode achieved a high cycling stability with a discharge capacity of 1500 mA h g^{-1} after 200 cycles. This is because VC-derived surface film is formed on the electrode in the presence of sufficient amount of VC, and it suppresses reductive decomposition of EMI cation over 200 cycles.
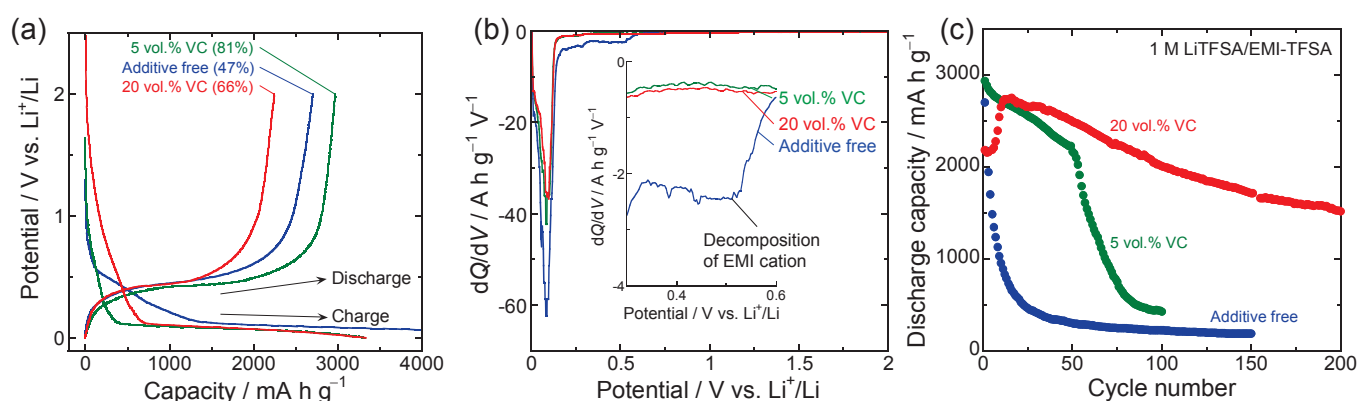
Figure 4-3. (a) Charge–discharge (Li-insertion/extraction) property, (b) differential capacity vs. voltage (dQ/dV) curves, and (c) cycling performance of Si electrode in 1 M LiTFSA/EMI-TFSA without and with 5 vol.% or 20 vol.% VC. The initial charge capacity obtained in the 1 M LiTFSA/EMI-TFSA without additive was 5730 mA h g^{-1}.
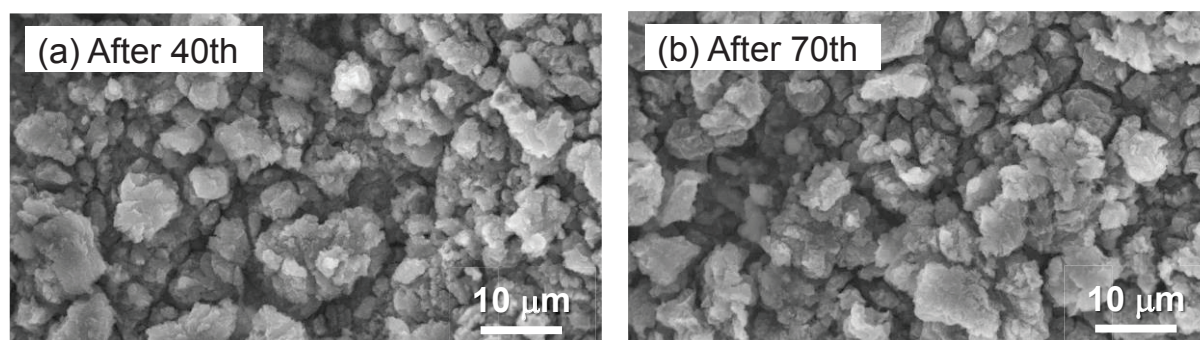
Figure 4-4. FE-SEM images of Si electrodes after (a) 40 and (b) 70 charge−discharge cycles in 1 M LiTFSA/EMI-TFSA with 5 vol.% VC.

EIS measurement was conducted to reveal the reason for suppression of capacity decay in the VC-added electrolyte. Figure 4-5a displays Nyquist plot of Si electrode charged at 0.005 V vs. Li$^+$/Li after the 1st and 40th cycles. In additive free electrolyte, interfacial resistance of Si electrode at the 40th cycle became approximately four-fold compared to that at the 1st cycle. This suggests Li$^+$ insertion into Si electrode is hardly to occur at the 40th cycle due to the decomposition of EMI cation. On the other hand, the resistance was significantly low at the 1st cycle in the 20 vol.% VC-added electrolyte and exhibited almost no change at the 40th cycle. Figure 4-5b shows change in the interfacial resistance of Si electrode versus cycle number in the electrolyte without/with 20 vol.% VC. The resistance increased quickly in first 20 cycles in the additive free electrolyte, whereas it mildly increased until the 80th cycle in the VC-added electrolyte. This means Li$^+$ can smoothly migrate at the electrode/electrolyte interface. Consequently, VC-derived surface film can suppress the decomposition of EMI cation to maintain low resistance, leading to better cycling performance.
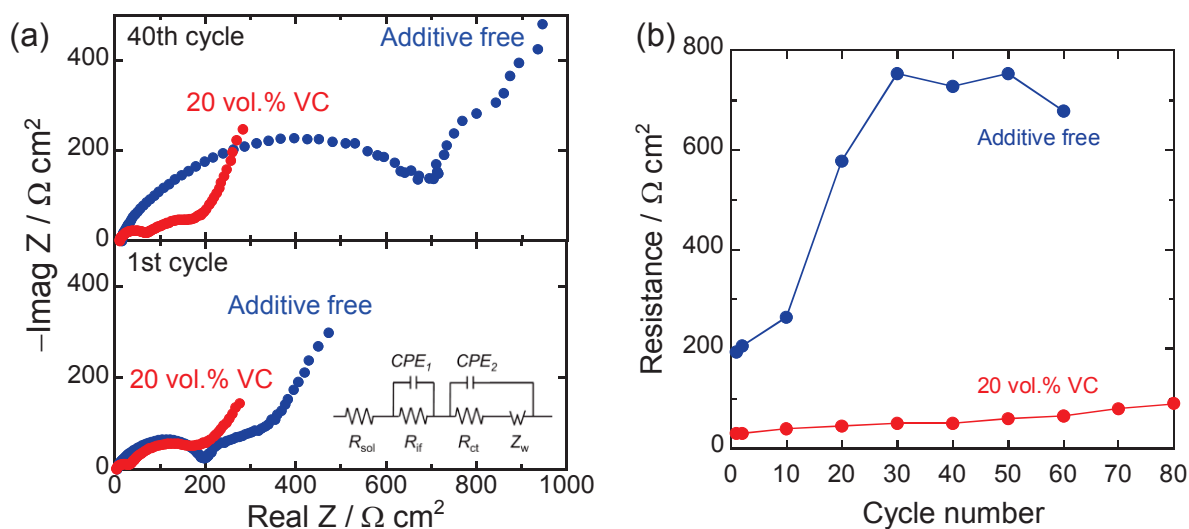
Figure 4-5. (a) Nyquist plots of cell including the electrode charged at 0.005 V in the first cycle. Inset: Randles circuit used in this study for analysis of cell impedance. (b) Change in interfacial resistance of Si electrode versus cycle number in 1 M LiTFSA/EMI-TFSA with and without 20 vol.% VC.

As electrolyte additives, fluoroethylene carbonate (FEC) is also utilized to improve electrochemical performance of anodes for LIBs. The author tried to reveal either VC or FEC is better electrolyte additive for EMI-based electrolyte. Figure 4-6a and b shows charge–discharge profiles and corresponding dQ/dV profiles of Si electrodes at the first cycle in FEC-added LiTFSA/EMI-TFSA. By adding FEC, potential gradient and broad peak at around 0.6 V vs. Li$^+$/Li on charge curve disappeared, which means that FEC also can suppress the decomposition of EMI cation. However, additional plateau appeared at 0.8 V vs. Li$^+$/Li in the electrolyte with 20 vol.% FEC, and the Coulombic efficiency did not increase (42%). Since a reduction potential of FEC is around 1.1 V[94], it is unclear the origin for this irreversible reaction at present state. Addition of FEC improved cycling stability, as shown in Figure 4-6c. However, degree of improvement was less than that in VC-added electrolyte; VC is better additive for EMI-TFSA.
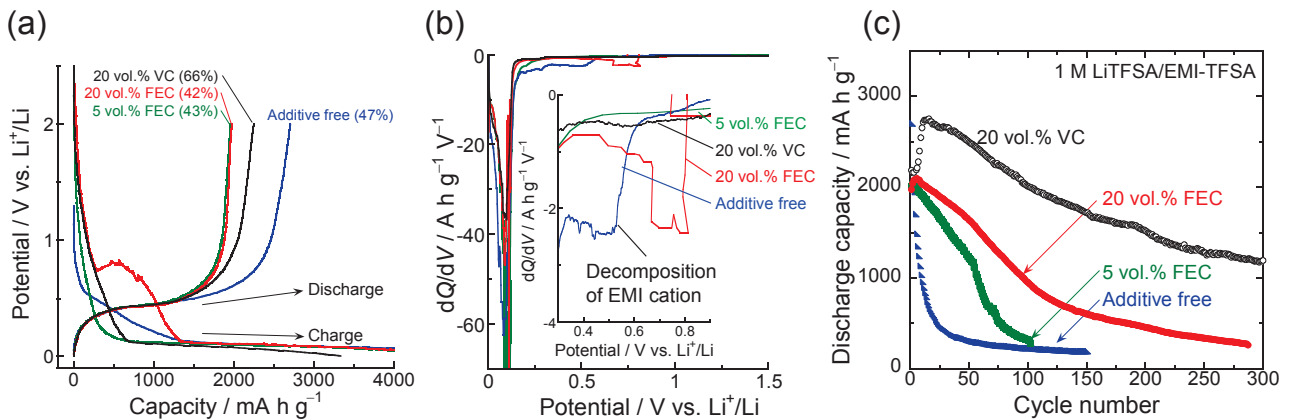
Figure 4-6. (a) Charge–discharge (Li-insertion/extraction) property, (b) differential capacity vs. voltage (dQ/dV) curves, and (c) cycling performance of Si electrode in 1 M LiTFSA/EMI-TFSA without and with 5 vol.% or 20 vol.% FEC.

As advantage of EMI-TFSA, they have lower viscosity and higher conductivity than pyrrolidinium-based ionic liquid electrolytes, such as Py13-TFSA. Thus, it is expected that Si electrode in EMI-TFSA exhibits superior rate capability to that in Py13-TFSA.[37] Figure 4-7

shows rate capability of Si electrode in TFSA-based electrolyte. Despite our expectation, poor rate capability was observed in 1 M LiTFSA/EMI-TFSA due to decomposition product of EMI cation. A relatively high discharge capacity of 2300 mA h g^{-1} was obtained at a low current density of 0.29 C (1050 mA g^{-1}) in 1 M LiTFSA/Py13-TFSA. However, the electrode exhibited only 590 mA h g^{-1} at 1.2 C (4200 mA g^{-1}) due to low conductivity of the Py13-based electrolyte (Table 4-1). In contrast, the rate capability of Si electrode was obviously improved in 20 vol.% VC-added electrolytes. This should be attributed to not only increase in the conductivity of electrolyte as shown in Table 1 but also formation of VC-derived surface film on the electrode to suppress continuous decomposition of the electrolytes. The best rate capability was achieved in 1 M LiTFSA/EMI-TFSA with 20 vol.% VC: a high capacity of 1500 mA h g^{-1} was maintained even at 1.2 C. As a consequence, it is clear that VC addition is effective to get potential out of EMI-TFSA.
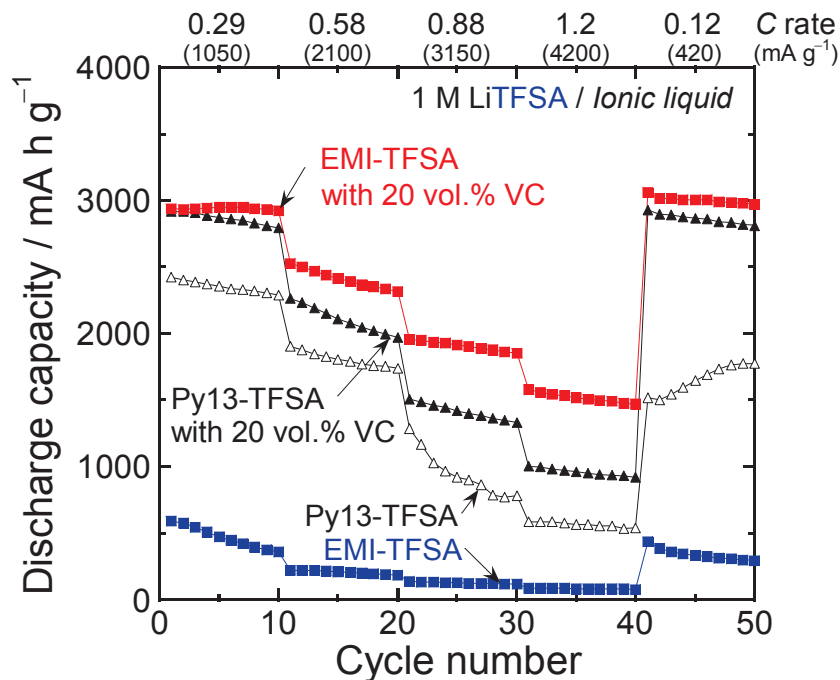
Figure 4-7. Rate performance of Si electrodes in 1 M LiTFSA/EMI-TFSA and 1 M LiTFSA/Py13-TFSA with/without 20 vol.% VC.

Table 4-1. Conductivity of EMI-based electrolytes without and with VC at 303 K.

	Conductivity / mS cm^{-1}	
	Without VC	With 20 vol.% VC
1 M LiTFSA/EMI-TFSA	4.9	10.5
1 M LiFSA/EMI-FSA	12.3	18.8

Electrochemical performance in an electrolyte consisted of EMI-FSA

The author also investigated the anion effect of EMI-based electrolyte on cycling performance of Si electrode. Figure 4-8a shows charge–discharge profiles of Si electrodes at the first cycle in an electrolyte of 1 M LiFSA/EMI-FSA without and with 20 vol.% VC. Figure 4-8b shows corresponding dQ/dV profiles. As with TFSA-based electrolytes, potential plateaus were observed at 0.1 V on charge curve and 0.4 V on discharge curve, respectively. However, a broad peak at 0.6 V did not appear even in additive free electrolyte and a new potential gradient appeared at around 1.5 V on charge curve. This is attributed to decomposition of FSA anion.[15] Thus, the FSA-derived surface film was preferentially formed on the electrode to probably suppress reductive decomposition of EMI cation. Coulombic efficiency in the 1 M LiFSA/EMI-FSA (64%) was higher than that in 1 M LiTFSA/EMI-TFSA (47%). The efficiency further increased to 74% by 20 vol.% VC addition. This result suggests that VC adding to FSA-based electrolyte is also effective to improve a reversibility of charge–discharge reaction.
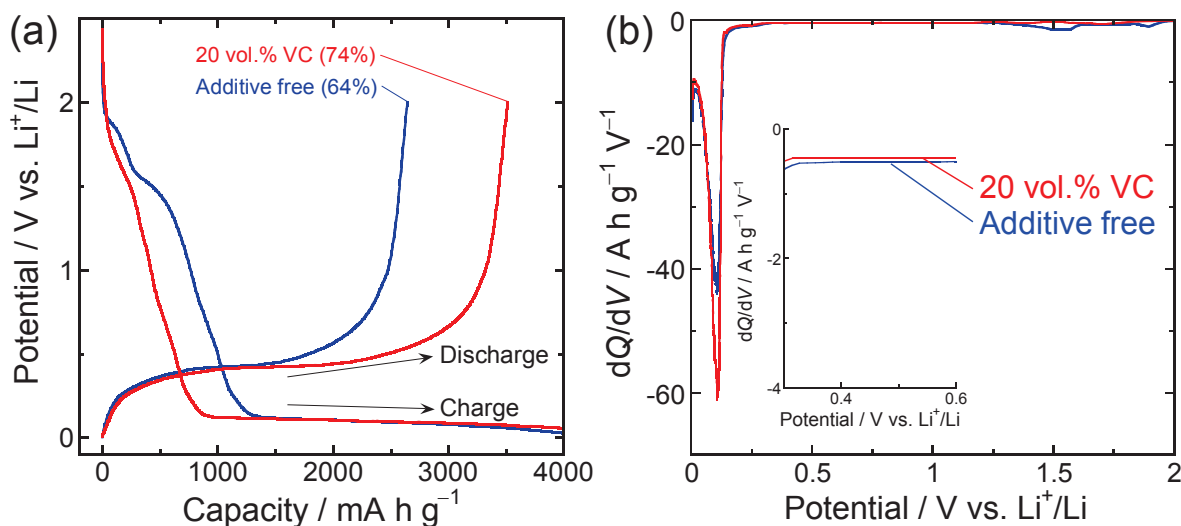
Figure 4-8. (a) Charge–discharge (Li-insertion/extraction) property of Si electrode in 1 M LiFSA/EMI-FSA without and with 20 vol.% VC. The initial charge capacity obtained in the 1 M LiFSA/EMI-FSA without and with 20 vol.% VC was 4250 and 4740 mA h g^{-1}, respectively. (b) Differential capacity vs. voltage (dQ/dV) curves of the electrodes in the respective ionic liquid electrolytes. Inset: enlarged view of the curves.

Figure 4-9 shows long-term cycling performance of Si electrode in 1 M LiFSA/EMI-FSA without and with 20 vol.% VC. The electrode maintained a discharge capacity of 500 mA h g^{-1} after 1000 cycles even in additive free electrolyte. This performance was comparable with that in 1 M LiTFSA/EMI-TFSA with 20 vol.% VC, indicating that FSA-derived surface film acts as a protective film suppressing reduction of EMI cation. Surprisingly, much higher cycling stability was obtained in 1 M LiFSA/EMI-FSA with 20 vol.% VC: the Si electrode maintained a high discharge capacity of more than 1000 mA h g^{-1} over 1500 cycles. This excellent performance was probably attributed to composition of surface film on the Si electrode. As well known, decomposition product of FSA anion is LiF, Li$_2$O, Li$_2$SO$_4$, LiNSO$_2$ and so on.[17,95] LiF and Li$_2$O have extremely high thermodynamic stability, which are good component for surface film to enhance its structural stability.[17] In addition, FSA-derived surface film is relatively thin and homogeneous.[95–97] On the other hand, VC-derived surface film is composed of mainly poly(VC), Li$_2$CO$_3$, Li$_2$C$_2$O$_4$ etc.[89,98–101] Poly(VC) is insoluble polymer to be useful for

63

fabrication of stable surface film during charge–discharge cycling. Michan *et al.* suggested that poly(VC) would likely aid surface film elasticity helping to solve the problem of uncontrolled surface-film growth and cracking in the surface film due to the large volumetric change of the Si active materials.[99] Combination of these components possibly makes more stable surface film for long-term cycling to inhibit electrolyte decomposition.
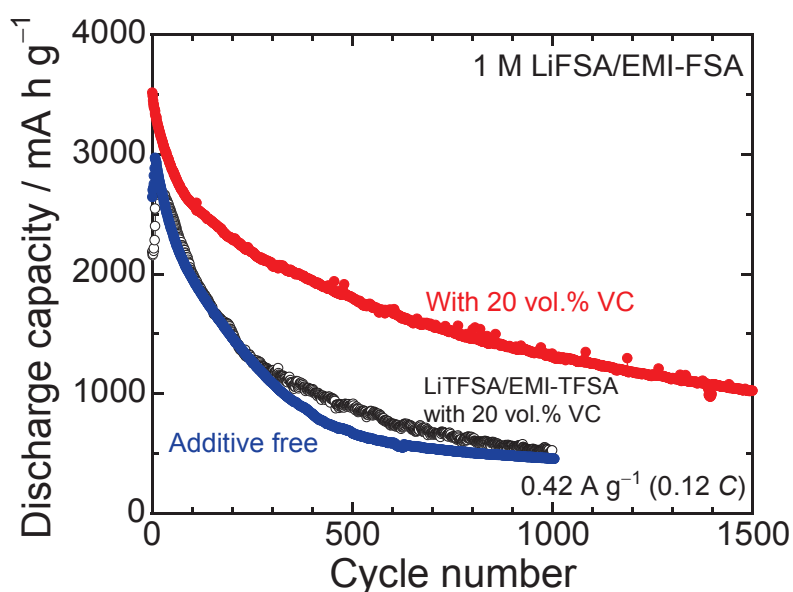

Figure 4-9. Long-term cycling performance of Si electrode in 1 M LiFSA/EMI-FSA without and with 20 vol.% VC at current density of 420 mA g^{-1} (0.12 *C*). Black open circle corresponds the performance in 1 M LiTFSA/EMI-TFSA with 20 vol.%.

We have demonstrated that a cycle life of a Si-based electrode can be prolonged by moderately controlling the amount of Li insertion–extraction.[57,63,71,72,102] To clarify the merit of using EMI-based electrolyte, a cycle life of Si-alone electrode (Figure 4-10) was investigated under Li extraction capacity limited to 1500 mA h g^{-1} which is approximately four times higher than graphite electrode. Cycle lives of Si electrodes were 780 and 1150 cycles in 1 M LiTFSA/EMI-TFSA with 20 vol.% VC and 1 M LiFSA/EMI-FSA, respectively. Cycling stability without capacity limit in 1 M LiFSA/EMI-FSA was comparable to that in 1 M LiTFSA/EMI-TFSA with 20 vol.% VC, as shown in Figure 7. On the other hand, the cycle

life in 1 M LiFSA/EMI-FSA was obtained 1.5 times as long as that in VC-added TFSA-based electrolyte under capacity limit of 1500 mA h g^{-1}. This result suggests that the FSA-derived surface film rather than the VC-derived one effectively contributes to improving cycle life of Si electrode if change in the volume of Si was moderately suppressed. Since the VC-derived film is tolerant to change in the volume of Si active materials, controlling Li-extraction amount might be less effective to improve the cycle life. In 1 M LiFSA/EMI-FSA with 20 vol.% VC, an excellent cycle life was attained with a reversible capacity of 1500 mA h g^{-1} beyond at least 1600 cycles. In this measurement also, cutoff potential was set between 0.005–2.0 V vs. Li^+/Li. However, a discharge cutoff potential is stopped on the way if the discharge capacity comes at 1500 mA h g^{-1}. It reaches upper limit of 2.0 V when the capacity of 1500 mA h g^{-1} cannot be obtained. In fact, capacity decay started at the 1150th cycle where cutoff potential reached 2.0 V in 1 M LiFSA/EMI-FSA. Thus, the discharge cutoff potential enables us to predict cycle life of the electrode. The cycle life in 1 M LiFSA/EMI-FSA with 20 vol.% VC can be much longer than that in the electrolyte without VC because its cutoff potential has stably maintained approximately 0.7 V over 1600 cycles. We demonstrated that VC addition is effective approach to enhance cycle life of Si electrode in FSA-based electrolyte also. This tendency was also observed in the case of discharge capacity limit of 1000 mA h g^{-1} (Figure 4-11). A cycle life in the electrolyte without VC under capacity limit of 1000 mA h g^{-1} was inferior to that in piperidinium-based electrolyte.[72]
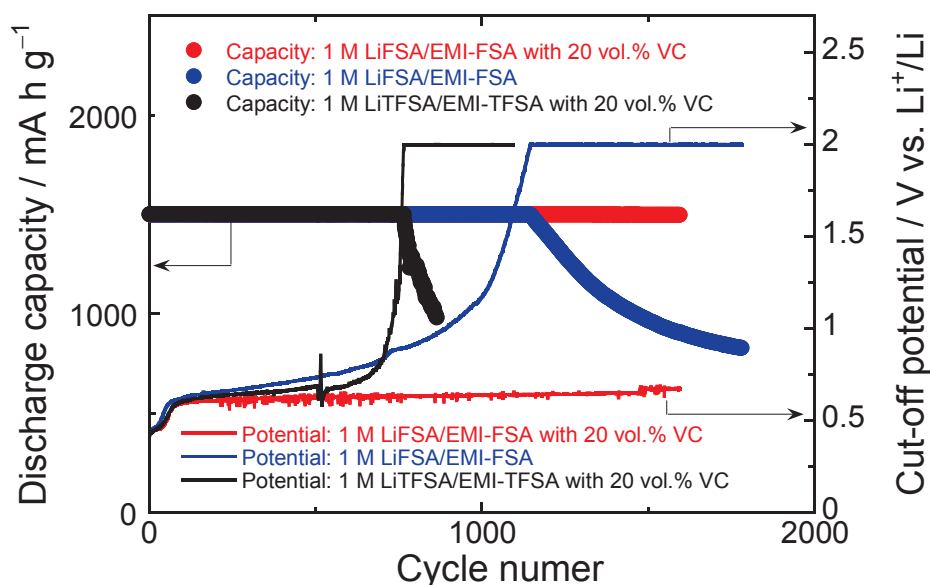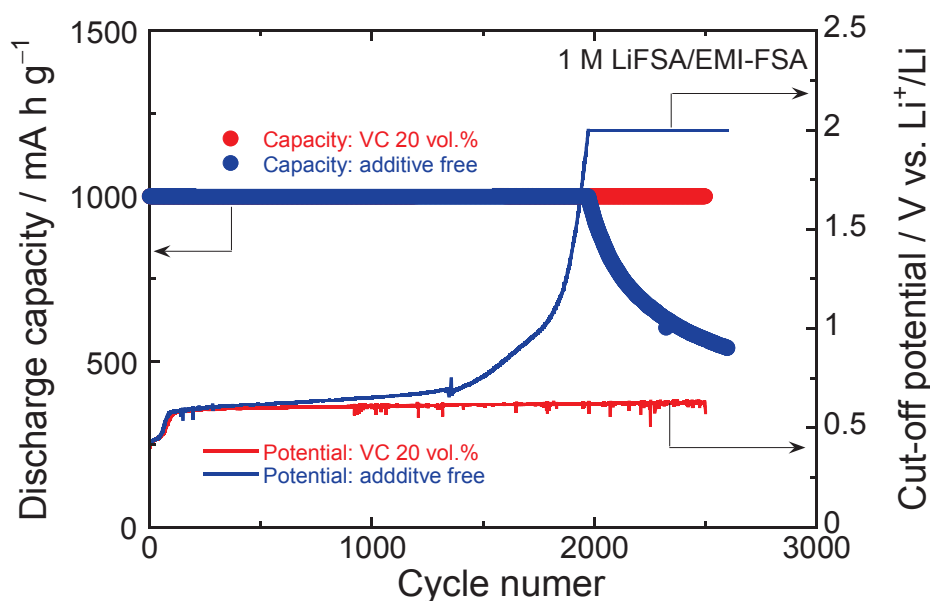
Figure 4-10. Variation in discharge capacity and discharge cut-off potential of Si electrode versus cycle number in 1 M LiFSA/EMI-FSA without and with 20 vol.% VC at current density of 420 mA g^{-1} (0.12 C) under discharge (Li-extraction) capacity limit of 1500 mA h g^{-1}.

Figure 4-11. Variation in discharge capacity and discharge cut-off potential of Si electrode versus cycle number in 1 M LiFSA/EMI-FSA without and with 20 vol.% VC at current density of 0.42 A g^{-1} (0.12 C) under discharge (Li-extraction) capacity limit of 1000 mA h g^{-1}.

The electrolytes consisted of EMI-FSA have very high ionic conductivity, which is superior to electrolytes consisted of EMI-TFSA (Figure 4-12 and Table 4-1). By adding VC to the electrolytes, the conductivity increased furthermore. Based on these conductivities, the author expected that the combination of EMI-FSA with VC enable Si electrode to exhibit

high rate capability beyond that in EMI-TFSA with VC. Figure 4-13 shows rate capability of Si electrode in the electrolyte consisted of EMI-FSA. Rate capability in 1 M LiFSA/EMI-FSA exceeded the performance in 1 M LiTFSA/EMI-TFSA with VC. For the combination of EMI-FSA with VC, higher performance was obtained: the electrode retained a discharge capacity of 2200 mA h g^{-1} and a capacity retention of 73% even at a current density of 4200 mA g^{-1} (1.2 C). It is noteworthy that this electrolyte can achieve such high rate capability without any structural design or surface modification of Si active material. The author concluded that the combination of LiFSA/EMI-FSA with VC is one of the best electrolytes to enhance the cycling stability and rate capability of Si-based electrolyte.
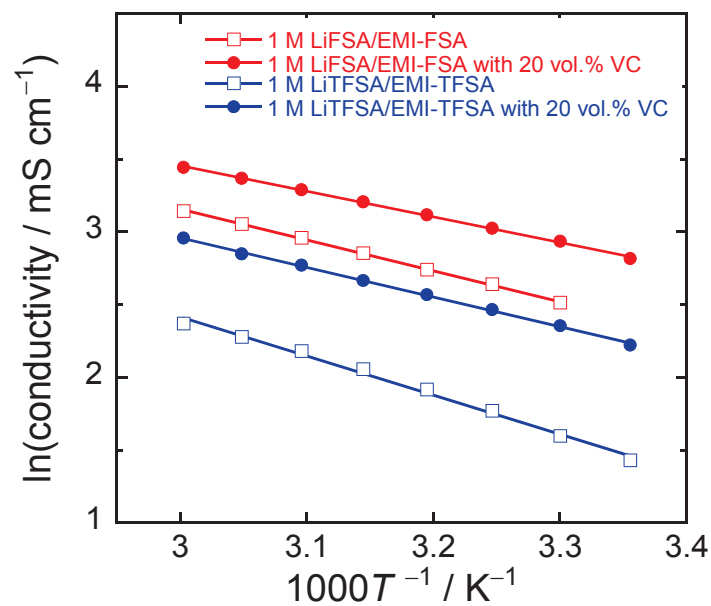
Figure 4-12. Temperature dependence of ionic conductivity of ionic liquid electrolytes with and without 20 vol.% VC.

67
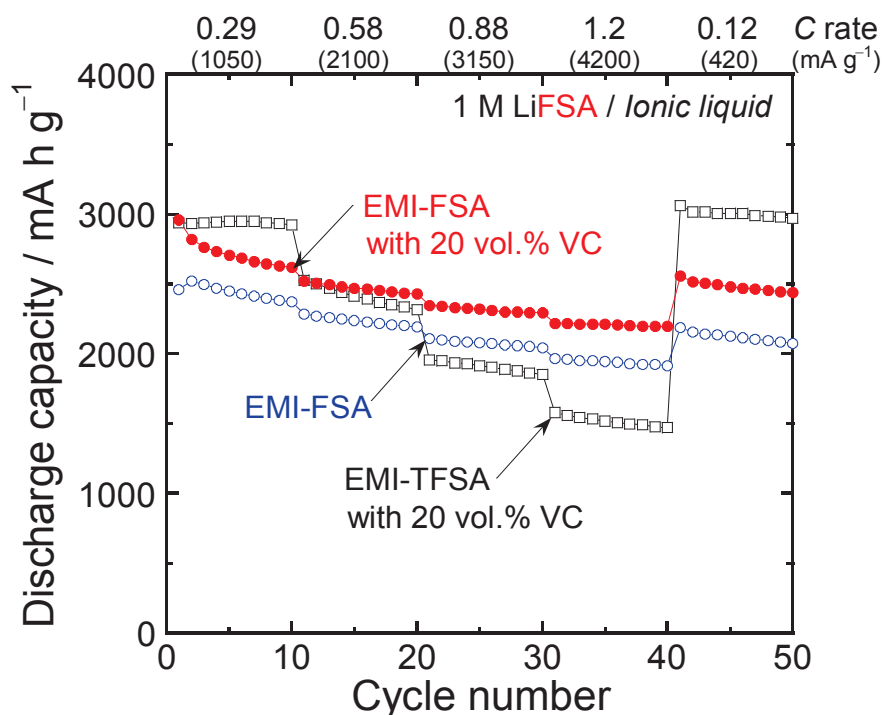
Figure 4-13. Rate performance of Si electrodes in 1 M LiFSA/EMI-FSA without and with 20 vol.% VC. The result in 1 M LiTFSA/EMI-TFSA with 20 vol.% VC was also shown.

Interaction of Li$^+$ and counter anion in ionic liquid

The author demonstrated that VC addition can increase the conductivity of EMI-based electrolyte. However, only increase in conductivity might be insufficient to explain the reason why rate capability of Si electrode is improved, because electrostatic interaction between Li$^+$ and counter anion in ionic liquid is too strong to cycle under high current density in general. Hardwick *et al.* reported that the electrostatic interaction between Li$^+$ and TFSA$^-$ is decreased by adding 2 M ethylene carbonate or VC to 0.5 M LiTFSA-dissolved EMI-TFSA.[103] Hence, the author tried to elucidate the interaction between Li$^+$ and counter anion in the 20 vol.% VC-added electrolytes used in this study. Figure 4-14 shows Raman spectra of the electrolytes without and with VC. The intense bands were observed at 742 cm^{-1} in Figure 4-14a, which is attributed to the CF$_3$ bending vibration δ_s (CF$_3$) coupled with the S−N stretching vibration ν_s (S−N−S) of the TFSA anion.[104–106] It is well known that the band position of 742 cm^{-1} shifts to 748 cm^{-1} by coordination of TFSA anions to Li$^+$. Unfortunately,

this band overlapped with Raman band at 742 cm^{-1} ascribed to skeletal breathing of VC[107], complicating the peak deconvolution for analyzing. On the other hand, in Figure 4-14b, the relatively intense bands were observed at 731 cm^{-1} and 1220 cm^{-1} attributed to the S−N stretching vibration ν_s (S−N) and the S−O stretching vibration ν_s (S−O) of the FSA anion without interaction (free FSA), respectively.[44] The band at 1220 cm^{-1} is also affected by coordination of FSA anions to Li$^+$ and does not overlap with VC-derived bands. Thus, the author focused on the band at 1220 cm^{-1} to determine the effect of VC addition on interaction between Li$^+$ and FSA$^-$ anions.
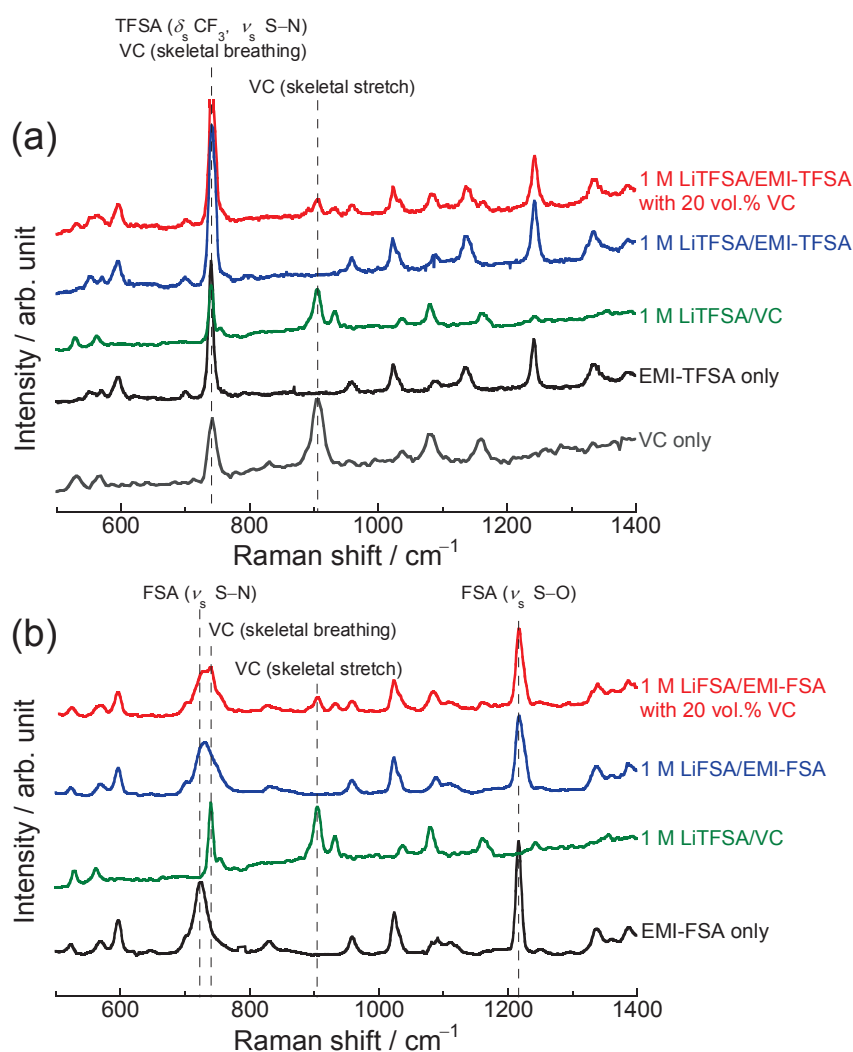
Figure 4-14. Raman spectra of (a) 1 M LiTFSA/EMI-TFSA and (b) 1 M LiFSA/EMI-FSA without and with 20 vol.% VC. For comparison, spectrum of 1 M LiTFSA/VC, VC, EMI-TFSA, and EMI-FSA was also shown in this figure.

Figure 4-15 shows the Raman spectra for the neat ionic liquid and the electrolyte containing LiFSA with/without VC in the wavenumber range of 1190 to 1250 cm^{-1}. Shoulder at around 1230 cm^{-1} was newly observed, which is ascribable to the FSA$^-$ solvating to the Li$^+$ ion in ionic liquid (Li$^+$-FSA), regardless of the presence/absence of VC.[44] However, the intensity in the electrolyte with VC was slightly lower compared to that without VC. The author conducted deconvolution of the Raman band, as shown in Figure 4-16. The relative intensity derived from Li$^+$-FSA in the VC-added electrolyte was less than that in the VC-free electrolyte. The ratio of peak intensity of Li$^+$-FSA to sum intensity of Li$^+$-FSA and free FSA ($I_{\text{Li+-FSA}}/(I_{\text{free FSA}}+I_{\text{Li+-FSA}})$) was 0.35 in the electrolyte without VC. On the other hand, the ratio was 0.24 in the electrolyte with VC. This means that VC reduces the interaction of FSA$^-$ with Li$^+$. Lower interaction leads to reduction of viscosity and high conductivity as well as smooth desolvation of FSA$^-$ from Li$^+$. This tendency is presumably in also the TFSA-based electrolyte. In addition, VC can also solvate to Li$^+$ because of its high relative permittivity. The Raman band at 905 cm^{-1} corresponds to skeletal stretch of VC (free VC).[107] The author confirmed that new Raman band appeared at around 930 cm^{-1} in 1 M LiTFSA/VC (Figure 4-17a). This Raman band was also observed in the EMI-based electrolytes with 20 vol.% VC, but did not appear in EMI-based ionic liquids (without Li salt) with 20 vol.% VC (Figure 4-17b). Therefore, this band should be attributed to the interaction between Li$^+$ and VC (Li$^+$-VC). The author calculated the ratio of $I_{\text{Li+-VC}}/(I_{\text{free VC}}+I_{\text{Li+-VC}})$ and summarized in Table 4-2. The ratio in the VC-added electrolytes was same or more than that in 1 M LiTFSA/VC. From this result, the author propose that VC solvates Li$^+$. Since VC is electrically neutral unlike component of ionic liquids, the interaction between Li$^+$ and VC must be weaker compared to the electrostatic interaction between Li$^+$ and FSA$^-$/TFSA$^-$. The electrostatic interaction decreases with VC solvation, and desolvation process at the electrode–electrolyte

interface can proceed smoothly. This is one of the reasons for achieving better cycling performance and rate capability.
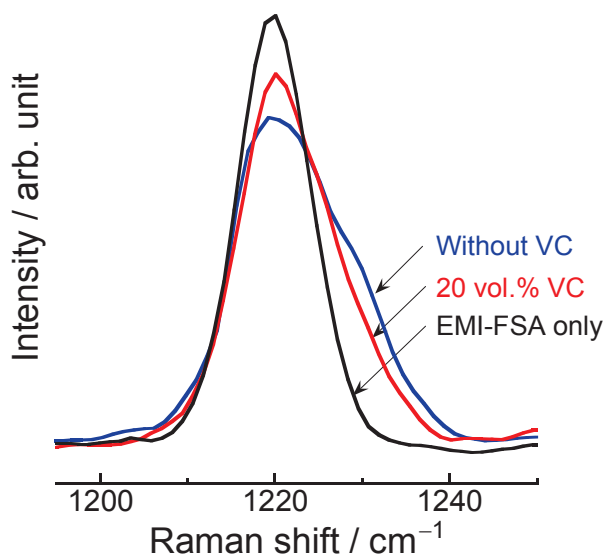

Figure 4-15. Raman bands of neat EMI-FSA and the 1 M LiFSA/EMI-FSA with and without VC in the wavenumber range of 1190 to 1250 cm^{-1}.
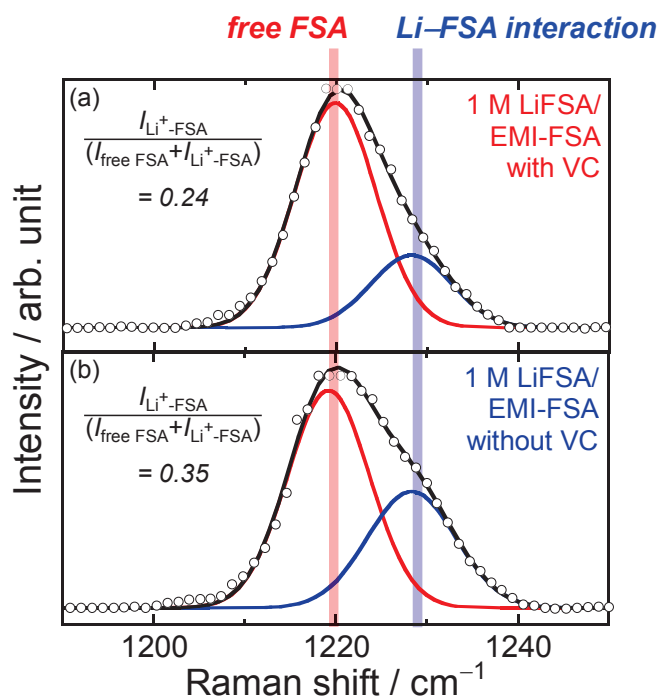

Figure 4-16. Deconvoluted Raman bands of 1 M LiFSA/EMI-FSA (a) with and (b) without 20 vol.% VC.
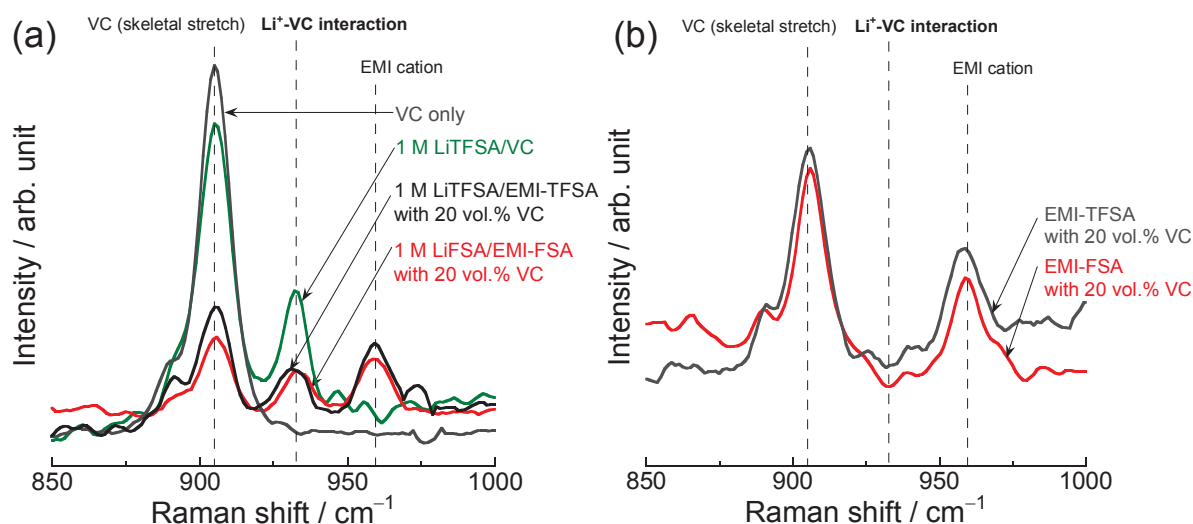
Figure 4-17. Raman spectra of (a) 1 M Li-salt-dissolved EMI-based electrolytes with 20 vol.% VC and (b) EMI-based ionic liquids with 20 vol.% VC in the wavenumber range of 850 to 1000 cm^{-1}.

Table 4-2. Ratio of peak intensity of Li$^+$-VC against sum intensity of Li$^+$-VC and free VC, namely $I_{Li+-VC}/(I_{free\ VC}+I_{Li+-VC})$ calculated by Figure S7a.

	$I_{Li+-VC}/(I_{free\ VC}+I_{Li+-VC})$
1 M LiTFSA/EMI-TFSA with 20 vol.% VC	0.30
1 M LiFSA/EMI-FSA with 20 vol.% VC	0.41
1 M LiTFSA/VC	0.29

Non-flammability estimation of VC-added electrolytes

VC effectively exerted advantage of EMI-based ionic liquid electrolyte, and thus electrochemical performance of Si electrode significantly improved. However, the electrolytes contained not only ionic liquid but also vinylene carbonate which is combustible, leading to fear to lose non-flammab ility of ionic liquid. Therefore, the author evaluated non-flammability of the electrolytes with VC by using a flash point tester (Figure 4-18a). Generally, flammability evaluation of ionic liquid electrolytes has been examined by directly exposing it to a test flame at room temperature.[108,109] The vapor of the electrolyte generated

72

by the heat hardly reaches its limit of inflammability because of an open-system measurement, though this test is a simple to easily understand. From this reason, the results have fear to be overestimated. On the other hand, the closed-system evaluation method (Rapid equilibrium closed cup method) used in this study is prescribed by ISO-standard and JIS. The flame retardant property can be evaluated with a good accuracy and reproducibility. We have introduced this technique as the evaluation method for non-flammability of ionic liquid electrolytes for the first time, and demonstrated its availability.[92,93] Figure 4-18b-d shows fire resistance test results of the VC-added electrolytes. The author also examined for 1 M LiTFSA/PC as a conventional organic electrolyte. The organic electrolyte ignited with a large flame at the relatively low temperature of 135 $^{\circ}$C (Figure 4-18b). In contrast, no fire was observed in both of 1 M LiTFSA/EMI-TFSA (Figure 4-18c) and 1 M LiFSA/EMI-FSA (Figure 4-18d) in spite of containing 20 vol.% VC even at 300 $^{\circ}$C which is measurement limit. The non-flammability of the VC-added ionic liquid electrolytes was clearly demonstrated by this method. From these results, the author revealed that the EMI-based electrolyte with VC, especially 1 M LiFSA/EMI-FSA with 20 vol.% VC, is very promising in order to not only improve electrochemical performance of Si-based electrode but also to effectively increase safety of batteries.
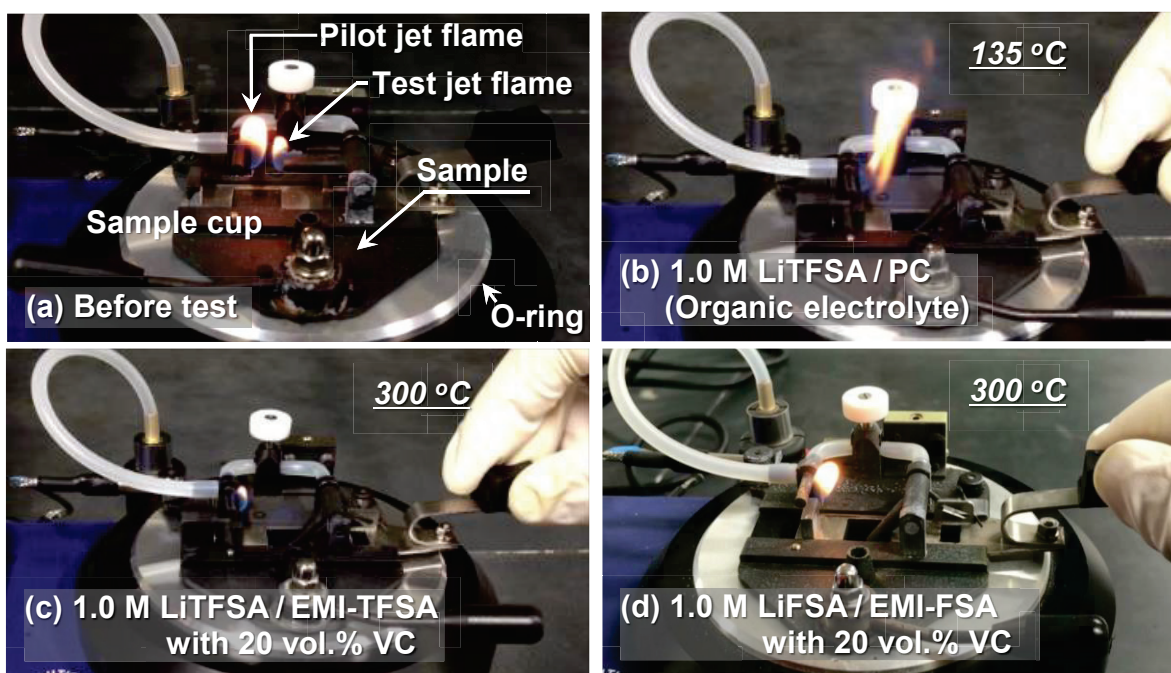
Figure 4-18. (a) Photographs of fire-resistance tester (Setaflash Series: 33000-0). Fire-resistance tests of (b) 1.0 M LiTFSA/PC (organic electrolyte), (c) 1.0 M LiTFSA/EMI-TFSA with 20 vol.% VC, and (d) 1.0 M LiFSA/EMI-FSA with 20 vol.% VC.

4.4 Summary

In this study, the author investigated the effect of adding VC as film-forming additive to EMI-based ionic liquid electrolytes on the electrochemical performance of Si-alone electrode for LIBs. The electrode exhibited an excellent cycling stability in 1 M LiFSA/EMI-FSA with 20 vol.% VC: a remarkably high capacity of 1500 mA h g^{-1} was maintained even after 1000 cycles, which was higher than that in EMI-TFSA-based electrolyte. This might be because the surface film derived from combination of FSA and VC is very stable during long-term cycling and suppresses the decomposition of EMI cation. An outstanding rate capability was also achieved in the electrolyte consisted of EMI-FSA and 20 vol.% VC. 1 M LiFSA/EMI-FSA with 20 vol.% VC had much higher conductivity of 18 mS cm^{-1} at 303 K compared to 1 M LiTFSA/EMI-TFSA with 20 vol.% VC. In addition, VC can solvate to Li$^+$ and reduce the electrochemical interaction between Li$^+$ and FSA. By achieving both of higher conductivity and smooth desolvation processes, outstanding rate capability can

be obtained in VC-added electrolyte. Fire retardancy test revealed that non-flammability of EMI-based electrolyte was maintained even containing 20 vol.% VC until at least 300 $^{\circ}$C. Although the composition of surface film on the Si electrode was insufficiently understood, the combination of VC and EMI-based electrolyte must be one of the most promising candidates to enhance the cycling stability and rate capability of Si-based electrolyte as well as the safety of LIBs.

Chapter 5

Enhanced Performance of Sn$_4$P$_3$ Anode for NIBs Cycled in Ionic Liquid Electrolyte at Intermediate Temperature

5.1 Introduction

Demands for stationary energy storage systems have been recently growing by applications for renewable energy and smart grid. Na-ion batteries (NIBs) have emerged as one of the potential alternatives for Li-ion batteries (LIBs) because of the huge abundant sodium resource and its low cost.[24,110] From the viewpoint of operation mechanism as rechargeable batteries, NIBs are very similar to LIBs. Charge−discharge reactions occur by insertion−extraction of alkali-metal ions into/from electrode active materials of these batteries. The LIBs electrode materials can provide beneficial references for developing the NIBs electrode materials because many Na-ion insertion hosts have their roots in Li$^+$-insertion hosts. The larger size and different bonding characteristics of Na$^+$, however, influence the thermodynamic and/or kinetic properties of NIBs, which leads to unexpected behavior in electrochemical performance and reaction mechanism, compared to LIBs.[111] For instance, graphite in practical use for LIBs anode does not show reversible charge−discharge reactions as NIBs anode.[112] Thus, NIBs active materials require an appropriate material design, which is similar to that of LIBs but different.

Hard carbons have disordered layered structure with nanopores, which has been reported to be suitable for reversible insertion and extraction of Na ions.[23,113,114] Komaba *et al.* have reported that the hard carbon electrode exhibited a good cycle stability and reversible capacities of 220−260 mA h g^{-1} for 100 charge−discharge cycles. In the most recently, the hard carbon electrode has maintained the reversible capacity of as high as 320 mA h g^{-1} for 100 cycles.[115] Although hard carbon is one of the promising candidates as NIBs anode

material, there are considerable interests in other anode materials showing better cyclability and higher capacity.

As NIBs anode materials, many researchers have particularly focused on titanium oxides, phosphorus (P), and tin (Sn). Titanium oxides can work as host materials for Na ions at lower electrode potentials than those of other transition metal oxides. Tarascon and Palacín have reported reversible Na-insertion/extraction of $Na_2Ti_3O_7$ at a low potential of 0.3 V vs. Na^+/Na.[116] Rudola $et\ al.$ have explored Na-ion storage in the structurally similar $Na_2Ti_6O_{13}$, demonstrating a reversible uptake by a solid solution mechanism at an average potential of 0.8 V vs Na^+/Na.[117] Although these sodium titanates are very promising as host materials, those have still suffered from their poor electronic conductivities as electrode materials. P and Sn are very attractive elements showing alloying−dealloying reactions because those have high theoretical capacities (Na_3P: 2596 mA h g^{-1} and $Na_{15}Sn_4$: 847 mA h g^{-1}). On the other hand, P and Sn have serious disadvantages. These elements show significant volume expansions of 490% and 525% when fully sodiated. Owing to such severe volume expansion/contraction, P electrode and Sn electrode cause the void space formation in active material layer and the electrode disintegration. In addition, a poor electronic conductivity of Na_3P phase disturbs electrode reactions of P electrodes. Small Sn nanoparticles react and merge together to form large agglomerates, resulting in acceleration of the disintegration. Consequently, P electrode and Sn electrode generally show a rapid capacity fading and a short cycle life.

To solve these problems, Hagiwara, Nohira, and Yamamoto have conducted systematic studies for several binary alloys consisting of Sn and transition metals, Cu−Sn,[118] Ni−Sn[119], and Fe−Sn.[120] The results of their studies indicate that Na-inactive elements (Cu, Ni, and Fe) are effective for improving the rapid capacity fading of Sn. Vogta and Villevieille have reported that $MnSn_2$ exhibited a stable cyclability based on its conversion reaction in addition

to the sodiation−desodiation reactions of Sn.[121] As phosphorus-based materials, Zhao *et al.* have demonstrated that CuP_2 is capable of reversible sodiation−desodiation based on the conversion mechanism.[122] On the other hand, the authors have applied two kinds of unique material designs, (i) the doping of impurity element and (ii) the formation of various compounds. As the result, we have succeeded to newly develop many anode materials: Nb-doped rutile TiO_2,[93,123,124] SiO,[125] SnO,[126] $LaSn_3$,[127] Sn_4P_3,[128,129] InP,[130] GeP,[130] and SiP.[130] A series of the material development has revealed that the best anode performance was obtained for Sn_4P_3, a compound of two Na-active elements. In 2014, Yang[131] and Kim[132] also have revealed that Sn_4P_3 electrodes exhibited good cycling performances in conventional organic electrolytes. Ahead of their reports, the authors have developed Sn_4P_3 as a potential anode material in 2013. In addition, the authors have firstly discovered that it exhibited an outstanding cycling performance by choosing an optimal ionic liquid electrolyte comprised of *N*-methyl-*N*-propylpyrrolidinium (Py13) cation and bis(fluorosulfonyl)amide (FSA) anion.[130] The Sn_4P_3 electrode achieved a high capacity of 750 mA h g^{-1} even at the 200th cycle under the charge−discharge current density of 50 mA g^{-1} at room temperature.

As the reason for the excellent property of this anode material, we suggest a complementary effect of Sn and P. After its phase separation at the first sodiation, an Sn phase functions as a conducting pathway to activate reversible desodiation of a nonconductive Na_3P, whereas the Na_3P phase provides a shield matrix preventing Sn aggregation.[128,131,132] We have confirmed that the first desodiation of Sn_4P_3 forms nanostructured domains in which crystalline Sn nanoparticles are dispersed in the amorphous-like P matrix.[129]

As an important role of the ionic liquid electrolyte, we have proposed the construction of a stable interface between electrode and electrolyte.[127,129] Py13 cations have a high electrochemical stability [19]. In charge reaction, FSA anions are decomposed to form a

chemically stable surface layer consisting of NaF and $NaSO_2F$.[133] The cations and the surface layer can suppress a continuous decomposition of electrolyte, and can improve charge−discharge efficiency. In addition, FSA-based ionic liquids have relatively low viscosity and high ionic conductivity among various ionic liquids because of flexible coordination structure of FSA anions.[44] Nevertheless, the conductivity of this ionic liquid at room temperature is still inferior to that of conventional organic electrolyte. [134] The elevation of the operating temperature is expected to improve the ion transport in the electrolyte. Intermediate temperatures between 60 ^{o}C and 90 ^{o}C can be sufficiently realized by using waste heat from factories and households. Therefore, in this study, the author evaluated the performance of the Sn_4P_3 anodes in the ionic liquid electrolyte at the intermediate temperatures.

5.2 Experimental Details

An active material powder of Sn_4P_3 was synthesized by a mechanical alloying (MA) using commercially available tin powder (99.99%, Rare Metallic) and red phosphorous powder (99.8%, Wako Pure Chemical). The MA treatment was conducted by a Fritsch planetary-type high-energy ball mill (Fritsch Pulverisette P-6) and a stainless steel vessel. The weight ratio of the active material and stainless steel balls was 1:30. The MA duration time and rotation speed were 10 hours and 380 rpm. The detailed procedure has been described in previous paper.[129] The active material obtained has a crystal structure of trigonal Sn_4P_3 (Inorganic Crystal Structure Database, ICSD No. 03-066-0017), which was confirmed by analysis using an X-ray diffraction (XRD, Ultima IV, Rigaku) as shown in Figure 5-1. Electrodes were prepared by using of Sn_4P_3/acetylene black/carboxymethyl cellulose/styrene-butadiene rubber with the weight ratio of 70/15/10/5 wt.%. The current collector was Al foil. The loading amount and the film thickness of active material layer were

79

1.2 mg cm^{-2} and 10 μm, respectively. Electrochemical measurements of Na-insertion (charge) and Na-extraction (discharge) were carried out for 2032-type coin half cells consisted of Na metal sheets and glass fiber separators. The author used ionic liquid electrolytes of 1.0 mol dm^{-3} NaFSA-dissolved in Py13-FSA. Galvanostatic charge−discharge tests were performed using an electrochemical measurement system (HJ-1001 SM8A, Hokuto Denko Co., Ltd.) under the current density of 100 mA g^{-1} (0.088 C) with potential ranges of 0.005−2.000 V vs. Na$^+$/Na. The measurements were conducted at a low temperature (0 $^{\circ}$C), room temperature (30 $^{\circ}$C), and intermediate temperatures (60 and 90 $^{\circ}$C). A cyclic voltammetry (CV) and an electrochemical impedance spectroscopic (EIS) analysis were performed by using an impedance analyzer (CompactStat.h 20250e, Ivium Technologies). The EIS measurements were done at 0.005 V vs. Na$^+$/Na with the potential amplitude of 5 mV in the frequency range of 100 kHz–10 mHz. Nyquist plots were analyzed by using Randles equivalent circuit (Figure 5-2) containing solution resistance (R_{sol}), surface film resistance (R_{sf}), and charge transfer resistance (R_{ct}). The conductivities of the electrolytes were evaluated for a symmetric cell of two platinum plates (Figure 5-3), demonstrating that the conductivities at 0, 30, 60, and 90 $^{\circ}$C were 1.5, 5.7, 12.7, and 20.0 mS cm^{-1}, respectively. As the author expected, the conductivity was improved with increasing the temperature. The results basically agree with the values reported by Ding *et al.* [135]
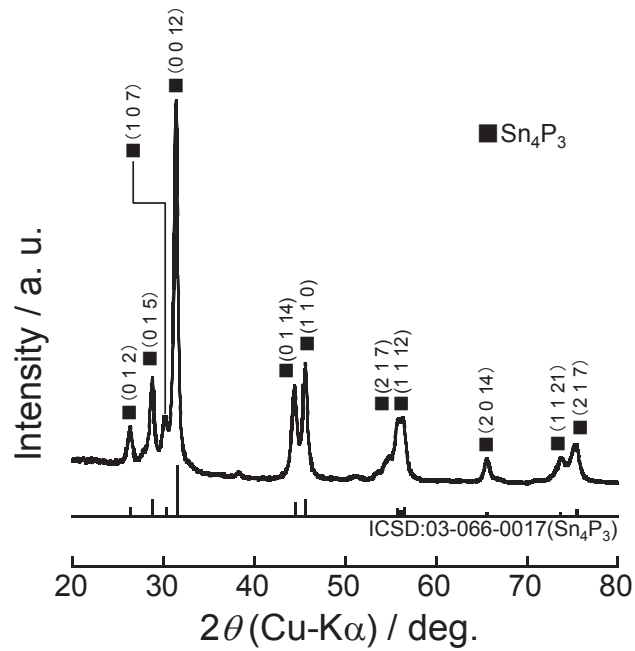
Figure 5-1. XRD pattern of active material powder prepared by mechanical alloying treatment for mixture of Sn and P. A single phase of Sn_4P_3 was confirmed.
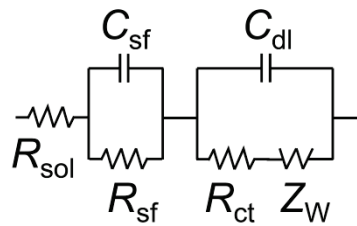

Figure 5-2. Randles circuit used for the fitting analysis. The circuit consisted of resistance of electrolyte (R_{sol}), surface film resistance (R_{sf}), charge-transfer resistance (R_{ct}), Warburg impedance (Z_W), and capacitances of surface film (C_{sf}) and electric double layer (C_{dl}). For analysis, constant phase elements were actually used instead of the capacitances to take into account the roughness of electrode surface.

Temperature / °C	Conductivity / mS cm^{-1}
0	1.5
30	5.7
60	12.7
90	20.0
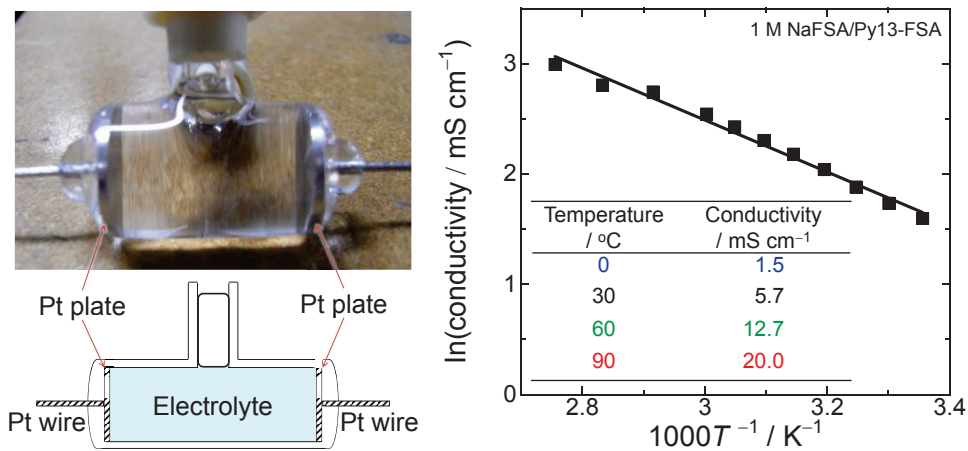
Figure 5-3. (a) A symmetric cell equipped with two platinum plates for conductivity measurements. (b) Results of conductivity measurements for the ionic liquid electrolyte (1 mol dm^{-3} NaFSA/Py13-FSA) at various temperatures.

5.3 Results and Discussion

As we have reported, Sn_4P_3 electrodes at the first charge−discharge cycle show the irreversible reaction caused by its phase separation.[129] Irreversible capacities were observed in galvanostatic charge−discharge cycling tests of this study: Coulombic efficiencies at the first cycles were 55.9%, 80.0%, 84.6%, and 82.5% at the temperatures of 0, 30, 60, and 90 ^{o}C, respectively (Figure 5−4a-d). The efficiencies steeply rose as high as 98% by the 5th cycles. This indicates that sufficiently reversible electrode reactions took place at the 5th cycles. Figure 5-5 show the charge (sodiation) and discharge (desodiation) potential profiles at the 5th cycles evaluated in the ionic liquid electrolyte at various temperatures. At 0 ^{o}C, a low charge capacity of 220 mA h g^{-1} was obtained. It is suggested that the electrode reaction of Sn_4P_3 was kinetically restricted by the poor electrolyte conductivity of 1.5 mS cm^{-1} at 0 ^{o}C. The charge capacity was significantly increased in the temperature range from 0 ^{o}C to 60 ^{o}C, whereas no remarkable increase was observed at 90 ^{o}C. The charge curve profile between 2.0 and 0.2 V vs. Na^+/Na at 30 ^{o}C almost entirely coincided with those at 60 and 90 ^{o}C. In the potentials below 0.2 V vs. Na^+/Na, charge capacities more than 400 mA h g^{-1} were produced at 60 and 90 ^{o}C, which was never confirmed at 30 ^{o}C.
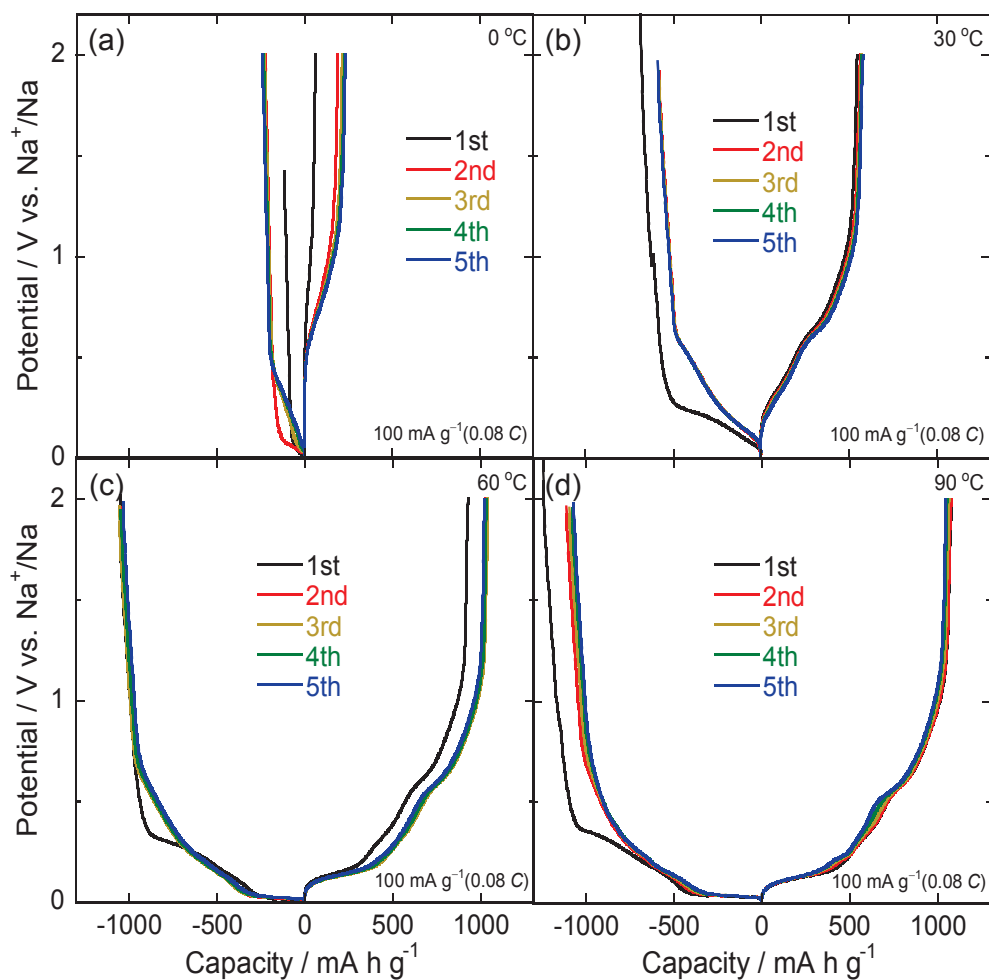
Figure 5-4. Charge−discharge curves of Sn$_4$P$_3$ electrode at the initial five cycles under 100 mA g^{-1} in NaFSA/Py13-FSA at the temperature of (a) 0, (b) 30, (c) 60, and (d) 90 ^{o}C.
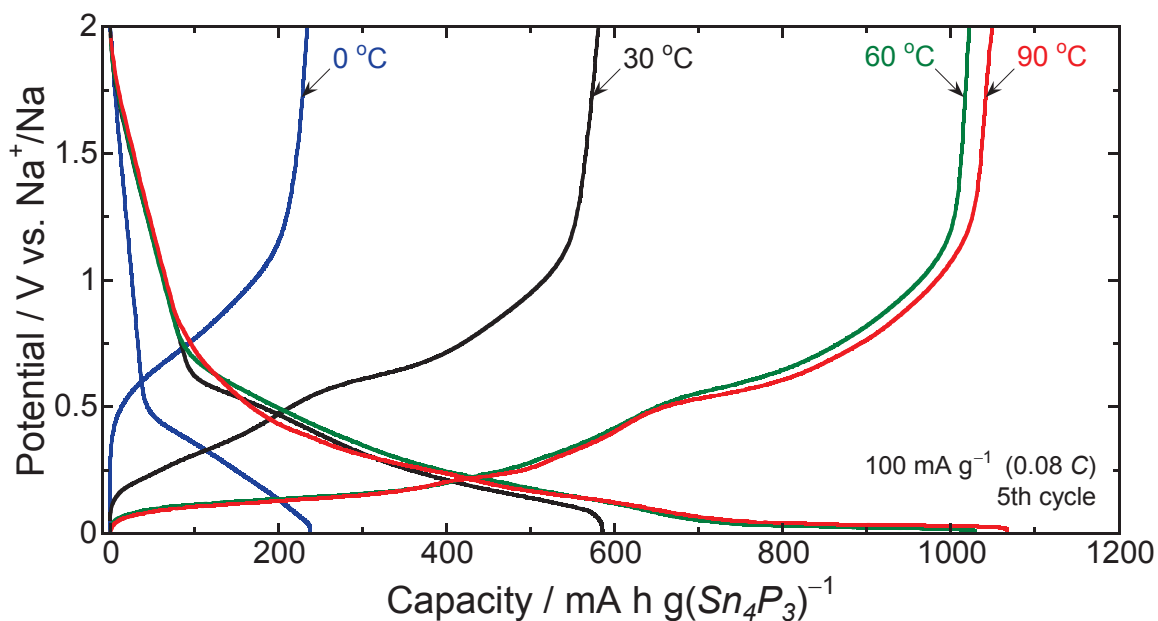

Figure 5-5. Charge–discharge curves of Sn$_4$P$_3$ electrode in the 5th cycles evaluated by using ionic liquid electrolyte (NaFSA/Py13-FSA) at various temperatures under the current density of 100 mA g^{-1}.

83

Figure 5-6 represents cyclic voltammograms of Sn_4P_3 electrodes in the ionic liquid electrolytes of NaFSA/Py13-FSA at various temperatures. At 0 °C, cathodic and anodic current densities were very small because of the low conductivity of electrolyte. At the temperatures equal to or higher than 30 °C, CV profiles showed multiple peaks. The authors [129] and other groups [131,132] have revealed that a disproponation of Sn_4P_3 occurs at the first cycle to form elemental Sn and P, and that Sn and P individually react with Na ions in the subsequent cycles. As Sn's electrode reactions, Obrovac *et al.* have found four potential peaks originating from phase transformation between Sn, $NaSn_3$, NaSn, Na_9Sn_4, and $Na_{15}Sn_4$: the charge (sodiation) peaks appeared at around 0.43, 0.20, 0.08, and 0.05 V vs. Na^+/Na, while the discharge (desodiation) peaks were observed at around 0.14, 0.23, 0.55, and 0.65 V vs. Na^+/Na. [136.137] The three peaks at the higher potentials often merged into one peak owing to the slow kinetics of Na diffusion in Sn. [137,138] As the result, two kinds of sodiation reactions are observed: $Sn + xNa^+ + xe^- \rightarrow Na_xSn$ and $Na_xSn + yNa^+ + ye^- \rightarrow Na_{15}Sn_4$. The authors also have previously confirmed two sodiation peaks at the potentials below 0.2 V vs. Na^+/Na. [127] As P's electrode reactions, Dahbi *et al.* [139] and Shimizu *et al.* [140] have reported that broad two or three peaks were observed for charge and discharge curves at 0.3−0.5 V and 0.5−0.8 V versus Na^+/Na, indicating the phase transformations between P, Na_3P_{11}, NaP, and Na_3P. [141] In this study, peak positions of the profile at 90 °C (Figure 5-6(d)) well agreed with those of Sn electrodes [136137,138] and P electrodes [139,140] previously reported. In the sodiation profile, cathodic peaks at 0.6, 0.25, and 0.12 V are attributed to phase transformation reactions of $P \rightarrow Na_3P_{11}$, $Na_3P_{11} \rightarrow NaP$, and $NaP \rightarrow Na_3P$. Anodic peaks by their reverse reactions appeared at 0.9 and 0.63 V. Although there is an overlapping of peak profiles, the author can recognize two cathodic peaks at 0.1 V ($Sn \rightarrow Na_xSn$) and 0.01 V ($Na_xSn \rightarrow Na_{15}Sn_4$). The reverse reactions were observed as anodic peaks at 0.32 and 0.19 V. At the temperatures of 30 and 60 °C, the author observed polarizations of these cathodic and anodic peaks. Note

that the cathodic peak intensity at 0.01 V was reduced with decreasing the temperature from 90 to 30 °C. The author considers that the $Na_{15}Sn_4$ formation reaction was considerably suppressed at the lower temperatures because of the polarization. The anodic peak intensity at 0.19 V ($Na_{15}Sn_4 \rightarrow Na_xSn$) was also reduced with decreasing the temperature, supporting our consideration.
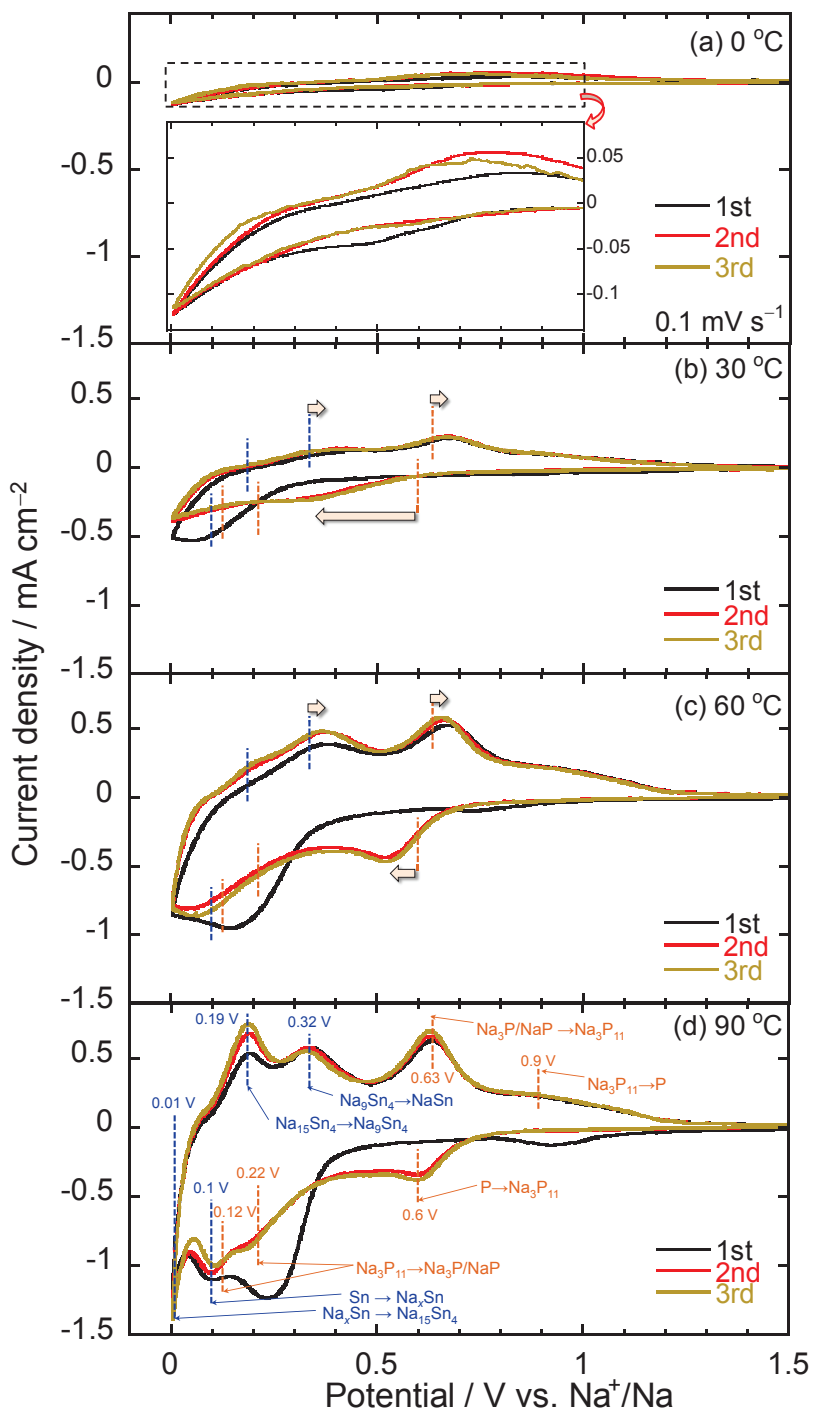

Figure 5-6. Cyclic voltammograms of Sn_4P_3 electrodes at (a) 0, (b) 30, (c) 60, and (d) 90 °C.

Figure 5-7 compares charge−discharge curves focusing on the lower potential ranges. By subtracting 410 and 450 mA h g^{-1} from the desodiation capacities at 60 and 90 $^{\circ}$C, the author can compare the desodiation curve profiles at lower potential ranges. Interestingly, the sodiation−desodiation profiles above 0.2 V vs. Na^{+}/Na at 60 and 90 $^{\circ}$C almost completely coincided with that at 30 $^{\circ}$C. This comparison demonstrated that the extra capacities of 410 and 450 mA h g^{-1} were produced at the low potential regions form 0 to 0.2 V vs. Na^{+}/Na, which is a benefit of the elevated temperature operation. The extra capacities are attributed to the full sodiation of Sn (Na$_x$Sn→Na$_{15}$Sn$_4$) and its reverse reaction (Na$_{15}$Sn$_4$→Na$_x$Sn). Even at the low temperature of 30 $^{\circ}$C, the extra capacity could be obtained by reducing the charge−discharge current density from 100 to 50 mA g^{-1} (Figure 5-8). It is considered that the elevation of operation temperature can improve the Sn's slow kinetics. This consideration was supported by results of an EIS analysis (Figure 5-9). The charge-transfer resistance (R_{ct}) at the full sodiation state was as large as 157 Ω when the temperature was 0 $^{\circ}$C, whereas it was drastically reduced to 8.0 Ω at 30 $^{\circ}$C. Furthermore, the resistance showed lower values of 2.3 and 1.7 Ω at 60 and 90 $^{\circ}$C, respectively.
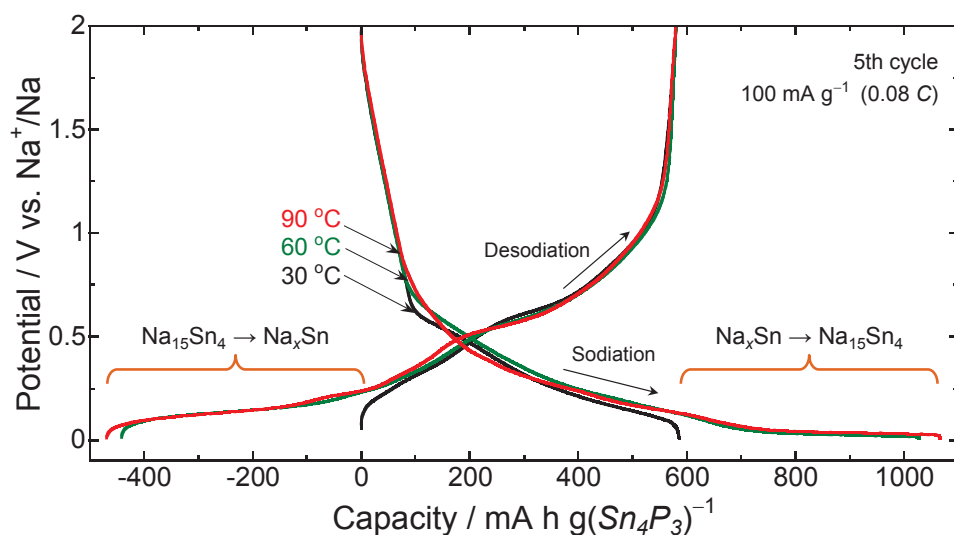

Figure 5-7. Charge−discharge curves of Sn$_4$P$_3$ electrode at the 5th cycles under the current densities of 100 mA g^{-1}. For desodiation curves at 60 and 90 $^{\circ}$C, the capacities of 410 and 450 mA h g^{-1} were subtracted so that the curve profiles can be compared.
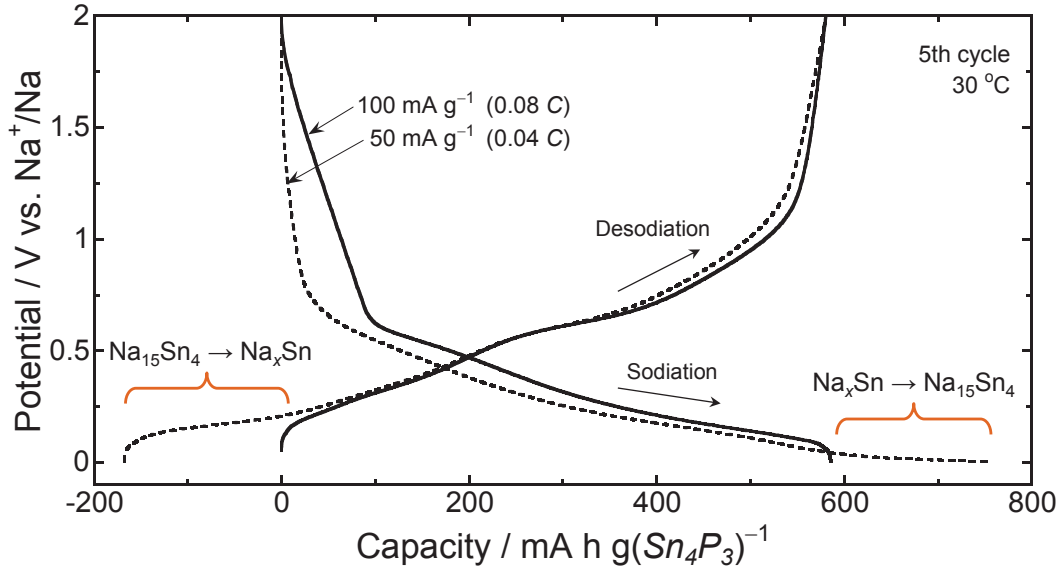
Figure 5-8. Charge–discharge curves of Sn_4P_3 electrode at the 5th cycles at 30 $^{\circ}$C under the current densities of 50 and 100 mA g^{-1}. For desodiation curves at 50 mA g^{-1}, the capacity of 170 mA h g^{-1} were subtracted so that the curve profiles can be compared.
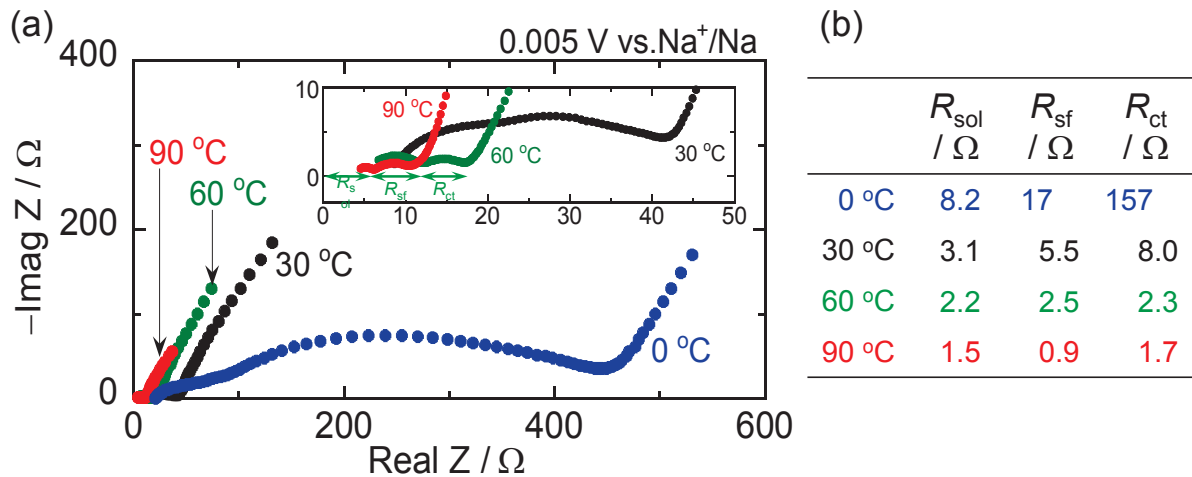

	R_{sol} / Ω	R_{sf} / Ω	R_{ct} / Ω
0 $^{\circ}$C	8.2	17	157
30 $^{\circ}$C	3.1	5.5	8.0
60 $^{\circ}$C	2.2	2.5	2.3
90 $^{\circ}$C	1.5	0.9	1.7

Figure 5-9. (a) Nyquist plots of Sn_4P_3 electrodes at 0.005 V vs. Na$^+$/Na at the first cycle in NaFSA/Py13-FSA electrolyte. The inset shows an enlarged profile of the plots at 30, 60, and 90 $^{\circ}$C in higher frequency region. (b) Results of the fitting analysis: resistance of electrolyte (R_{sol}), surface film resistance (R_{sf}), charge transfer resistance (R_{ct}).

Figure 5-10 shows cycling performances of Sn_4P_3 electrode cycled under the current density of 100 mA g^{-1} at various temperatures. In the range of 0 to 60 $^{\circ}$C, the discharge capacity was remarkably increased with increasing temperature. Especially at 60 $^{\circ}$C, the

Sn_4P_3 electrode exhibited very large capacities of approximately 1000 mA h g^{-1} in the initial cycles. It is notable that the capacities are comparable to the Sn_4P_3's theoretical capacity of 1133 mA h g^{-1}. This is probably because the electrode reaction of Sn_4P_3 progressed more efficiently at the elevated temperature by the reduced reaction resistance as well as the enhanced electrolyte conductivity. At the 60th cycle, 870 mA h g^{-1} was attained. Although the conductivity showed a further enhancement at 90 ^{o}C, no significant improvement in the discharge capacity was observed. After the 5th cycle, Coulombic efficiencies were more than 99% at 30 to 60 ^{o}C. By contrast, it remained only 98% at 90 ^{o}C. The decomposition of the electrolyte probably occurred owing to such high temperature.
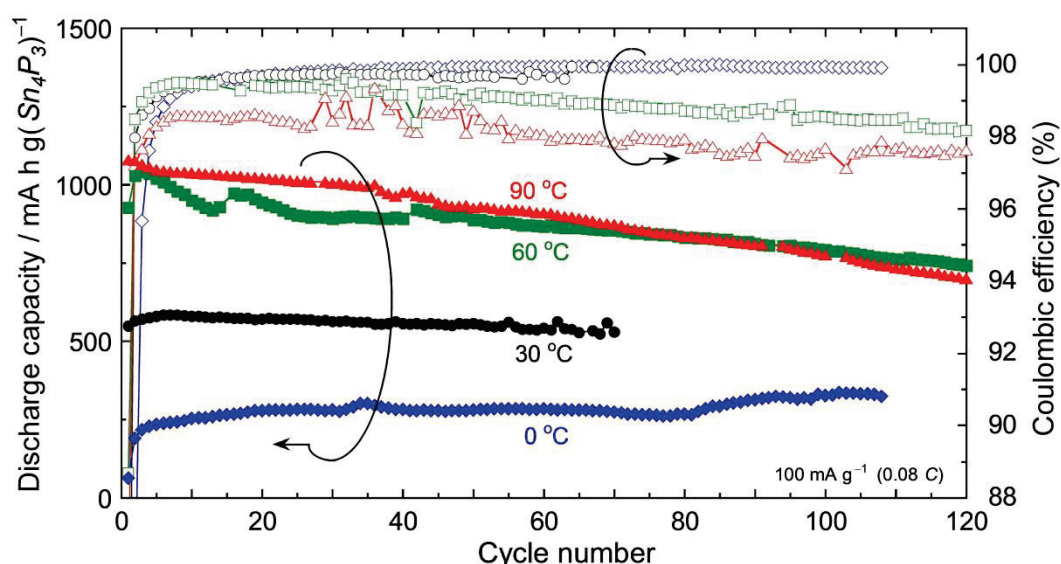

Figure 5-10. Variation in discharge capacity and Coulombic efficiency of Sn_4P_3 electrode cycled in NaFSA/Py13-FSA at various temperatures. The conductivities of the electrolytes at 0, 30, 60, and 90 °C were 1.5, 5.7, 12.7, and 20.0 mS cm-1, respectively (Figure 4-4).

Figure 5-11 gives results of rate capability measurements at various current densities. At a high current density of 1 A g^{-1} (0.88 C), the electrode lost almost all its discharge capacity at 0 ^{o}C, whereas it maintained 250 mA h g^{-1} at 30 ^{o}C. In contrast, the electrode exhibited excellent rate capabilities with the large capacities of 500 mA h g^{-1} at 60 and 90 ^{o}C.

At 3 A g^{-1} (2.65 *C*), the capacity was 250 mA h g^{-1} at 60 ^{o}C, which is superior to that of 230 mA h g^{-1} at 90 ^{o}C. This capacity corresponds to that of a hard carbon electrode under a very low current density of 0.2 A g^{-1} at room temperature.[142] The excellent rate performance demonstrated that Sn$_4$P$_3$ anode in ionic liquid electrolyte at intermediate temperature around 60 ^{o}C is very promising for high-performance NIBs.
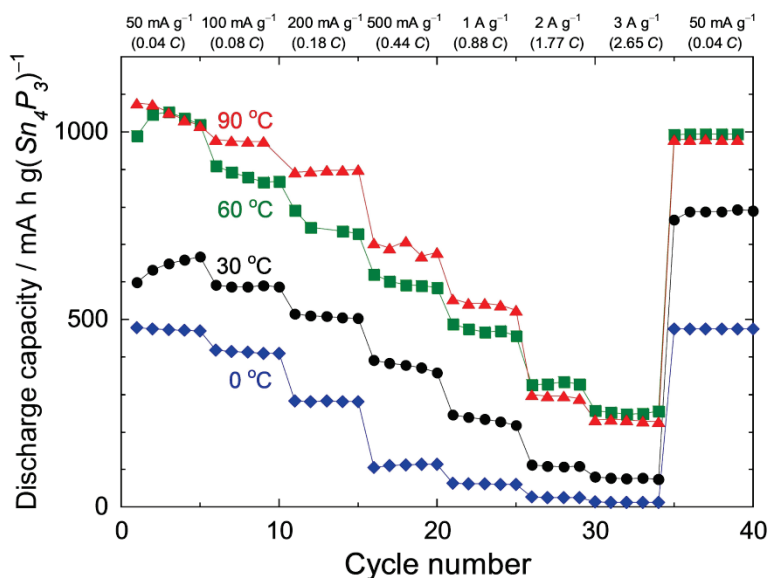

Figure 5-11. Rate performances of Sn$_4$P$_3$ electrode in NaFSA/Py13-FSA at various temperatures.

5.4 Summary

The author investigated charge−discharge performances of Sn$_4$P$_3$ anodes in an ionic liquid electrolyte of NaFSA/Py13-FSA at intermediate temperatures of 60 and 90 ^{o}C. The electrode showed extra capacities based on the full sodiation of Sn in a potential range below 0.2 V vs. Na$^+$/Na at 60 and 90 ^{o}C because its slow kinetics could be improved by elevating operation temperature from 30 ^{o}C. Under the charge−discharge current density of 0.1 A g^{-1} (0.08 *C*), the Sn$_4$P$_3$ electrode at 60 ^{o}C exhibited a large capacity of 870 mA h g^{-1} at the 60th cycle and high Coulombic efficiencies above 99% after the 5th cycle. On the other hand, the

89

degradation of efficiency was observed at 90 ^{o}C. The reason is probably the electrolyte decomposition owing to too high temperature. Even at 3 A g^{-1} (2.65 C), a large capacity of 250 mA h g^{-1} was attained at 60 ^{o}C. From the above results, it was confirmed that the Sn$_4$P$_3$ electrode exhibited remarkable NIBs anode performances with large capacities, high Coulombic efficiencies, and better rate capabilities in the ionic liquid electrolyte at the intermediate temperature range of about 60 ^{o}C.

Chapter 6

Improved Rate Capability of Sn_4P_3 Anode for NIBs in Ether-Substituted Ionic Liquid Electrolyte

6.1 Introduction

In chapter 5, the author demonstrated that the operation at intermediate temperature can significantly improve the electrochemical performance of the Sn_4P_3 anode for NIBs by using the FSA-based ionic liquid electrolyte. On the other hand, the batteries which operate at room temperature have still acted an important role for current society. In this chapter, the author tried to enhance the electrochemical performance of the Sn_4P_3 anode for NIBs at room temperature by fabricating the electrode–electrolyte interface which can realize smooth Na^+ transport.

The electrolyte is one of the most important components determining the cycle life and safety of batteries. The safety requirements increase with the energy density of the batteries. Thus, non-flammable ionic liquids are a promising alternative to conventional organic electrolytes.[143] Li *et al*. applied an ionic liquid electrolyte of sodium bis(fluorosulfonyl)amide (NaFSA)/1-methyl-1-propylpyrrolidinium bis(fluorosulfonyl)amide (Py13-FSA) to a Sb_2S_3/graphene electrode, and reported a reversible capacity of *ca*. 600 mA h g^{-1} over 100 cycles.[144] They showed also non-flammability of the electrolyte by testing with an electric Bunsen burner.[144] We have also firstly demonstrated that this ionic liquid electrolyte is effective to enhance the safety of NIBs by using a closed-system fire-resistance evaluation.[92,93] Moreover, the Sn_4P_3 electrode was found to exhibit superior performance in NaFSA/Py13-FSA than in a conventional carbonate-based electrolyte.[128,129]

In general, since Na^+ is coordinated by solvent molecules in the electrolyte, it inserts in the negative-electrode material via a desolvation process during charging. The charge density of Na^+ is smaller than that of Li^+, resulting in an easier desolvation process for Na^+. Nonetheless, the strong electrostatic interaction of Na^+ with FSA^- in the ionic liquid electrolyte hinders the Na^+ transport, not only at the electrode–electrolyte interface but also in the electrolyte bulk. In the case of Li-ion batteries (LIBs), we have demonstrated that the capacity of Si-based electrodes is significantly promoted by introducing an ether group, e.g., methoxyethoxymethyl (MEM), in the side-chain of the ionic liquid cation.[38] The local negative charge of oxygen atom in ether group weakens the interaction between the Li^+ and bis(trifluoromethanesulfonyl)amide (TFSA) ions, enabling smooth Li^+ transport at the electrode–electrolyte interface. Therefore, we envisioned that the introduction of an ether group in the cation side-chain would enhance the electrochemical performance in NIBs as well. However, MEM is a relatively long chain, which results in higher viscosity and lower conductivity.[145] In this study, we tried to achieve smooth Na^+ transport at the electrode–electrolyte interface, as well as in the electrolyte bulk, by introducing an oxygen atom in the Py13 cation with a shorter side-chain compared to that of the 1-((2-methoxyethoxy)methyl)-1-methylpyrrolidinium (Py1MEM) cation.

6.2 Experimental Details

Figure 6-1 shows the cation and anion structures of the ionic liquids used in this study. Two ionic liquids were synthesized by a previously reported organic method:[146] 1-methoxymethyl-1-methylpyrrolidinium bis(fluorosulfonyl)amide (Py1MOM-FSA) and 1-((2-methoxyethocy)methyl)-1-methylpyrrolidinium bis(fluorosulfonyl)amide (Py1MEM-FSA). Py13-FSA was purchased from Kanto Chemical Co., Inc., and used

without further purification. The author confirmed the water content of the ionic liquids to be <50 ppm on a Karl-Fisher moisture titrator (Labconco Corporation, FZ-Compact). Ionic liquid electrolytes were prepared by dissolving NaFSA in each ionic liquid with a concentration of 1 mol dm^{-3} (M). The conductivity was evaluated by electrochemical impedance measurements (CompactStat, Ivium Technologies) using a cell equipped with two Pt electrodes under Ar atmosphere at temperatures ranging from 298 to 333 K.
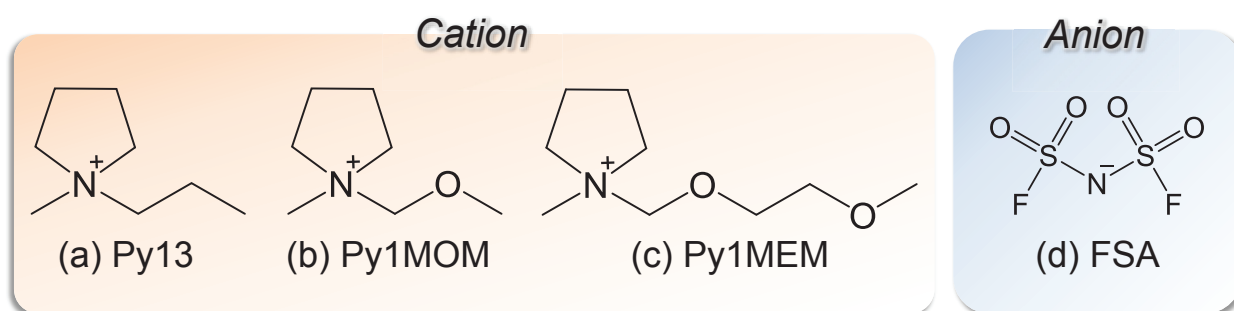

Figure 6-1. Chemical structure of (a) 1-methyl-1-propylpyrrolidinium (Py13), (b) 1-methoxymethyl-1-propylpyrrolidinium (Py1MOM), (c) 1-((2-methoxyethoxy)methyl)-1-propylpyrrolidinium (Py1MEM), and (d) bis(fluorosulfonyl)amide (FSA).

The Sn$_4$P$_3$ active material powder was synthesized by mechanical alloying (MA) using tin powder (99.99%, Rare Metallic) and red phosphorus powder (99.8%, FUJIFILM Wako Pure Chemical Corporation) as the raw materials. The MA treatment was conducted by a Fritsch planetary-type high-energy ball mill (Fritsch Japan Co.,Ltd., Pulverisette P-6) and a stainless steel vessel. The detailed conditions have been described elsewhere.[129] The Sn$_4$P$_3$ powder (70 wt.%) was mixed with acetylene black (15 wt.%), carboxymethyl cellulose (10 wt.%), and styrene-butadiene rubber (5 wt.%). The resulting slurry was uniformly coated on an Al foil with 20 μm thickness. Then, the electrode was punched with holes of $\phi = 1.0$ cm. The mass loading and thickness of the active material layer were approximately 1.2 mg cm^{-2} and 10 μm, respectively. The author assembled a 2032-type coin cell consisting of a Sn$_4$P$_3$

93

working electrode, glass fiber separator, and Na foil counter-electrode. Charge–discharge tests were performed using an electrochemical measurement system (HJ-1001 SD8, Hokuto Denko Co., Ltd.) in the potential range between 0.005 and 2.000 V vs. Na$^+$/Na at 303 K under current densities from 50 to 10000 mA g^{-1} (corresponding to 0.04–8.83 C), since the theoretical capacity of Sn$_4$P$_3$ is 1133 mA h g^{-1}. The interactions between Na$^+$ and FSA$^-$ in ionic liquid electrolytes were analyzed on a Raman microscopy system (NanofinderFLEX, Tokyo Instruments, Inc.) using the 532 nm line of a Nd:YAG laser through a 50-power objective lens at *ca.* 298 K. To avoid the effect of the moisture in air, we placed the electrolyte solution into a quartz cell and tightly sealed it under Ar atmosphere.

6.3 Results and Discussion

Figure 6-2 shows the temperature dependence of the conductivity of the different ionic liquid electrolytes. The conductivities of NaFSA/Py13-FSA, NaFSA/Py1MEM-FSA, and NaFSA/Py1MOM-FSA at 303 K were 5.66, 3.95, and 7.11 mS cm^{-1}, respectively. The NaFSA/Py1MOM-FSA exhibited higher conductivity than NaFSA/Py13-FSA. This is attributed to the electron donation from the methoxy group to the Py1MOM cation center to counter the positive charge.[147] Consequently, the electrostatic interaction between Py1MOM$^+$ and FSA$^-$ is weakened and the conductivity increases. Although Py1MEM-FSA bears a MEM group with electron-donation ability, its conductivity was the lowest of all the ionic liquid electrolytes tested. This is attributed to the long side-chain of the cation.[145] Therefore, both the short side-chain and electron-withdrawing group contribute to the improved conductivity of Py1MOM-FSA.
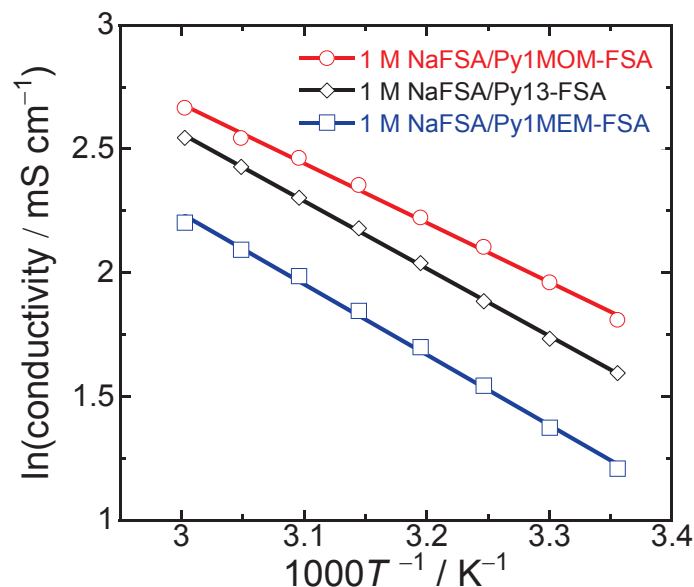
Figure 6-2. Temperature dependence of conductivity of the pyrrolidinium-based ionic-liquid electrolyte solutions.

Higher conductivity of the electrolyte should lead to higher rate capability; thus, the Py1MOM-based electrolyte should be able to improve the rate capability of Sn_4P_3 electrodes. The author performed rate-capability tests for a Sn_4P_3 negative electrode in these ionic liquid electrolytes (Figure 6-3). Discharge capacities of 660 and 240 mA h g^{-1} were obtained in the Py13-based electrolyte at the current densities of 50 and 1000 mA g^{-1}, respectively. Although the conductivity of the Py1MEM-based electrolyte was the lowest, exhibited higher rate capability than in the Py13-based electrolyte: capacities of 850 and 290 mA h g^{-1} were measured at current densities of 50 and 1000 mA g^{-1}, respectively. In the Py1MOM-based electrolyte, the electrode showed the best rate capability, maintaining a discharge capacity of 360 mA h g^{-1} even at 1000 mA g^{-1}, thus surpassing the capacity of hard carbon negative electrodes. By decreasing the current rate to 50 mA g^{-1} at the 51st cycle, the capacities were largely recovered in all the electrolytes. Thus, the capacity fading at high current densities might not be caused by electrode disintegration. As expected, the Py1MOM-based ionic liquid electrolyte enhanced the rate capability of the Sn_4P_3 electrode at current densities up to

2000 mA g^{-1}. However, differences in the performance were observed at current densities over 2000 mA g^{-1}. We have previously confirmed the Sn$_4$P$_3$ electrode exhibits a reversible capacity of *ca.* 250 mA h g^{-1} even at 3000 mA g^{-1} in the Py13-based electrolyte at 333 and 363 K.[148] Thus, the low capacities at high current densities over 2000 mA g^{-1} must be caused by slow Na$^+$ diffusion in the Sn$_4$P$_3$ active material layer. The Py1MEM-based electrolyte was also found to enhance the performance of the electrode compared to the Py13-based electrolyte. It was thus concluded that not only high conductivity is required to improve the rate capability. To clarify the factors enhancing the rate capability, we focused on the charge–discharge behavior of the Sn$_4$P$_3$ electrode in the different electrolytes.
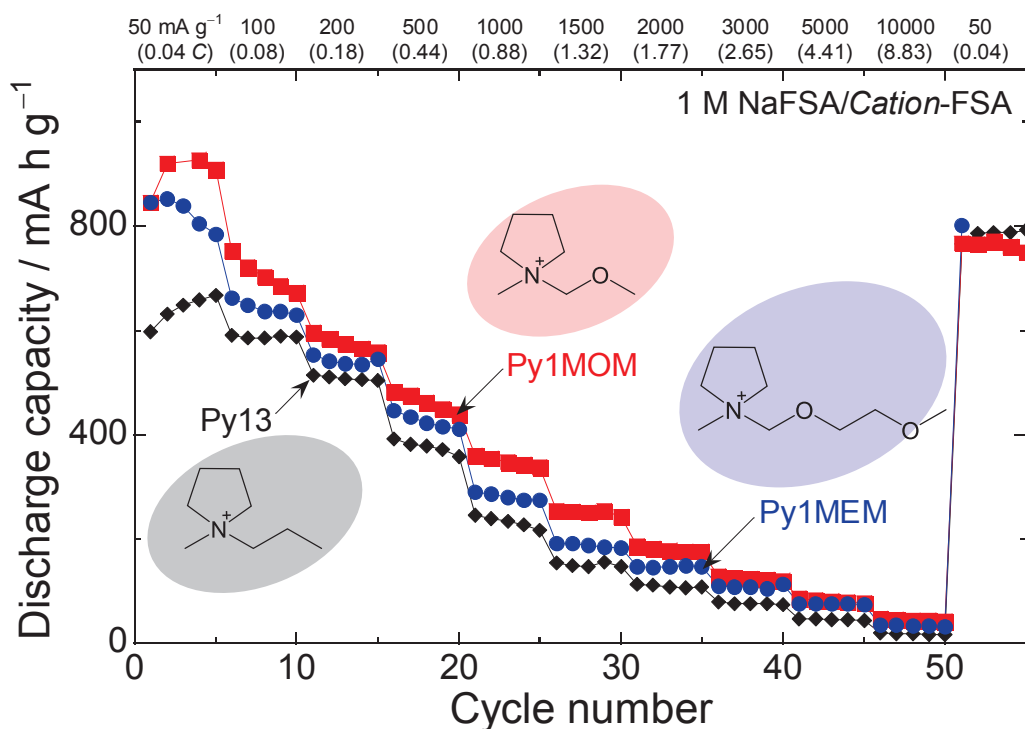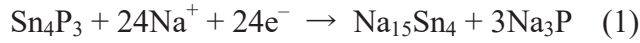

Figure 6-3. Rate capability of Sn$_4$P$_3$ electrodes in 1 M NaFSA-dissolved in Py1MOM-FSA, Py1MEM-FSA, and Py13-FSA.

Qian *et al.* and Kim *et al.* have reported that Sn$_4$P$_3$ phase separation occurs at the first cycle to form elemental Sn and P, and that Sn and P individually react with Na$^+$ in subsequent

cycles.[131,132] We have also confirmed the following reaction mechanism by transmission electron microscopy analysis:[129]

At the first charge (sodiation):

$$Sn_4P_3 + 24Na^+ + 24e^- \rightarrow Na_{15}Sn_4 + 3Na_3P \quad (1)$$

Subsequent cycles:

$$P + 3Na^+ + 3e^- \rightleftarrows 3Na_3P \qquad\qquad (2)$$

$$4Sn + 15Na^+ + 15e^- \rightleftarrows Na_{15}Sn_4 \qquad (3)$$

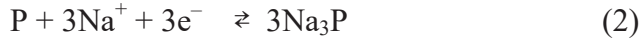Figure 6-4a, c, and e shows the charge–discharge curves of the Sn_4P_3 electrodes in the Py1MOM-, Py1MEM, and Py13-based ionic liquid electrolytes, respectively. In all the electrolytes, potential plateaus are observed at 0.1 V vs. Na^+/Na on the charge curve and at 0.2 V vs. Na^+/Na on the discharge curve at current densities equal to or below 100 mA g^{-1}. These plateaus are ascribed to sodiation–desodiation reactions of Sn. However, they almost disappear at $\geq$200 mA g^{-1} regardless of the electrolyte. This indicates that the slow kinetics of the sodiation reaction for Sn prevents its full sodiation.[149] In contrast, clear charge–discharge potential plateaus are observed at around 0.6 V vs. Na^+/Na corresponding to the reaction of P with Na at current densities up to 500 mA g^{-1}. The reactions of Sn_4P_3 were further evaluated from the differential capacity vs. potential (dQ/dV) profiles (Figure 4b, d, and f). During charging, the peaks at 0.58, 0.16, and 0.005 V vs. Na^+/Na are attributed to the phase transformation reactions P $\rightarrow$ Na_3P_{11}, Na_3P_{11} $\rightarrow$ Na_3P, and Na_xSn $\rightarrow$ $Na_{15}Sn_4$, respectively.[137,141,150] While a clear peak is not observed, the reaction Sn $\rightarrow$ Na_xSn should occur at around 0.08 V vs. Na^+/Na. During discharging (desodiation), four peaks are observed at 0.19, 0.4, 0.62, and 0.9 V vs. Na^+/Na, which are assigned to the reverse reactions, as shown in Figure 6-5. At low current densities of $\leq$100 mA g^{-1}, the peak intensity at 0.005 V vs. Na^+/Na increases following the order: Py1MOM > Py1MEM > Py13. In addition, a peak is observed with the Py1MEM-based electrolyte even at a current density of 200 mA g^{-1}

97

(Figure 6-6). Although it is not distinctly observed in the Py1MOM-based electrolyte, we have confirmed the peak attributed to the reverse reaction at 0.2 V vs. Na$^+$/Na. Thus, the Na$_{15}$Sn$_4$ phase is formed up to 200 mA g^{-1} in the Py1MOM- and Py1MEM-based electrolytes. In regard to the reaction of P with Na$^+$, the peak at 0.62 V vs. Na$^+$/Na (Na$_3$P $\rightarrow$ Na$_3$P$_{11}$) during discharging in the Py1MOM- and Py1MEM-based electrolytes is larger than that for the Py13-based one (Figure 6-7). These results suggest that the sodiation–desodiation reactions of Sn and P are promoted upon introduction of an ether group to the cation side-chain.
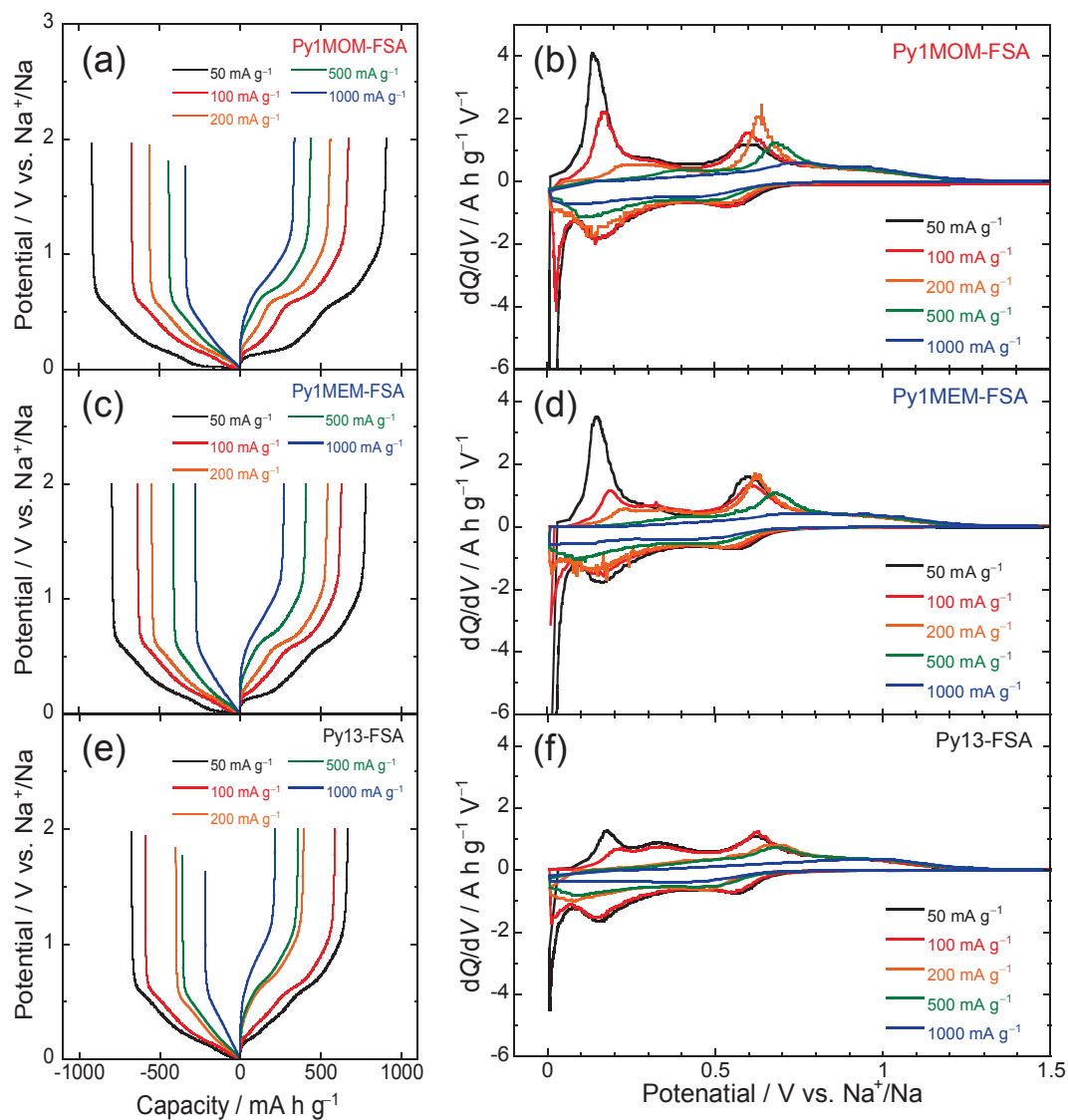

Figure 6-4. (a, c, e) Charge–discharge (Na-insertion/extraction) profiles and (b, d, f) dQ/dV curves of Sn$_4$P$_3$ electrodes in ionic liquid electrolyte of 1 M NaFSA-dissolved (a, b) Py1MOM-FSA, (c, d) Py1MEM-FSA, and (e, f) Py13-FSA under the current density from 50 to 1000 mA g^{-1} at 303 K.
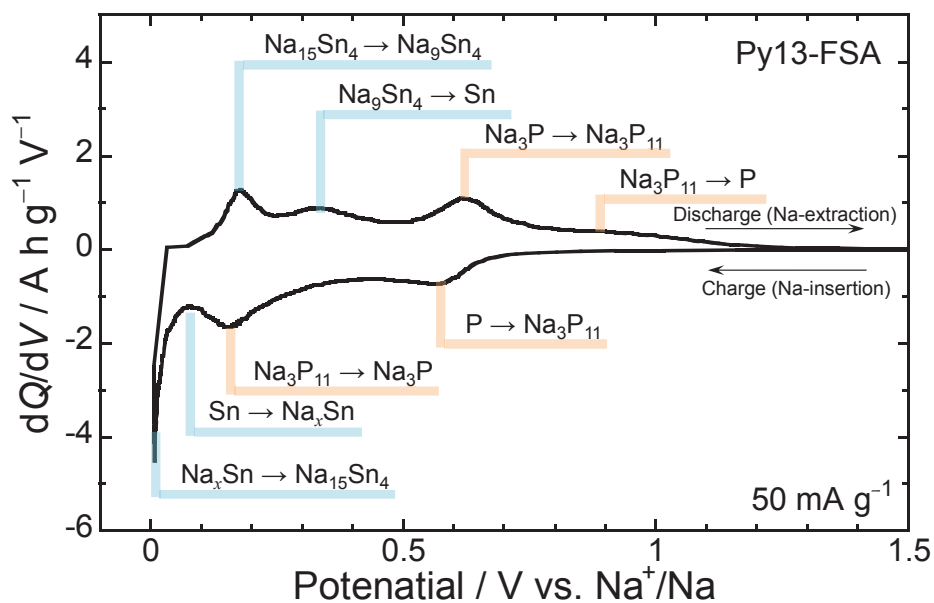
Figure 6-5. Differential capacity (dQ/dV) versus potential profile of Sn$_4$P$_3$ electrode in 1 M NaFSA/Py13-FSA under current density of 50 mA g^{-1}.

Figure 6-6. Differential capacity (dQ/dV) versus potential profiles of Sn$_4$P$_3$ electrodes in various ionic liquid electrolytesA under current density of 200 mA g^{-1}.
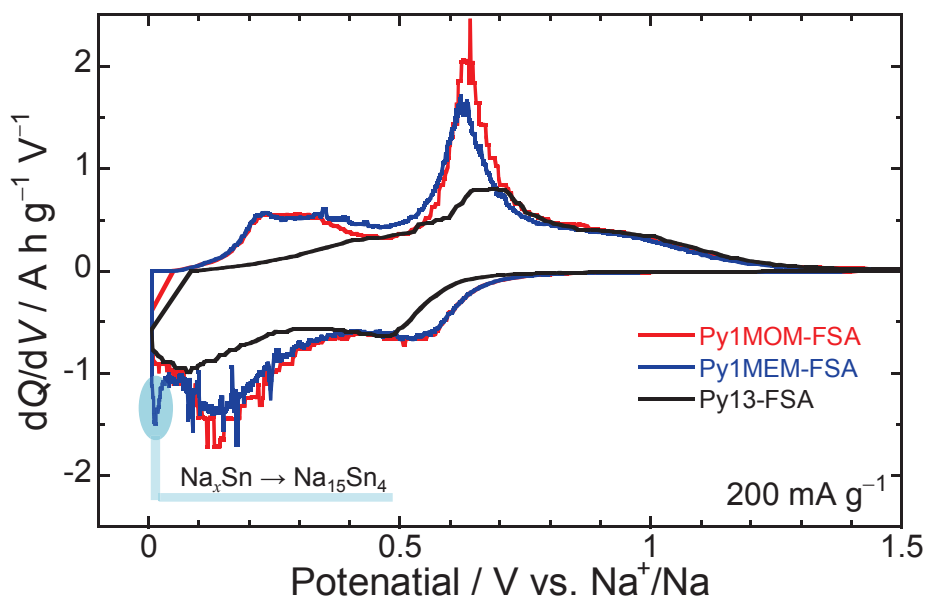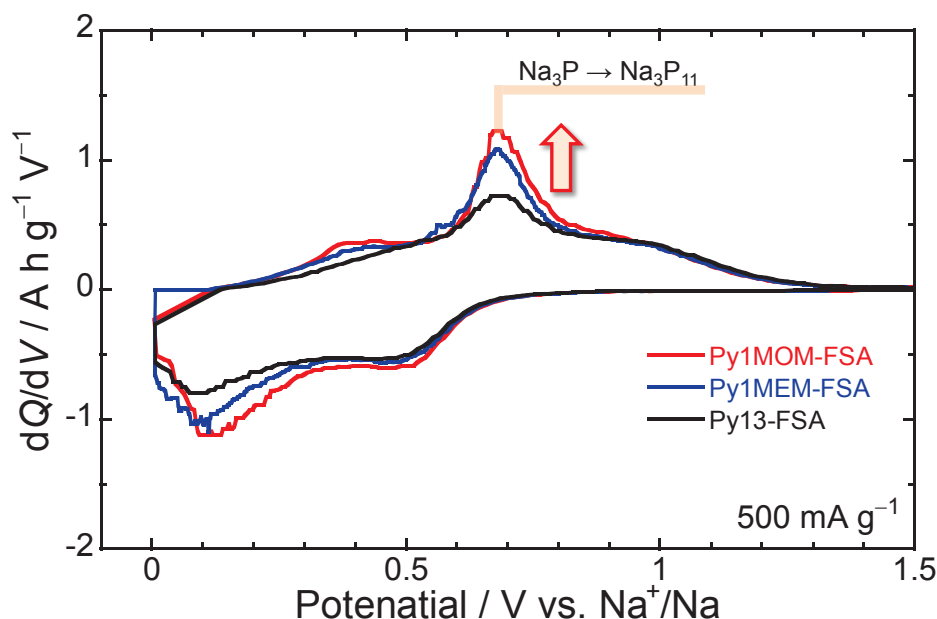
Figure 6-7. Differential capacity (dQ/dV) versus potential profiles of Sn_4P_3 electrodes in various ionic liquid electrolytesA under current density of 500 mA g^{-1}.

We have previously revealed that the electrochemical performance of a Si negative electrode for LIBs can be significantly improved by introducing an ether (MEM) group on the side-chain of the cation in ionic liquids.[38,151] This occurs because the MEM group reduces the electrostatic interactions between Li$^+$ and TFSA$^-$, thus promoting Li$^+$ transport at the electrode–electrolyte interface. In terms of NIBs, we assumed that the introduction of an ether group would also reduce the interaction between Na$^+$ and FSA$^-$, contributing to a higher rate capability. To analyze the solvation number of FSA$^-$ per Na$^+$ cation, we prepared ionic liquid electrolytes with various concentrations of NaFSA, and performed Raman spectroscopy measurements. Figure 6-8 shows the Raman spectra of the ionic liquid electrolytes. The Raman band at ~728 cm^{-1} is attributed to the stretching vibration ν_s(S−N) of FSA$^-$.[152] The band indicates the presence of FSA$^-$ not interacting with Na$^+$ (free FSA$^-$). An additional shoulder is observed at ~745 cm^{-1} with the increasing molar fraction of Na (Figure 6-9). Carstens *et al*. have reported that such a new band at ~743 cm^{-1} corresponds to the interaction between Na$^+$ and FSA$^-$ (Na$^+$-FSA$^-$).[152] The solvation number was determined

from said Raman band in the wavenumber range of 650–800 cm^{-1}. All Raman bands were deconvoluted into two components, those of free FSA^- and Na^+-FSA^-, using a Gaussian function, as shown in Figure 6-10a-c. The band intensity of Na^+-FSA^- ($I_{Na^+-FSA^-}$) in the Py1MEM-based electrolyte is significantly low, indicating that the MEM group reduces the electrostatic interactions between Na^+ and FSA^-. Plots of $I_{Na^+-FSA^-}/(I_{free\ FSA^-} + I_{Na^+-FSA^-})$ as a function of the molar fraction (x) of NaFSA for the different electrolyte solutions afforded a straight line (Figure 6-11). This slope corresponds to the average solvation number of FSA^- per Na^+.[153,154] The average solvation number was calculated as 2.54 for the Py13-based electrolyte and 2.40 for the Py1MOM-based electrolyte. It has been reported that the solvation number of FSA^- per Na^+ is 2.7 in the electrolyte consisting of 1-butyl-1-methylpyrrolidinium (Py14)-FSA.[152] It is suggested that both $[Na(FSA)_3]^{2-}$ and $[Na(FSA)_2]^-$ complexes exist in the electrolytes. Kunze *et al.* have reported that the solvation number of $TFSA^-$ per Li^+ in a Py13-based electrolyte was smaller than that in a Py14-based electrolyte.[155] This is caused by aggregation of the Py14 cations due to the stronger hydrophobic interactions between the long alkyl chains.[155] Thus, the solvation number in the Py13-based electrolyte is smaller than 2.7 in this study. The solvation number in the Py1MOM-based electrolyte is equal to or slightly lower than that for the Py13-based one. This might be because the oxygen atom in the MOM group acts repulsively against FSA^- minimizing the interaction between Na^+ and FSA^-. On the other hand, the solvation number was determined as 1.63 for the Py1MEM-based electrolyte, the lowest value of all the electrolytes. It is considered that the Py1MEM cation favors the Na^+ binding with FSA^- through the two oxygen atoms in its ether side-chain to form a Py1MEM–NaFSA complex, as is the case with the PP1MEM–LiTFSA complex we have previously reported.[151] Therefore, the average solvation number of FSA^- in the Py1MEM-based electrolyte is lower than that for the other electrolytes. A lower solvation number should contribute to improve the rate

capability. However, the Sn_4P_3 electrode exhibits higher rate capability in the Py1MOM-based electrolyte than in the Py1MEM-based one. In addition, the reaction of Na^+ with Sn or P is promoted in the Py1MOM-based electrolyte compared to the Py13-based one, as shown in Figures 6-3 and 6-4. From these results, as expected, the introduction of an ether moiety in the short side-chains of the Py13 cation is a promising approach for NIBs to enhance the rate capability. If both reduced solvation number and improved conductivity can be realized, the rate capability may be further improved.
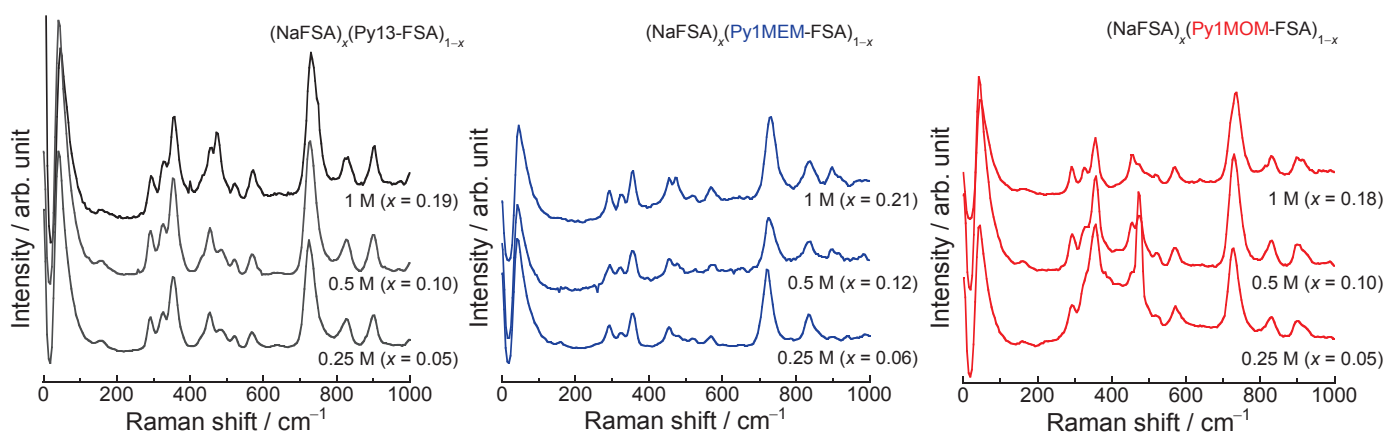

Figure 6-8. Raman spectra of (a) Py13-FSA, (b) Py1MEM-FSA, and (c) Py1MOM-FSA dissolved NaFSA with various concentration of 0.25, 0.5, and 1.0 M in the wavenumber range from 0 to 1000 cm^{-1}.
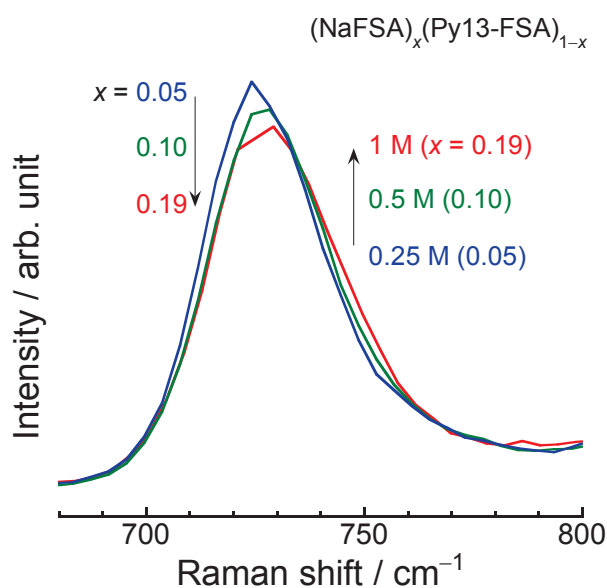

Figure 6-9. Raman spectrum of $(NaFSA)_x(Py13\text{-}FSA)_{1-x}$, ($x = 0.05, 0.10, 0.19$) in the wavenumber range from 650 to 800 cm^{-1}.
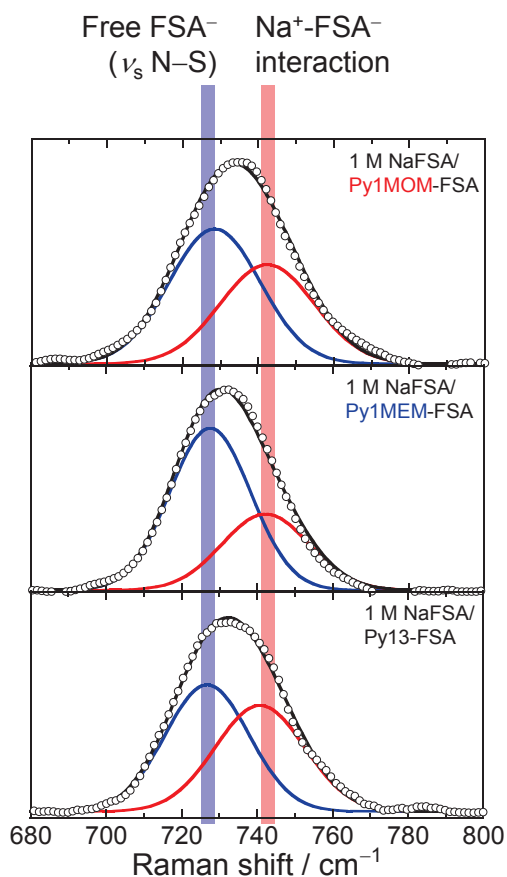
Figure 6-10. Deconvoluted Raman bands of 1 M NaFSA-dissolved in (a) Py1MOM-FSA, (b) Py1MEM-FSA, and (c) Py13-FSA. The dotted, black, blue, and red lines show the observed spectrum, the total Raman spectrum, the deconvoluted components of free FSA anion and coordinated FSA anion (Na$^+$-FSA$^-$), respectively.
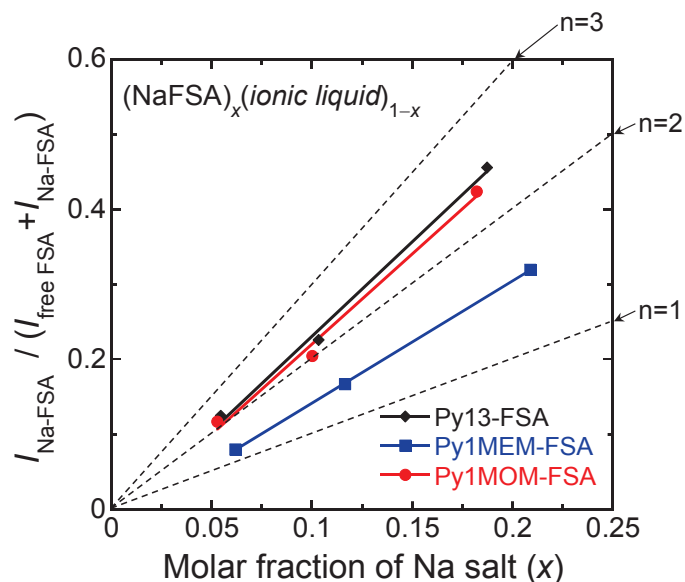
Figure 6-11. Plot of $I_{Na^+-FSA^-}/(I_{free\ FSA^-} + I_{Na^+-FSA^-})$ as a function of x for (NaFSA)$_x$(Py13-FSA)$_{1-x}$, (NaFSA)$_x$(Py1MEM-FSA)$_{1-x}$, (NaFSA)$_x$(Py1MOM-FSA)$_{1-x}$. The dotted lines show slopes in cases for which the average solvation numbers (n) of FSA anions per Na ion are one, two, and three.

6.4 Summary

The author has investigated the effect of the cation structure in ionic liquids on the electrochemical performance of the Sn_4P_3 negative electrode for NIBs. Ether-substituted ionic liquid electrolytes NaFSA/Py1MOM-FSA and NaFSA/Py1MEM-FSA successfully enhanced the rate capability of the electrode. The electrochemical reaction of Na^+ and Sn/P was promoted in these electrolytes compared to the Py13-based electrolyte without ether moieties, further contributing to a higher capacity. Introduction of an ether group in the side-chain of the ionic liquid cation reduces the electrostatic interactions between Na^+ and FSA^- in the electrolyte; as a result, the solvation number of FSA^- per Na^+ is reduced, especially in the Py1MEM-based electrolyte. While the solvation number in the Py1MOM-based electrolyte was found to be greater than in the Py1MEM-based one, its conductivity was significantly higher, leading to better rate capability. Therefore, the introduction of an ether group in the short side-chains of the Py13 cation is a better approach to improve the conductivity and enhance the rate capability of the Sn_4P_3 electrode.

Concluding Remarks

In this thesis, the author tried to fabricate the electrode–electrolyte interface which can enhance an electrochemical property of anode for alkali-metal-ion rechargeable batteries by modifying cation and anion structure of ionic liquids. Main results of this work are as follows:

1.   A Si-alone electrode was prepared by a gas-deposition method. Electrochemical reactions of the Si electrodes in three types of ionic liquid electrolytes (PP1MEM-FSA, PP1MEM-TFSA, and PP1MEM-BF$_4$) were investigated without commercially used conductive additive or binder. The BF$_4$-derived surface films cannot be electrical insulating, whereas the TFSA- and FSA-derived ones have good insulation property. This property leads to the suppression of the additional reductive decomposition of the electrolyte. Si electrode in the FSA-based electrolyte exhibited the best cycle performance with the discharge capacity of 2000 mA h g^{-1} after 100 cycles.

2.   Effect of anion structure in ionic liquids on the electrochemical performance of annealed Ni–P/(etched Si) electrode was studied. It was revealed that the replacement of TFSA anion to FSA anion can reduce the cell resistances and promote Li-insertion into Si. Therefore, increase in Li-insertion/extraction capacities and improvement of cycling stability of annealed Ni–P/(etched Si) were simultaneously achieved. In addition, rate capability of annealed Ni–P/(etched Si) electrode was also enhanced because of lower cell resistances in the FSA-based electrolyte.

3.   Reaction behavior of the Si-alone electrode in the FSA-based ionic liquid electrolyte was investigated by SXES measurement with FE-SEM observation. By determining the position of Li in Si active material layer with SXES, it was found that Li-insertion distribution inside Si electrode cycled in the FSA-based electrolyte was more homogeneous compared with that in a conventional organic electrolyte. Li-extraction distribution at the electrode surface was also uniform in the FSA-based electrolyte. The homogeneous Li-insertion/extraction distribution enables Si electrode to alleviate the stresses and avoid the accumulation of strains, leading to better cycling stability.

4.   Influence of film-forming additives in EMI-based ionic liquid electrolytes on charge–discharge performance of Si-alone anode for LIBs was studied. VC addition successfully suppressed the reductive decomposition of EMI cation to enable lithiation-delithiation reactions of Si. The rate performance of the Si electrode in the VC-added EMI-based electrolyte was significantly improved owing to the high conductivity of the EMI-based electrolyte. In addition, a non-flammability of the electrolyte was demonstrated even in the VC-added system. Thus, the VC-added EMI-based electrolyte can improve not only the electrochemical performance of the Si anode but also safety of batteries.

5.   Electrochemical performance of the Sn_4P_3 electrode for NIBs was evaluated in the FSA-based ionic liquid electrolyte at intermediate temperature. The Sn_4P_3 electrode at 60 and 90 ^{o}C exhibited not only a higher discharge capacity but also a better cycle performance and rate capability than that at 30 ^{o}C. Charge transfer resistance of the cell clearly decreased at 60 ^{o}C. In addition, Coulombic efficiency at 60 ^{o}C was better compared to that at 90 ^{o}C. Therefore, it was confirmed that the ionic liquid electrolyte at the intermediate temperature range of about 60 ^{o}C can remarkably enhance the NIBs anode performance of Sn_4P_3 electrode.

6.   Applicability of the ether-substituted ionic liquid (Py1MEM-FSA and Py1MOM-FSA) electrolytes to the Sn_4P_3 electrode was evaluated to enhance its rate capability. Although the Py1MEM cation with two ether oxygen atoms has a longer side chain length compared to the Py13 cation, the Py1MEM-based electrolyte enhanced the rate capability of the Sn_4P_3 electrode. The electrostatic interaction between Na^+ and FSA^- was weakened in the electrolyte, which should contribute to higher rate capability. Meanwhile, the best rate capability was obtained in the ionic liquid electrolyte consisted of Py1MOM cation with one ether oxygen atom and same side chain length of Py13 cation. This is because the Py1MOM-based electrolyte has higher conductivity than the Py13-based electrolyte. Consequently, it is revealed that introduction of ether-group into ionic liquid cation with short side chain length is effective approach to enhance rate capability of the Sn_4P_3 electrode for NIBs.

Acknowledgments

References

[1]   C.J. Wen, R.A. Huggins, *J. Solid State Chem.* **37** (1981) 271–278.

[2]   B. Key, R. Bhattacharyya, M. Morcrette, V. Seznec, J.M. Tarascon, C.P. Grey, *J. Am. Chem. Soc.* **131** (2009) 9239–9249.

[3]   W. Wang, P.N. Kumta, *ACS Nano*. **4** (2011) 2233–2241.

[4]   X.H. Liu, L. Zhong, S. Huang, S.X. Mao, T. Zhu, J.Y. Huang, *ACS Nano*. **6** (2012) 1522–1531.

[5]   N. Ding, J. Xu, Y.X. Yao, G. Wegner, X. Fang, C.H. Chen, I. Lieberwirth, *Solid State Ionics*. **180** (2009) 222–225.

[6]   J. Xie, N. Imanishi, T. Zhang, A. Hirano, Y. Takeda, O. Yamamoto, N. Ding, J. Xu, Y.X. Yao, G. Wegner, X. Fang, C.H. Chen, I. Lieberwirth, *Mater. Chem. Phys.* **120** (2010) 421–425.

[7]   M. Galiński, A. Lewandowski, I. Stepniak, *Electrochim. Acta*. **51** (2006) 5567–5580.

[8]   V.I. Pârvulescu, C. Hardacre, *Chem. Rev.* (2007) 2615–2665.

[9]   N. V. Plechkova, K.R. Seddon, *Chem. Soc. Rev.* **37** (2008) 123–150.

[10] P. Hapiot, C. Lagrost, *Chem. Rev.* **108** (2008) 2238–2264.

[11] S. Kuwabata, T. Tsuda, T. Torimoto, *J. Phys. Chem. Lett.* **1** (2010) 3177–3188.

[12] T. Torimoto, T. Tsuda, K.I. Okazaki, S. Kuwabata, *Adv. Mater.* **22** (2010) 1196–1221.

[13] M. Zhen, J. Yu, S. Dai, *Adv. Mater.* **22** (2010) 261–285.

[14] H. Wang, G. Gurau, R.D. Rogers, *Chem. Soc. Rev.* **41** (2012) 1519.

[15] X. Sun, H. Luo, S. Dai, *Chem. Rev.* **112** (2012) 2100–2128.

[16] M. Armand, F. Endres, D.R. MacFarlane, H. Ohno, B. Scrosati, *Nat. Mater.* **8** (2009) 621–629.

[17] D.M. Piper, T. Evans, K. Leung, T. Watkins, J. Olson, S.C. Kim, S.S. Han, V. Bhat, K.H. Oh, D.A. Buttry, S.-H. Lee, *Nat. Commun.* **6** (2015) 1–10.

109

[18] H. Matsumoto, H. Sakaebe, K. Tatsumi, *J. Power Sources*. **146** (2005) 45–50.

[19] H. Matsumoto, H. Sakaebe, K. Tatsumi, M. Kikuta, E. Ishiko, M. Kono, *J. Power Sources*. **160** (2006) 1308–1313.

[20] S. Tsuzuki, W. Shinoda, M. Matsugami, Y. Umebayashi, K. Ueno, T. Mandai, S. Seki, K. Dokko, M. Watanabe, *Phys. Chem. Chem. Phys.* **17** (2015) 126–129.

[21] K. Yoshida, M. Nakamura, Y. Kazue, N. Tachikawa, S. Tsuzuki, S. Seki, K. Dokko, M. Watanabe, *J. Am. Chem. Soc.* **133** (2011) 13121–13129.

[22] K. Tsunashima, M. Sugiya, *Electrochem. Commun.* **9** (2007) 2353–2358.

[23] S. Komaba, W. Murata, T. Ishikawa, N. Yabuuchi, T. Ozeki, T. Nakayama, A. Ogata, K. Gotoh, K. Fujiwara, *Adv. Funct. Mater.* **21** (2011) 3859–3867.

[24] N. Yabuuchi, K. Kubota, M. Dahbi, S. Komaba, *Chem. Rev.* **114** (2014) 11636–11682.

[25] D.A. Stevens, J.R. Dahn, *J. Electrochem. Soc.* **147** (2000) 1271.

[26] A. Ponrouch, A.R. Goñi, M.R. Palacín, *Electrochem. Commun.* **27** (2013) 85–88.

[27] M. Egashira, T. Tanaka, N. Yoshimoto, M. Morita, *Electrochemistry*. **80** (2012) 755–758.

[28] G. Hasegawa, K. Kanamori, N. Kannari, J. Ozaki, K. Nakanishi, T. Abe, *J. Power Sources*. **318** (2016) 41–48.

[29] S.-C. Lai, *J. Electrochem. Soc.* **123** (1976) 1196–1197.

[30] M.N. Obrovac, L. Christensen, *Electrochem. Solid-State Lett.* **7** (2004) A93–A96.

[31] T.D. Hatchard, J.R. Dahn, *J. Electrochem. Soc.* **151** (2004) A838–A842.

[32] M.N. Obrovac, L.J. Krause, *J. Electrochem. Soc.* **154** (2007) A103.

[33] M.K. Datta, P.N. Kumta, *J. Power Sources*. **194** (2009) 1043–1052.

[34] T. Zhang, J. Gao, L.J. Fu, L.C. Yang, Y.P. Wu, H.Q. Wu, *J. Mater. Chem.* **17** (2007) 1321–1325.

[35] T. Zhang, L.J. Fu, H. Takeuchi, J. Suzuki, K. Sekine, T. Takamura, Y.P. Wu, *J. Power Sources*. **159** (2006) 349–352.

[36] H. Usui, M. Shimizu, H. Sakaguchi, *J. Power Sources*. **235** (2013) 29–35.

[37] H. Usui, T. Masuda, H. Sakaguchi, *Chem. Lett.* **41** (2012) 521–522.

[38] M. Shimizu, H. Usui, K. Matsumoto, T. Nokami, T. Itoh, H. Sakaguchi, *J. Electrochem. Soc.* **161** (2014) A1765–A1771.

[39] K. Hayamizu, S. Tsuzuki, S. Seki, *J. Chem. Eng. Data*. **59** (2014) 1944–1954.

[40] K. Hayamizu, S. Tsuzuki, S. Seki, K. Fujii, M. Suenaga, Y. Umebayashi, *J. Chem. Phys.* **133** (2010) 194505.

[41] H. Matsumoto, H. Sakaebe, K. Tatsumi, *ECS Trans.* **16** (2009) 59–66.

[42] Y. Umebayashi, T. Mitsugi, S. Fukuda, T. Fujimori, K. Fujii, R. Kanzaki, M. Takeuchi, S.-I.I. Ishiguro, *J. Phys. Chem. B*. **111** (2007) 13028–13032.

[43] Y. Umebayashi, S. Mori, K. Fujii, S. Tsuzuki, S. Seki, K. Hayamizu, S.I. Ishiguro, *J. Phys. Chem. B*. **114** (2010) 6513–6521.

[44] K. Fujii, H. Hamano, H. Doi, X. Song, S. Tsuzuki, K. Hayamizu, S. Seki, Y. Kameda, K. Dokko, M. Watanabe, Y. Umebayashi, *J. Phys. Chem. C*. **117** (2013) 19314–19324.

[45] T. Sugimoto, Y. Atsumi, M. Kikuta, E. Ishiko, M. Kono, M. Ishikawa, *J. Power Sources*. **189** (2009) 802–805.

[46] T. Sugimoto, M. Kikuta, E. Ishiko, M. Kono, M. Ishikawa, *J. Power Sources*. **183** (2008) 436–440.

[47] M. Yamagata, N. Nishigaki, S. Nishishita, Y. Matsui, T. Sugimoto, M. Kikuta, T. Higashizaki, M. Kono, M. Ishikawa, *Electrochim. Acta*. **110** (2013) 181–190.

[48] H. Sakaguchi, T. Toda, Y. Nagao, T. Esaka, *Electrochem. Solid-State Lett.* **10** (2007) J146–J149.

111

[49] C. Liu, X. Ma, F. Xu, L. Zheng, H. Zhang, W. Feng, X. Huang, M. Armand, J. Nie, H. Chen, Z. Zhou, *Electrochim. Acta*. **149** (2014) 370–385.

[50] S. Fang, L. Yang, J. Wang, H. Zhang, K. Tachibana, K. Kamijima, *J. Power Sources*. **191** (2009) 619–622.

[51] P. Johansson, *Phys. Chem. Chem. Phys.* **9** (2007) 1493–1498.

[52] P.C. Howlett, E.I. Izgorodina, M. Forsyth, D.R. MacFarlane, *Zeitschrift Für Phys. Chemie*. **220** (2006) 1483–1498.

[53] E. Markevich, R. Sharabi, V. Borgel, H. Gottlieb, G. Salitra, D. Aurbach, G. Semrau, M.A. Schmidt, *Electrochim. Acta*. **55** (2010) 2687–2696.

[54] S. Xiong, K. Xie, E. Blomberg, P. Jacobsson, A. Matic, *J. Power Sources*. **252** (2014) 150–155.

[55] A. Budi, A. Basile, G. Opletal, A.F. Hollenkamp, A.S. Best, R.J. Rees, A.I. Bhatt, A.P. O'Mullane, S.P. Russo, P.F. Imide, A.P.O. Mullane, *J. Phys. Chem. C*. **116** (2012) 19789–19797.

[56] K.W. Schroder, J. Alvarado, T.A. Yersak, J. Li, N. Dudney, L.J. Webb, Y.S. Meng, K.J. Stevenson, *Chem. Mater.* **27** (2015) 5531–5542.

[57] M. Shimizu, H. Usui, T. Suzumura, H. Sakaguchi, *J. Phys. Chem. C*. **119** (2015) 2975–2982.

[58] S. Tsuzuki, K. Hayamizu, S. Seki, *J. Phys. Chem. B*. **114** (2010) 16329–16336.

[59] Y. Yamada, Y. Iriyama, T. Abe, Z. Ogumi, *J. Electrochem. Soc.* **157** (2010) A26.

[60] H. Usui, K. Meabara, K. Nakai, H. Sakaguchi, *Int. J. Electrochem. Sci.* **6** (2011) 2246–2254.

[61] Y. Domi, H. Usui, Y. Takemoto, K. Yamaguchi, H. Sakaguchi, *Chem. Lett.* **45** (2016) 1198–1200.

[62] H. Usui, N. Uchida, H. Sakaguchi, *Electrochemistry*. **80** (2012) 737–739.

[63] Y. Domi, H. Usui, M. Narita, Y. Fujita, K. Yamaguchi, H. Sakaguchi, *J. Electrochem. Soc.* **164** (2017) A3208–A3213.

[64] H. Usui, K. Wasada, M. Shimizu, H. Sakaguchi, *Electrochim. Acta.* **111** (2013) 575–580.

[65] K. Ababtain, G. Babu, X. Lin, M.T.F. Rodrigues, H. Gullapalli, P.M. Ajayan, M.W. Grinstaff, L.M.R. Arava, *ACS Appl. Mater. Interfaces.* **8** (2016) 15242–15249.

[66] S.H. Baek, J.S. Park, Y.M. Jeong, J.H. Kim, *J. Alloys Compd.* **660** (2016) 387–391.

[67] V. Chakrapani, F. Rusli, M.A. Filler, P.A. Kohl, *J. Phys. Chem. C.* **115** (2011) 22048–22053.

[68] B. Philippe, R. Dedryvère, M. Gorgoi, H. Rensmo, D. Gonbeau, K. Edström, *J. Am. Chem. Soc.* **135** (2013) 9829–9842.

[69] I.A. Shkrob, Y. Zhu, T.W. Marin, D. Abraham, *J. Phys. Chem. C.* **117** (2013) 19255–19269.

[70] V. Etacheri, O. Haik, Y. Goffer, G.A. Roberts, I.C. Stefan, R. Fasching, D. Aurbach, *Langmuir.* **28** (2012) 965–976.

[71] K. Yamaguchi, Y. Domi, H. Usui, M. Shimizu, K. Matsumoto, T. Nokami, T. Itoh, H. Sakaguchi, *J. Power Sources.* **338** (2017) 103–107.

[72] K. Yamaguchi, Y. Domi, H. Usui, H. Sakaguchi, *ChemElectroChem.* **4** (2017) 3257–3263.

[73] C.Y. Chen, T. Sano, T. Tsuda, K. Ui, Y. Oshima, M. Yamagata, M. Ishikawa, M. Haruta, T. Doi, M. Inaba, S. Kuwabata, *Sci. Rep.* **6** (2016) 1–3.

[74] C.C. Nguyen, S.W. Woo, S.W. Song, *J. Phys. Chem. C.* **116** (2012) 14764–14771.

[75] T. Sugimoto, Y. Atsumi, M. Kono, M. Kikuta, E. Ishiko, M. Yamagata, M. Ishikawa, *J. Power Sources.* **195** (2010) 6153–6156.

[76] T. Wermelinger, R. Spolenak, *J. Raman Spectrosc.* **40** (2009) 679–686.

113

[77] A.M. Yaremko, V.O. Yukhymchuk, S.S. Ponomaryov, V. V. Koroteev, V.M. Dzhagan, Y.A. Romanyuk, J. Baran, *Solid State Commun.* **195** (2014) 39–42.

[78] S. Murugesan, J.T. Harris, B. a Korgel, K.J. Stevenson, *Chem. Mater.* **24** (2012) 1306–1315.

[79] M. Nie, D.P. Abraham, Y. Chen, A. Bose, B.L. Lucht, *J. Phys. Chem. C.* **117** (2013) 13403–13412.

[80] A. Tokranov, B.W. Sheldon, C. Li, S. Minne, X. Xiao, *ACS Appl. Mater. Interfaces.* **6** (2014) 6672–6686.

[81] Y. Domi, H. Usui, M. Shimizu, Y. Kakimoto, H. Sakaguchi, *ACS Appl. Mater. Interfaces.* **8** (2016) 7125–7132.

[82] T. Jaumann, J. Balach, M. Klose, S. Oswald, U. Langklotz, A. Michaelis, J. Eckert, L. Giebeler, *Phys. Chem. Chem. Phys.* **17** (2015) 24956–24967.

[83] J.R. Szczech, S. Jin, *Energy Environ. Sci.* **4** (2011) 56–72.

[84] M. Terauchi, H. Takahashi, N. Handa, T. Murano, M. Koike, T. Kawachi, T. Imazono, M. Koeda, T. Nagano, H. Sasai, Y. Oue, Z. Yonezawa, S. Kuramoto, *J. Electron Microsc. (Tokyo).* **61** (2012) 1–8.

[85] A.A. Miran Beigi, M. Abdouss, M. Yousefi, S.M. Pourmortazavi, A. Vahid, *J. Mol. Liq.* **177** (2013) 361–368.

[86] S. Hy, Y.H. Chen, H.M. Cheng, C.J. Pan, J.H. Cheng, J. Rick, B.J. Hwang, *ACS Appl. Mater. Interfaces.* **7** (2015) 13801–13807.

[87] S.K. Jeong, M. Inaba, R. Mogi, Y. Iriyama, T. Abe, Z. Ogumi, *Langmuir.* **17** (2001) 8281–8286.

[88] Y. Xiao, D. Hao, H. Chen, Z. Gong, Y. Yang, *ACS Appl. Mater. Interfaces.* **5** (2013) 1681–1687.

[89] D. Aurbach, K. Gamolsky, B. Markovsky, Y. Gofer, M. Schmidt, U. Heider, *Electrochim. Acta*. **47** (2002) 1423–1439.

[90] X.G. Sun, S. Dai, *Electrochim. Acta*. **55** (2010) 4618–4626.

[91] T. Sugimoto, Y. Atsumi, N. Handa, M. Yamagata, M. Kono, M. Kikuta, E. Ishiko, M. Ishikawa, *Electrochemistry*. **77** (2009) 696–698.

[92] M. Shimizu, H. Usui, K. Yamane, T. Sakata, T. Nokami, T. Itoh, H. Sakaguchi, *Int. J. Electrochem. Sci.* **10** (2015) 10132–10144.

[93] H. Usui, Y. Domi, M. Shimizu, A. Imoto, K. Yamaguchi, H. Sakaguchi, *J. Power Sources*. **329** (2016) 428–431.

[94] I.A. Profatilova, C. Stock, A. Schmitz, S. Passerini, M. Winter, *J. Power Sources*. **222** (2013) 140–149.

[95] G.G. Eshetu, T. Diemant, S. Grugeon, R.J. Behm, S. Laruelle, M. Armand, S. Passerini, *ACS Appl. Mater. Interfaces*. **8** (2016) 16087–16100.

[96] G.M.A. Girard, M. Hilder, N. Dupre, D. Guyomard, D. Nucciarone, K. Whitbread, S. Zavorine, M. Moser, M. Forsyth, D.R. MacFarlane, P.C. Howlett, *ACS Appl. Mater. Interfaces*. **10** (2018) 6719–6729.

[97] G.M.A. Girard, M. Hilder, D. Nucciarone, K. Whitbread, S. Zavorine, M. Moser, M. Forsyth, D.R. MacFarlane, P.C. Howlett, *J. Phys. Chem. C*. **121** (2017) 21087–21095.

[98] M. Nie, J. Demeaux, B.T. Young, D.R. Heskett, Y. Chen, A. Bose, J.C. Woicik, B.L. Lucht, *J. Electrochem. Soc.* **162** (2015) A7008–A7014.

[99] A.L. Michan, B.S. Parimalam, M. Leskes, R.N. Kerber, T. Yoon, C.P. Grey, B.L. Lucht, *Chem. Mater.* **28** (2016) 8149–8159.

[100] Y. Jin, N.J.H. Kneusels, L.E. Marbella, E. Castillo-Martínez, P.C.M.M. Magusin, R.S. Weatherup, E. Jónsson, T. Liu, S. Paul, C.P. Grey, *J. Am. Chem. Soc.* **140** (2018) 9854–9867.

115

[101] F. Lindgren, C. Xu, L. Niedzicki, M. Marcinek, T. Gustafsson, F. Björefors, K. Edström, R. Younesi, *ACS Appl. Mater. Interfaces*. **8** (2016) 15758–15766.

[102] Y. Domi, H. Usui, M. Shimizu, K. Miwa, H. Sakaguchi, *Int. J. Electrochem. Sci.* **10** (2015) 9678–9686.

[103] L.J. Hardwick, M. Holzapfel, A. Wokaun, P. Novák, *J. Raman Spectrosc.* **38** (2007) 110–112.

[104] I. Rey, P. Johansson, J. Lindgren, J.C. Lassègues, J. Grondin, L. Servant, *J. Phys. Chem. A*. **102** (1998) 3249–3258.

[105] M. Herstedt, M. Smirnov, P. Johansson, M. Chami, J. Grondin, L. Servant, J.C. Lassègues, *J. Raman Spectrosc.* **36** (2005) 762–770.

[106] J.C. Lassègues, J. Grondin, R. Holomb, P. Johansson, *J. Raman Spectrosc.* **38** (2007) 551–558.

[107] J.R. Durig, J.W. Clark, J.M. Casper, *J. Mol. Struct.* **5** (1970) 67–84.

[108] M. Montanino, M. Moreno, M. Carewska, G. Maresca, E. Simonetti, R. Lo Presti, F. Alessandrini, G.B. Appetecchi, *J. Power Sources*. **269** (2014) 608–615.

[109] H. Nakagawa, Y. Fujino, S. Kozono, Y. Katayama, T. Nukuda, H. Sakaebe, H. Matsumoto, K. Tatsumi, *J. Power Sources*. **174** (2007) 1021–1026.

[110] D. Kundu, E. Talaie, V. Duffort, L.F. Nazar, *Angew. Chem. Int. Ed.* **54** (2015) 3432–3448.

[111] H. Kim, J. Hong, G. Yoon, H. Kim, K.-Y. Park, M.-S. Park, W.-S. Yoon, K. Kang, *Energy Environ. Sci.* (2015).

[112] P. Ge, M. Fouletier, *Solid State Ionics*. **28** (1988) 1172–1175.

[113] R. Alcantara, P. Lavela, G.F. Ortiz, J.M. Jimenez-mateos, R. Menendez, R. Santamarıa, *Carbon N. Y.* **41** (2003) 3003–3013.

[114] M. Dahbi, T. Nakano, N. Yabuuchi, T. Ishikawa, K. Kubota, M. Fukunishi, S. Shibahara, J.Y. Son, Y.T. Cui, H. Oji, S. Komaba, *Electrochem. Commun.* **44** (2014) 66–69.

[115] M. Dahbi, M. Kiso, K. Kubota, T. Horiba, T. Chafik, K. Hida, T. Matsuyama, S. Komaba, *J. Mater. Chem. A*. **5** (2017) 9917–9928.

[116] P. Senguttuvan, G. Rousse, V. Seznec, J.M. Tarascon, M.R. Palacín, *Chem. Mater.* **23** (2011) 4109–4111.

[117] A. Rudola, K. Saravanan, S. Devaraj, H. Gong, P. Balaya, *Chem. Commun.* **49** (2013) 7451.

[118] T. Yamamoto, T. Nohira, R. Hagiwara, A. Fukunaga, S. Sakai, K. Nitta, S. Inazawa, *Electrochim. Acta*. **135** (2014) 60–67.

[119] T. Yamamoto, T. Nohira, R. Hagiwara, A. Fukunaga, S. Sakai, K. Nitta, *Electrochim. Acta*. **193** (2016) 275–283.

[120] T. Yamamoto, T. Nohira, R. Hagiwara, A. Fukunaga, S. Sakai, K. Nitta, *Electrochim. Acta*. **211** (2016) 234–244.

[121] L.O. Vogt, C. Villevieille, *J. Mater. Chem. A*. **4** (2016) 19116–19122.

[122] F. Zhao, N. Han, W. Huang, J. Li, H. Ye, F. Chen, Y. Li, *J. Mater. Chem. A*. **3** (2015) 21754–21759.

[123] H. Usui, S. Yoshioka, K. Wasada, M. Shimizu, H. Sakaguchi, *ACS Appl. Mater. Interfaces*. **7** (2015) 6567–6573.

[124] H. Usui, Y. Domi, S. Yoshioka, K. Kojima, H. Sakaguchi, *ACS Sustainable Chem. Eng.* **4** (2016) 6695–6702.

[125] M. Shimizu, H. Usui, K. Fujiwara, K. Yamane, H. Sakaguchi, *J. Alloys Compd.* **640** (2015) 440–443.

[126] M. Shimizu, H. Usui, H. Sakaguchi, *J. Power Sources*. **248** (2014) 378–382.

117

[127] H. Usui, Y. Domi, S. Ohshima, H. Sakaguchi, *Electrochim. Acta*. **246** (2017) 280–284.

[128] H. Usui, T. Sakata, M. Shimizu, H. Sakaguchi, *Electrochemistry*. **83** (2015) 810–812.

[129] H. Usui, Y. Domi, K. Fujiwara, M. Shimizu, T. Yamamoto, T. Nohira, R. Hagiwara, H. Sakaguchi, *ACS Energy Lett.* **2** (2017) 1139–1143.

[130] H. Usui, Y. Domi, R. Yamagami, K. Fujiwara, H. Nishida, H. Sakaguchi, *ACS Appl. Energy Mater.* **1** (2018) 306–311.

[131] J. Qian, Y. Xiong, Y. Cao, X. Ai, H. Yang, *Nano Lett.* **14** (2014) 1865–1869.

[132] Y. Kim, Y. Kim, A. Choi, S. Woo, D. Mok, N.S. Choi, Y.S. Jung, J.H. Ryu, S.M. Oh, K.T. Lee, *Adv. Mater.* **26** (2014) 4139–4144.

[133] M. Dahbi, M. Fukunishi, T. Horiba, N. Yabuuchi, S. Yasuno, S. Komaba, *J. Power Sources*. **363** (2017) 404–412.

[134] A. Ponrouch, D. Monti, A. Boschin, B. Steen, P. Johansson, M.R. Palacín, *J. Mater. Chem. A*. **3** (2015) 22–42.

[135] C. Ding, T. Nohira, A. Fukunaga, R. Hagiwara, *Electrochemistry*. **83** (2015) 91–94.

[136] L.D. Ellis, T.D. Hatchard, M.N. Obrovac, *J. OfThe Electrochem. Soc.* **159** (2012) A1901–A1805.

[137] Z. Du, R.A. Dunlap, M.N. Obrovac, *J. Alloys Compd.* **617** (2014) 271–276.

[138] M.K. Datta, R. Epur, P. Saha, K. Kadakia, S.K. Park, P.N. Kumta, *J. Power Sources*. **225** (2013) 316–322.

[139] M. Dahbi, N. Yabuuchi, M. Fukunishi, K. Kubota, K. Chihara, K. Tokiwa, X.F. Yu, H. Ushiyama, K. Yamashita, J.Y. Son, Y.T. Cui, H. Oji, S. Komaba, *Chem. Mater.* **28** (2016) 1625–1635.

[140] M. Shimizu, Y. Tsushima, S. Arai, *ACS Omega*. **2** (2017) 4306–4315.

[141] M. Mortazavi, Q. Ye, N. Birbilis, N. V. Medhekar, *J. Power Sources*. **285** (2015) 29–36.

[142] G. Hasegawa, K. Kanamori, N. Kannari, J. Ozaki, K. Nakanishi, T. Abe, *ChemElectroChem*. **2** (2015) 1917–1920.

[143] D. Monti, E. Jónsson, M.R. Palacín, P. Johansson, *J. Power Sources*. **245** (2014) 630–636.

[144] C.Y. Li, J. Patra, C.H. Yang, C.M. Tseng, S.B. Majumder, Q.F. Dong, J.K. Chang, *ACS Sustainable Chem. Eng.* **5** (2017) 8269–8276.

[145] M. Montanino, M. Carewska, F. Alessandrini, S. Passerini, G.B. Appetecchi, *Electrochim. Acta*. **57** (2011) 153–159.

[146] T. Nokami, K. Matsumoto, T. Itoh, Y. Fukaya, T. Itoh, *Org. Process Res. Dev.* **18** (2014) 1367–1371.

[147] K. Tsunashima, A. Kawabata, M. Matsumiya, S. Kodama, R. Enomoto, M. Sugiya, Y. Kunugi, *Electrochem. Commun.* **13** (2011) 178–181.

[148] H. Usui, Y. Domi, H. Nishida, K. Yamaguchi, R. Yamagami, H. Sakaguchi, *ChemistrySelect*. **3** (2018) 8462–8467.

[149] L. Baggetto, P. Ganesh, R.P. Meisner, R.R. Unocic, J.C. Jumas, C.A. Bridges, G.M. Veith, *J. Power Sources*. **234** (2013) 48–59.

[150] J.M. Sangster, *J Phase Equilib. Diff.* **31** (2010) 62–67.

[151] M. Shimizu, H. Usui, H. Sakaguchi, *Phys. Chem. Chem. Phys.* **18** (2016) 5139–5147.

[152] T. Carstens, A. Lahiri, N. Borisenko, F. Endres, *J. Phys. Chem. C*. **120** (2016) 14736–14741.

[153] S. Menne, T. Vogl, A. Balducci, *Phys. Chem. Chem. Phys.* **16** (2014) 5485–5489.

[154] S. Duluard, J. Grondin, J.-L.L. Bruneel, I. Pianet, A. Grélard, G. Campet, M.-H.H. Delville, J.-C. Lassègues, *J. Raman Spectrosc.* **39** (2008) 627–632.

[155] M. Kunze, S. Jeong, E. Paillard, M. Schönhoff, M. Winter, S. Passerini, *Adv. Energy Mater.* **1** (2011) 274–281.

119

List of Publications

[1] Influence of the structure of the anion in an ionic liquid electrolyte on the electrochemical performance of a silicon negative electrode for a lithium-ion battery
K. Yamaguchi, Y. Domi, H. Usui, M. Shimizu, K. Matsumoto, T. Nokami, T. Itoh, H. Sakaguchi,
J. Power Sources, **338** (2017) 103-107.

[2] Elucidation of the Reaction Behavior of Silicon Negative Electrodes in a Bis(fluorosulfonyl)amide-Based Ionic Liquid Electrolyte
K. Yamaguchi, Y. Domi, H. Usui, H. Sakaguchi,
ChemElectroChem, **4** (12) (2017) 3257-3263.

[3] Superior Electrochemical Performance of Ni–P/Si Negative Electrode for Li-ion Batteries in an Ionic Liquid Electrolyte
K. Yamaguchi, Y. Domi, H. Usui, A. Ueno, T. Komura, T. Nokami, T. Itoh, H. Sakaguchi,
Chem. Lett., **47** (2018) 1416-1419.

[4] Effect of Film-forming Additive in Ionic Liquid Electrolyte on Electrochemical Performance of Si Negative-Electrode for LIBs
K. Yamaguchi, Y. Domi, H. Usui, M. Shimizu, S. Morishita, S. Yodoya, T. Sakata, H. Sakaguchi,
J. Electrochem. Soc., **166** (2019) A278-A286.

[5] Enhanced Performance of Sn_4P_3 Electrode Cycled in Ionic Liquid Electrolyte at Intermediate Temperature as Na-ion Battery Anode
H. Usui, Y. Domi, H. Nishida, K. Yamaguchi, R. Yamagami, H. Sakaguchi,
ChemistrySelect, **3** (29) (2018) 8462-8467.

[6] Electrochemical Performance of Sn_4P_3 Negative-Electrode for Na-Ion Battery in Ether-Substituted Ionic Liquid Electrolyte
K. Yamaguchi, H. Usui, Y. Domi, H. Nishida, T. Komura, T. Nokami, T. Itoh, H. Sakaguchi,
Electrochem. Commun., submitted.

Supplementary Publications

[1] Improved Electrochemical Performance of Lanthanum Silicide/Silicon Composite Electrode with Nickel Substitution for Lithium-Ion Batteries
Y. Domi, H. Usui, Y. Takemoto, K. Yamaguchi, H. Sakaguchi,
J. Phys. Chem. C, **120** (30) (2016) 16333-16339.

[2] Improved Electrochemical Performance of a Ge_xSi_{1-x} Alloy Negative Electrode for Lithium-Ion Batteries
Y. Domi, H. Usui, Y. Takemoto, K. Yamaguchi, H. Sakaguchi,
Chem. Lett., **45** (10) (2016) 1198-1200.

[3] Niobium-doped titanium oxide anode and ionic liquid electrolyte for a safe sodium-ion battery
H. Usui, Y. Domi, M. Shimizu, A. Imoto, K. Yamaguchi, H. Sakaguchi,
J. Power Sources, **329** (2016) 428-431.

[4] Advanced Performance of Annealed Ni–P/(Etched Si) Negative Electrodes for Lithium-Ion Batteries
Y. Domi, H. Usui, M. Narita, Y. Fujita, K. Yamaguchi, H. Sakaguchi,
J. Electrochem. Soc., **164** (2017) A3208-A3213.

[5] Ether Oxygen Atom Effects in Alkyl Side Chains on Physical Properties of Piperidinium Ionic Liquids
T. Nokami, T. Yamashita, T. Komura, N. Handa, M. Shimizu, K. Yamaguchi, Y. Domi, H. Usui, H. Sakaguchi, T. Itoh,
Faraday Discussions, **206** (2018) 523-534.

[6] Silicon-Based Anodes with Long Cycle Life for Lithium-Ion Batteries Achieved by Significant Suppression of their Volume Expansion in Ionic-Liquid Electrolyte
Y. Domi, H. Usui, K. Yamaguchi, S. Yodoya, H. Sakaguchi,
ACS Appl. Mater. Interfaces, (2019) *in press*.